A Fourier-Bessel Test of the Gravitational Inverse-Square Law

John G. Lee

A dissertation
submitted in partial fulfillment of the
requirements for the degree of

Doctor of Philosophy

University of Washington

2020

Reading Committee:

Blayne Heckel, Chair

Eric Adelberger, Chair

Andreas Karch

Program Authorized to Offer Degree:
Department of Physics

University of Washington

Abstract

A Fourier-Bessel Test of the Gravitational Inverse-Square Law

John G. Lee

Co-Chairs of the Supervisory Committee:
Professor Blayne Heckel
Department of Physics

Professor Eric Adelberger
Department of Physics

This dissertation presents the latest Eöt-Wash group test of the gravitiational Inverse Square Law (ISL) at the shortest possible distances using a stationary torsion pendulum above a rotating attractor. It largely builds off of earlier Fourier-Bessel work of Ted Cook [19] that utilized test-masses with both 18-fold and 120-fold azimuthal symmetries. In this case, the effective masses of the platinum test bodies of the 18- and 120-fold patterns on the pendulum were 0.21 and 0.62 mg. We tested the ISL at separations ranging from 52μm to 3mm. We have excluded at 95% confidence gravitational strength Yukawa interactions with length scales $\lambda > 39\mu$m and set new limits between $\lambda = 8\mu$m and 90μm. We have resolved gravitational interactions at the closest separations ever and measured a new systematic arising from the magnetic susceptibilities of our test-mass materials. We present a full description of the instrument, the analysis methods, and the results.

Hojišąnane, wiigihuhu anąga wiirokų gipįnįpįnį aašgekixjįirera wiiyaa'ųwi anąga Mąąrutira Inverse Square Law (ISL) yaagųswi. Eöt-Wash group test aanąągre yaa'ųwi. Waagax te'e, jaagu haisunąkwira wahakjene. Ted Cookga Fourier-Bessel airera hikišeregįnį anąga

woore že'e yaa'ųwi. Mąąssga ceexi wiirokųra haruwąkašąną nąga hogihižą nąga kerepąną nųųp wejąjąire. Wiigihuhura rutiire anąga peesįwįwigają hosgįgrera 0.21mg anąga 0.62mg yaagųswi. 52μm anąga 3mm hocąkeną peesįwį. 39μm anąga hiraicera hosereceja wesįwįgi, horoğocra hąke Yukawa Interaction Mąąrutira hikisgeižą herenį hire wahi. Yukawa nągre 8μm anąga 90μm hocąkenaija hąke wa'ųnįakgųnį yaarawi. Aašgexjį peesįwįwi anąga yaagųswigejene važącek yaagųsi yaare wa'ųajawi. Wiirokų yaa'ųwira, jaasge ha'ųwira, anąga hegųnegi jaagu yaapereswira wapahakjene.

TABLE OF CONTENTS

LIST OF FIGURES

ACKNOWLEDGEMENTS

This work would not have been possible without the help of so many people. In particular I would like to thank my advisors, Blayne and Eric, and the other members of the Eöt-Wash group: especially Will Terrano, Svenja Fleischer, and Charlie Hagedorn. I would also like to thank Prof. Andy Kim for his help while on sabbatical with us. The incredible enthusiasm from this small research group made this difficult work thoroughly enjoyable.

In addition, I would like to thank my friends and family for their support and encouragement in continuing on this project over the years. Finally, I want to thank Henning Garvin and Cecil Garvin for their work translating the abstract into Ho-Chunk. Pįįnagigiwi.

Chapter 1

INTRODUCTION

Gravity was the first physical force with a mathematical description, where the inverse-square law (ISL) was written down by Newton in the late 1600's. And even General Relativity, Einstein's classical theory of gravity, must match the ISL in the limit of weak gravitational fields. However, there is still no accepted physical theory that gives a fully quantum description of gravity in combination with the Standard Model of particle physics. Attempts at combining General Relativity with the Standard Model frequently require the introduction of subtle new currently undetected phenomena. For example, string theory (or M-theory), the leading candidate for unifying gravity and the Standard Model, necessarily invokes extra compact spatial dimensions and new nominally massless gravitationally coupled particles. This work presents the latest effort by the Eöt-Wash group to search for these hypothetical new forces by testing the ISL for gravity at the shortest possible distances. In this chapter, we list several plausible theoretical candidates as motivations for experiments of this type and roughly characterize the signature of a detection in our experiment. We also present the status of experimental limits on these hypothetical new forces prior to our result.

1.1 Theoretical Motivations

Throughout this chapter and the entire document, we characterize any violation of the Newtonian ISL as an additional Yukawa interaction. The Newtonian potential that gives rise to the ISL between two point masses m_1 and m_2 separated by a distance r is

$$V_N(r) = -G\frac{m_1 m_2}{r}.$$

Similarly, a Yukawa interaction that couples masses has a potential parameterized by a length scale λ beyond which the force is negligible and a coupling strength relative to gravity α

$$V_Y(r) = -\alpha G \frac{m_1 m_2}{r} e^{-r/\lambda}.$$

Experimenters fit their data to calculations of a combined Newtonian and Yukawa potential

$$V(r) = V_N(r) + V_Y(r) = -\frac{G m_1 m_2}{r}\left(1 + \alpha e^{-r/\lambda}\right)$$

to constrain α for a given λ. It is important to note that any given ISL experiment is sensitive to a range of λ's between the shortest and largest separations at which the data are obtained. It should also be noted that if a convincing violation of the ISL were observed it would be important to establish whether it actually has a Yukawa form and if it obeys the Equivalence Principle, i.e. if α is independent of composition.

1.1.1 Large Extra Dimensions and the Gauge Hierarchy Problem

One inspiration for testing the ISL came from a possible solution to the Gauge Hierarchy Problem (GHP), which arises from the comparably large difference in the strength of gravitational interactions relative to electroweak interactions. One can relate the gravitational constant to an energy scale known as the Planck mass $M_{Pl} = \sqrt{\frac{\hbar c}{G}}$ which is considerably larger than the electroweak energy scale, $M_{Pl} \approx 10^{19}\text{GeV} \gg m_{EW} \approx 10^{3}\text{GeV}$. The Newtonian ISL potential is proportional to the inverse-square of this mass scale.

$$V_N(r) \propto \frac{1}{M_{Pl}^2}\frac{m_1 m_2}{r}.$$

In 1998, Arkani-Hamed, Dimopoulos, and Dvali (ADD) proposed a model to solve the GHP by introducing extra compact spatial dimensions such as would arise in string theory [6]. At separations smaller than the size of the extra n dimensions, gravity obeys an inverse-(2+n) law which follows from Gauss' law generalized to (3+n)-dimensions. The gravitational

potential which gives rise to such a force is

$$V_{N,3+n}(r) \propto \frac{1}{M_*^{2+n}} \frac{m_1 m_2}{r^{n+1}}, \quad (r \ll R)$$

where M_* is some new mass scale introduced for dimensional consistency which we will see can be less than the Planck mass. At separations large compared to the size of the extra dimensions, the gravitational potential would give rise to the normally observed ISL

$$V_{N,3+n}(r) \propto \frac{1}{M_*^{2+n} R^n} \frac{m_1 m_2}{r}, \quad (r \gg R)$$

and the observed Planck mass relates to the other true mass scale by

$$M_{Pl}^2 \propto M_*^{2+n} R^n.$$

The authors suggest that the only true energy scale may be the electroweak scale, $M_* = m_{EW}$, and that the observed Planck mass and the relative weakness of gravity would be explained by the possibly large size of the extra dimensions. In particular, two large extra dimensions would imply R $\sim 100\mu$m.

The compactified dimensions would additionally give rise to Kaluza-Klein massive excitations of the graviton which, for separations larger than the size of the extra dimensions would appear as a Yukawa force with $\alpha = 8n/3$ and $\lambda =$ R. Strong constraints on the ADD model now come from collider experiments like the LHC and astrophysical observations for $n \geq 2$ [1],[27], Small amounts of warping in the metric make direct observation relevant as a relatively model-independent test, and direct tests of the ISL still provide the tightest constraints on a single large extra dimension [41][4].

1.1.2 String Theory Moduli

String theory not only requires the existence of extra spatial dimensions but also many possible new scalar particles known as moduli that characterize the low energy effective theory. These can come in a wide range of coupling strengths and length scales. One of the

best characterized is the dilaton, which sets the scale of string couplings and would couple to matter with $\mathcal{O}(1) \leq \alpha \leq \mathcal{O}(1000)$ [34].

More generally, in these quantum descriptions of gravity, the size of the spatial dimensions may fluctuate, and a scalar particle known as the radion is needed to stabilize the effective size of these extra dimensions. The relative coupling strength is expected to scale with a dependence on the number of extra dimensions as $\alpha = \frac{n}{n+2}$, $n \geq 2$. Some estimates of the expected coupling strengths and interaction length scales of the radion, dilaton, and other moduli are depicted along with previous experimental constraints in figure 1.1.

1.1.3 Dark Energy Scale

Dark energy provides another motivation for short range tests of gravity. The universe is seen to be undergoing an accelerating expansion, seen in measurements of Hubble's constant through redshifts of Type 1a supernovae, the CMB, structure formation, etc. The simplest explanation for this expansion adds a cosmological constant Λ related to the energy density of empty space. This term is equivalent to a negative pressure fluid throughout the universe. In either sense of this dark energy, we can associate a length scale,

$$\lambda_\Lambda = \left(\frac{\hbar c}{\rho_\Lambda}\right)^{\frac{1}{4}} = \left(\frac{8\pi G\hbar}{3\Omega_\Lambda H_0^2 c}\right)^{\frac{1}{4}} \approx 86\mu m \tag{1.1}$$

where $\rho_\Lambda = \frac{\Lambda c^4}{8\pi G}$ is the vacuum energy density of the universe, $H_0 = 67.66 \pm .42$km s^{-1} Mpc^{-1} is the Hubble parameter, and $\Omega_\Lambda = .6889 \pm .0056$ is the ratio of the vacuum energy density to the critical density for a flat universe [18]. We might then expect to see any new gravitional phenomena associated to dark energy to be manifested around this length scale [8].

1.1.4 Cosmological Constant Problem and Fat Gravitons

Another problem in our understanding of dark energy comes from considering the cosmological constant as the vacuum energy density of the universe. Theorists have attempted

to compute the vacuum energy density by summing the zero-point energies of the normal modes of a field with mass m up to some wavenumber cutoff $k_{max} \gg m$

$$< \rho > \; = \; \hbar c \int_0^{k_{max}} \frac{\sqrt{k^2 + m^2}}{2} \frac{4\pi k^2 \mathrm{d}k}{(2\pi)^3} \approx \frac{\hbar c k_{max}^4}{16\pi^2}. \tag{1.2}$$

Setting k_{max} to the Planck scale leads to an estimate 120 orders of magnitude larger than the observed value, and even at the QCD scale the estimate is still larger by 40 orders of magnitude [58]. One proposal for resolving this problem is the idea of a fat graviton [48]. If the graviton has some finite size, then it can distinguish between hard and soft processes and the high momentum contributions to the cosmological constant are suppressed. This effective theory suggests the gravitational potential goes to zero below some length scale. This length scale must be greater than 20μm in order to solve the cosmological constant problem.

1.1.5 Particles with Screening Mechanisms

Models of the dark sector of physics often predict additional particles and forces, but these new forces must conform to constraints from laboratory or space-based tests. One way to escape such constraints on new long range forces is through a screening mechanism that makes the effect vanish under laboratory conditions. There are a few known screening mechanisms: Chameleons, symmetrons, and the Vainshtein mechanism. Chameleon and symmetron particles in particular are accessible to short-range tests of gravity [11].

Chameleons

The chameleon mechanism gives a scalar or vector particle with self-interactions and a mass that is dependent on the local matter density [11] [38]. In low density regions, as in space, the particle becomes light and mediates a long-range force, but in higher density regions, the particle becomes massive and the range of the mediated force shrinks. In effect, the chameleon force between two test-bodies arises only from a thin "skin" on the test-bodies, attenuating

the strength by a huge factor. The chameleon mass in an experiment such as ours where the test-bodies are very thin depends on all of the nearby matter including the electrostatic screen between the test-masses of this experiment, which makes the highly non-linear force fairly difficult to calculate. Additional constraints arise from a theoretical requirement that quantum corrections are small [55], so that the theory remains perturbative and hence predictive. Calculations constraining a chameleon particle with a ϕ^4 self-interaction have been performed for previous iterations of this experiment [53].

Symmetrons

The symmetron mechanism for a scalar particle has a vacuum expectation value (VEV) that depends on the local matter density, becoming large in regions of low density and small in regions of high density. In constrast to the chameleon mechanism where the scalar mass changes and the interaction length diminishes in the presence of matter, the symmetron undergoes spontaneous symmetry breaking in high density regions such that the VEV goes to zero and its coupling to matter vanishes. Again calculations are demanding but have been performed for previous iterations of this experiment [54].

1.1.6 Unparticles

There have also been proposals for a scale-invariant sector of "unparticles" that couple to standard model particles[24]. Scale invariant theories arise in theories with supersymmetry, string theory, and particularly in AdS/CFT. If the scale invariance is unbroken at low energies, a long range force with a possibly non-integer power-law potential arises [21].

1.2 Recent Experimental Results

A wide variety of experiments have searched for Yukawa interactions that couple to mass at various length scales and coupling strengths. We do not exhaustively review these but list a couple of recent results and show the current limits prior to our work on $|\alpha|$ over the range of λ accessible to our experiment, see figure 1.1.

1.2.1 Torsion Balance Tests

Several torsion balance tests have been performed since the last published Eöt-Wash result [36] including two from our research group. Each of the torsion balance experiments used an electrostatic screen consisting of a thin conductive foil between the test-masses to prevent electrostatic interactions.

Fourier-Bessel Pendulum V.1

The experiment by Ted Cook [19] pioneered a test-mass geometry for which the Fourier-Bessel expansion provides analytic solutions of the torques for both Newtonian and Yukawa interactions. Our work utilized much of the same apparatus and techniques of Cook's experiment as well as many of Cook's suggested improvements. Cook's experiment tested the ISL at separations between 57μm and 2mm. The data preferred the inclusion of a long range Yukawa of $\lambda = 10$mm at $\alpha = .021 \pm .005$ likely due to some undetermined systematic effect and so remained unpublished.

Parallel Plate

A parallel plate torsion balance ISL test was performed by Charlie Hagedorn also of the Eöt-Wash group in 2015 [26]. The work was complementary to our other ISL test as it was a null test with a potentially higher signal-to-noise ratio. The pendulum consisted of a flat titanium plate with tungsten insets, and an effectively "infinite" plane of tantalum served as the source mass which actuated horizontally toward and away from the stationary pendulum . The experiment tested the ISL at separations ranging from 159μm to 850μm. It is also note-worthy that the experiment was performed with the measured torques completely blinded and with a public unblinding.

HUST

Two recent experiments from Huazhong University of Science and Technology in 2012 and 2016 placed new 95% confidence limits on α between $\lambda = 0.7 - 5.0$mm and $\lambda = 70 - 300\mu$m, respectively [60][50]. The 2012 experiment used an I-shaped pendulum with tungsten end masses and a horizontally-oriented I-shaped structure with similar tungsten plates as a source mass, which sinusoidally translated back-and-forth toward the pendulum. The tungsten source masses were partially compensated by similar tungsten masses on the opposite side of the pendulum. The experiment measured torques at separations ranging from $0.4 - 4.3$mm. The 2016 experiment used a similar I-shaped pendulum and a rotating source mass of alternating 8-fold pattern of tungsten and glass wedges in a horizontal orientation, measuring the torque at several separations from $0.25 - 1.00$mm.

Huazhong University of Science and Technology published another result concurrent with our experiment, improving on their 2016 experimental set-up [49]. They stiffened their electrostatic screen support against vibrations allowing for closer separations and nulled the electrostatic potential between the pendulum and screen. They placed new 95% confidence limits on α between $\lambda = 40 - 350\mu$m.

1.2.2 Casimir Force Tests

In 2016 an Indiana University - Purdue University Indianapolis group placed new 95% confidence limits on α for λ between 30 and 8000nm [16]. This experiment used a microelectromechanical torsional oscillator with a spherical gold-coated test-mass on one side of the oscillator suspended over a rotating source mass with several wedge-shaped patterns of gold and silicon. This experiment did not use an electrostatic screen, but the source mass had a uniform gold-coating such that the Casimir force above the silicon and gold wedges was nearly matched. The group searched for a density-dependent force in-phase with the silicon wedges at separations between 200nm and 1μm.

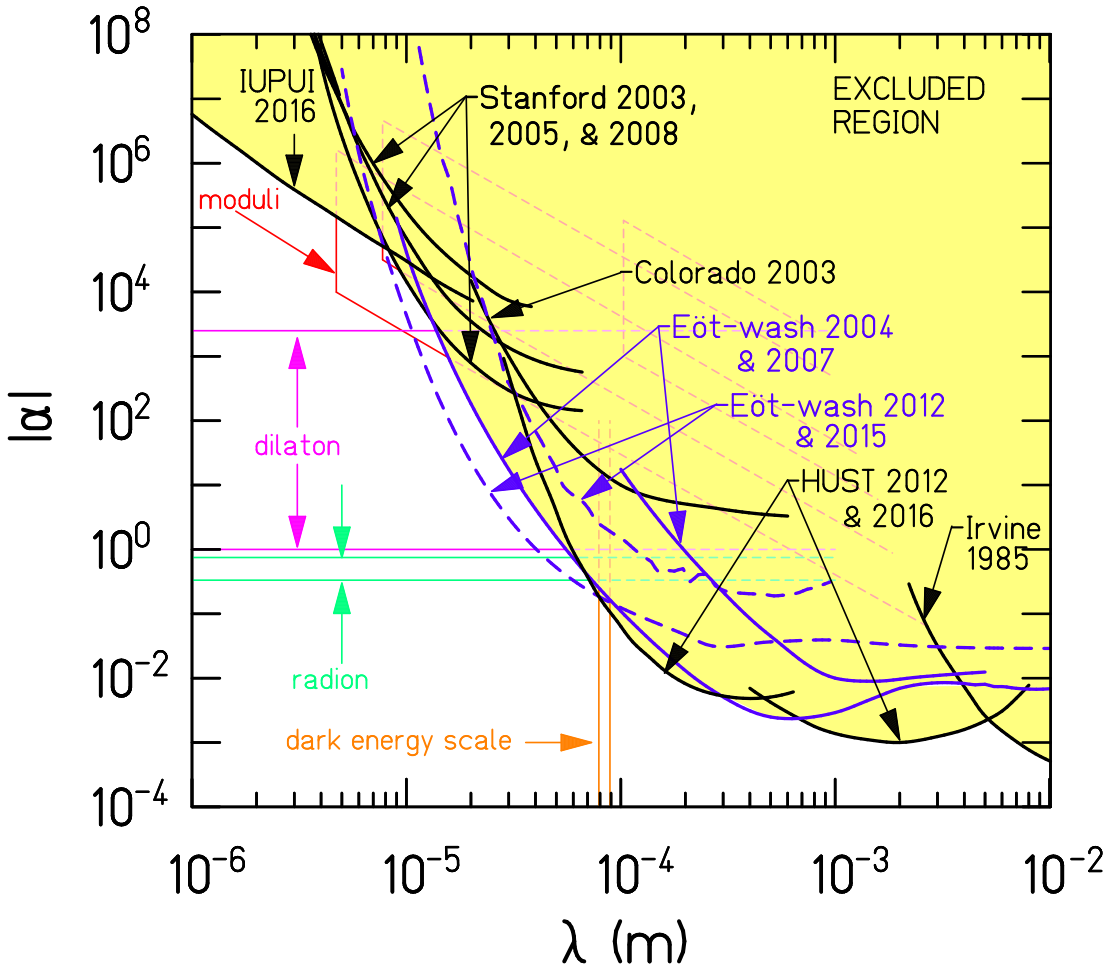

Figure 1.1: **Previous 95% confidence level constraints on Yukawa interactions** $(\lambda, |\alpha|)$ **with ranges between** 10^{-6}**m and** 10^{-2}**m.** - The dashed curves correspond to unpublished constraints from [19] [26]. Solid blue curves are previous limits from the Eöt-Wash group, [36][31], while solid black lines correspond to limits from [16][50][60][17][44][25][30]

Chapter 2

CALCULATED GRAVITATIONAL, YUKAWA, AND MAGNETIC TORQUES

We have chosen a geometry that makes the calculation of gravitational and Yukawa forces nearly analytic through the Fourier-Bessel decomposition. This section describes the derivation of the solution, corrections and numerical calculations for deviations from cylindrical symmetry, and the use of the Fourier-Bessel formalism for magnetostatic systematic torque calculations.

2.1 Fourier Bessel Expansion

The Fourier-Bessel decomposition for the torque calculations was suggested by George Bertsch, applied by Blayne Heckel, formally written down by Frank Marcoline, and turned into an efficient Fortran code `FBESSELN` by Eric Adelberger as has been stated before, [37][19][52]. For the sake of completeness, the same solutions are briefly written here.

2.1.1 Modified Helmholtz Green's Function

The Newtonian and Yukawa potentials are solutions of the modified Helmholtz equation

$$(\nabla^2 - \mu^2)\Phi(\vec{r}) = -\rho(\vec{r})$$

This linear differential equation has a Green's function, $G(\vec{r}, \vec{r}')$ satisfying the equation which allows us to calculate the potential

$$(\nabla^2 - \mu^2)G(\vec{r}, \vec{r}') = -4\pi\delta(\vec{r} - \vec{r}').$$

In Cartesian coordinates, the Green's function is given by

$$G(\vec{r},\vec{r}\,') = \frac{e^{-\mu|\vec{r}-\vec{r}\,'|}}{|\vec{r}-\vec{r}\,'|}$$

from which we can see that Newtonian gravity corresponds to $\mu = 0$ and the Yukawa potential to $\mu = 1/\lambda$.

The Laplacian is separable in cylindrical coordinates so that

$$\left(\frac{1}{r}\frac{\partial}{\partial r}r\frac{\partial}{\partial r} + \frac{1}{r^2}\frac{\partial^2}{\partial\phi^2} + \frac{\partial^2}{\partial z^2} - \mu^2\right)G(\vec{r},\vec{r}\,') = -4\pi\frac{1}{r}\delta(r-r')\delta(\phi-\phi')\delta(z-z').$$

We then use the following identities,

$$\delta(\phi-\phi') = \frac{1}{2\pi}\sum_{m=-\infty}^{\infty} e^{im(\phi-\phi')},$$

$$\frac{1}{r}\delta(r-r') = \int_0^\infty dk\, k J_m(kr)J_m(kr'),$$

and apply Bessel's differential equation, $(x\frac{\partial}{\partial x}x\frac{\partial}{\partial x} + k^2x^2 - m^2)J_m(kx) = 0$, to get the final identity

$$\delta(z-z') = -\frac{e^{-\sqrt{k^2+\mu^2}(z_>-z_<)}}{\sqrt{k^2+\mu^2}}.$$

So that the Green's function is given by

$$G(\vec{r},\vec{r}\,') = \sum_{m=-\infty}^{\infty} e^{im(\phi-\phi')}\int_0^\infty dk\, k\, J_m(kr)J_m(kr')\frac{e^{-\sqrt{k^2+\mu^2}(z_>-z_<)}}{\sqrt{k^2+\mu^2}}.$$

To compute the torques from one mass distribution on another, we start by defining the potential energy

$$U = -\frac{G}{4\pi}\int d^3r\,\rho(\vec{r})\int d^3r'\,\rho(\vec{r}\,')G(\vec{r},\vec{r}\,'),$$

from which we may derive the torque as

$$\tau = -\frac{\partial U}{\partial\phi}.$$

2.1.2 Torque Calculation from Wedge Sources

Our experiment makes use of N-fold symmetric wedge-shaped test-masses. We define the mass distribution of a single N-fold wedge pattern of density ρ, half-thickness s, inner radius r_0, outer radius r_1, half-subtended angle β, angular offset from the x-axis ϕ_0, and height above the plane h as

$$\rho(\vec{r}) = \rho\left[\Theta(r-r_0)-\Theta(r-r_1)\right]\left[\Theta(z-h+s)-\Theta(z-h-s)\right]\times \sum_{j=0}^{N-1}\left[\Theta\left(\phi-\phi_0-\frac{2j\pi}{N}+\beta\right)-\Theta\left(\phi-\phi_0-\frac{2j\pi}{N}-\beta\right)\right].$$

A test-mass may be comprised of several layers of the same N-fold symmetry with different densities or geometric parameters.

Our test-masses are separated vertically, which allows us to separate our source distributions with primed coordinates for the attractor test-mass and unprimed coordinates for the pendulum test-mass. By changing the order of integration, we can analytically compute the source volume integrals over the wedge layers so that the potential energy is then

$$U = -\frac{G}{4\pi}\sum_{m=-\infty}^{\infty}\int_0^\infty \frac{dk\,k}{\sqrt{k^2+\mu^2}}\sum_{a=1}^{N_a}\sum_{p=1}^{N_p} I_a I_p,$$

where I_a and I_p are the analytically computed source distribution integrals for each N_a attractor layers and each N_p pendulum layers.

$$\begin{aligned}
I_a &= \frac{4\rho^a}{l\alpha}\sin(Nl\beta^a)e^{-im(\phi_0^a+\phi)}\sinh(s^a\alpha)e^{h^a\alpha}R^{(1)}_{Nl}(r_0^a,r_1^a;k)\\
I_p &= \frac{4\rho^p}{l\alpha}\sin(Nl\beta^p)e^{im\phi_0^p}\sinh(s^p\alpha)e^{-h^p\alpha}R^{(1)}_{Nl}(r_0^p,r_1^p;k)\\
\alpha &= \sqrt{k^2+\mu^2}\\
R^{(1)}_m(r_0,r_1;k) &= \frac{2m}{k}\sum_{j=0}^{\infty}\frac{(m+2j+1)}{(m+2j)(m+2j+2)}\left[r_1 J_{m+2j+1}(kr_1)-r_0 J_{m+2j+1}(kr_0)\right].
\end{aligned}$$

We have skipped the source volume integral derivations, but we will note that the integral over polar angle restricts the potential energy contributions to only arise from integer harmonics l of the symmetry number N. We now define the potential as

$$U = \sum_{l=-\infty}^{\infty} U'_{Nl}$$

If the wedge pattern is evenly spaced, $\beta = \frac{\pi}{2N}$ then we could restrict ourselves to only odd harmonics. From the form of the Green's function, we know that $U'^{*}_{Nl} = U'_{-Nl}$, so that we define $U_{Nl} = U'_{-Nl} + U'_{Nl} = 2\mathcal{R}e\{U'_{Nl}\}$, and the energy is

$$U = U'_0 + \sum_{l=-0}^{\infty} U_{Nl}.$$

The U'_0 term does not contribute to the torque, so will be ignored. Combining everything together, the potential is

$$\begin{aligned} U &= \sum_{l=0}^{\infty}\sum_{a=0}^{N_a}\sum_{p=0}^{N_p} A^{a,p}_{Nl}\cos(Nl(\phi^a_0 - \phi^p_0 + \phi_0)) \\ A^{a,p}_{Nl} &= -\frac{G}{4\pi}\frac{32\rho_a\rho_p}{l^2}\sin(Nl\beta^a)\sin(Nl\beta^p)\times \\ &\quad \int_0^{\infty}\frac{dk\,k}{\alpha^3}\sinh(s_a\alpha)\sinh(s_p\alpha)e^{\alpha(h^a-h^b)}R^{(1)}_{Nl}(r^a_0, r^a_1; k)R^{(1)}_{Nl}(r^p_0, r^p_1; k) \end{aligned}$$

The amplitude of the corresponding torque at a given harmonic of the attractor rotation is given by the derivative of the potential contribution,

$$\tau_{Nl} = -\frac{\partial U_{Nl}}{\partial \phi_0} = Nl\sum_{a=0}^{N_a}\sum_{p=0}^{N_p} A^{a,p}_{Nl}\sin(Nl(\phi^a_0 - \phi^p_0 + \phi_0)$$

To summarize, the torque calculation has been reduced from a set of six spatial integrals, down to a single integral over an infinite range and two infinite sums which must be evaluated numerically. The sums converge quickly so can be truncated. The integrand is also sharply peaked, but the integration range must be checked before the calculations.

2.2 Off-Center Calculations

The Fourier-Bessel solutions allows for fast computations of the cylindrically symmetric wedge-patterns, but breaks down when radial misalignments break the cylindrical symmetry. We utilized the Monte-Carlo calculations developed by Cook [19] to build similar empirical models of the off-center torques.

2.2.1 Fourier-Bessel Monte-Carlo

The code developed by Cook to compute the effect of radial misalignments of the test-masses retains as much of the Fourier-Bessel solution as possible and performs the rest of the integration through Monte-Carlo sampling. The attractor test-mass is left fixed while the pendulum test-mass is moved to the radially mis-centered position, leaving the three integrals of the attractor volume and the pendulum z-integral intact. The remaining two volume integrals of the pendulum test-mass are performed by uniformly sampling (r, ϕ) values in the the set of translated pendulum wedges, and then performing the "k-integral" numerically as in `FBESSELN`. The calculations reveal that the torques all remain in the same phase and that the torque is independent of the direction of radial misalignment. We made one slight improvement to the code by instead summing the randomly sampled values of the pendulum volume integrand before performing the k-integral. This resulted in less calculations of the same attractor volume integrals, which reduced the calculation time of the third harmonic of the 18-fold pattern by approximately 7×.

2.2.2 Off-Center Empirical Functions

Again following in the footsteps of Cook, we constructed empirical functions to approximate the off-center FBMC calculations. We calculated the off-center torques using the nominal geometry for the 18ω and 120ω torques as well as for the 3^{rd} harmonic of the 18-fold pattern, ie. the 54ω. We chose to use the same functional form for the empirical function defined as

	harmonic		
coefficient	18ω	54ω	120ω
c_0	0.961	0.722	0.376
c_1	3.579	2.717	5.046
c_2	0.979	0.324	0.824
c_3	-4.715	-2.862	-1.216
c_4	-0.420	-0.428	-0.212
c_5	-3.080	-3.626	-6.207
c_6	-4.299	-7.469	-7.860

Table 2.1: Fit coefficients of empirical off-center functions.

follows

$$R(r,s,\lambda) = c_0 + (1-c_0)\cos(f(s,\lambda)r)$$
$$f(s,\lambda) = c_1 + c_2 e^{c_3 y(s,\lambda)}$$
$$y(s,\lambda) = \begin{cases} s, & \text{Newton } (\lambda = \infty) \\ (1-e^{c_6\lambda})s + c_4 e^{c_5\lambda}, & \text{Yukawa} \end{cases}$$

Where $c_0 - c_6$ are seven fit coefficients, r and s are the test-mass radial misalignment and separation, and λ is the Yukawa length scale. We fit the gravitational and Yukawa off-center calculations with least-squares to determine each of the seven coefficients for each harmonic (see table 2.1).

2.3 Magnetic Calculations

As discussed elsewhere in this thesis, we discovered that the application of an external uniform vertical magnetic field produced a significant torque that is ascribed to the induced magnetization in the platinum foils. The magnetostatic problem can also be formulated as a potential that satisfies the Poisson equation [33], where the magnetic field strength is given

by the gradient of the potential and the magnetic density is given by the negative divergence of the magnetization:

$$\vec{H} = \vec{\nabla}\Phi_M, \quad \nabla^2\Phi_M = -\rho_M, \quad \rho_M = -\vec{\nabla}\cdot\vec{m}.$$

Again the potential can be computed by a convolution with the Green's function,

$$\Phi_M(x) = -\frac{1}{4\pi}\int d^3x'\,\vec{\nabla}\cdot\vec{m}G(\vec{r},\vec{r}\,').$$

We assume the magnetic density to be well-behaved and localized so that the potential goes to zero at infinity. We can then integrate by parts, writing the potential as

$$\Phi_M(x) = \frac{1}{4\pi}\int d^3x'\,\vec{m}\cdot\vec{\nabla}G(\vec{r},\vec{r}\,').$$

The potential energy of the magnetized pendulum wedges in the magnetic field from the magnetized attractor wedges is given ([33] problem 5.21)

$$\begin{aligned} U &= -\frac{\mu_0}{2}\int_{V_P} d^3x\,\overrightarrow{m_P}\cdot\vec{H_A} \\ &= -\frac{\mu_0}{2}\int_{V_P} \overrightarrow{m_P}\cdot\vec{\nabla}\Phi_{M,A} \\ &= -\frac{\mu_0}{8\pi}\int_{V_P} \overrightarrow{m_P}\cdot\vec{\nabla}\int_{V_A}\overrightarrow{m_A}\cdot\vec{\nabla}G(\vec{r},\vec{r}\,'). \end{aligned}$$

This expansion allowed us to compute systematic torques due to a difference in susceptibility in the the platinum wedges, section 10.1. A nearly identical formulation may be derived from spin-spin coupling of electron spins and is very similar to the hypothetical dipole-dipole interactions searched for in [52][51]. For this systematic, we treat the magnetization of the wedges as linearly dependent on the applied field without any second order effect from nearby magnetized materials, static in the vertical direction, and compute the torques due to the difference in susceptibility between the platinum wedges and the Stycast 1266 filled between the wedges. The net magnetization is

$$\overrightarrow{M} = \frac{\chi_{Pt}-\chi_{1266}}{\mu_0}B_z\hat{z} = \frac{\Delta\chi}{\mu_0}B_z\hat{z}.$$

with the potential energy is given by

$$U = \frac{\mu_0}{8\pi} \int d^3x \int d^3x' \left(\frac{\Delta\chi B_z}{\mu_0}\right)(x) \left(\frac{\Delta\chi B_z}{\mu_0}\right)(x') \frac{\partial}{\partial z}\frac{\partial}{\partial z'} G(\vec{r}, \vec{r}').$$

Again we can sum over the effect of layers of wedges at a given harmonic, so that the energy of the l^{th} harmonic of an N-fold wedge pattern is

$$U_{Nl} = \sum_{a=1}^{N_a} \sum_{b=1}^{N_b} A_{Nl}^{a,b} \cos(Nl(\phi_0^a - \phi_0^b + \phi_0))$$

where the amplitude is defined as

$$A_{Nl}^{a,b} = \frac{\mu_0}{8\pi} \left(\frac{\Delta\chi_a B_z}{\mu_0}\right) \left(\frac{\Delta\chi_b B_z}{\mu_0}\right) \frac{32N}{l} \sin(Nl\beta^a) \sin(Nl\beta^b)$$
$$\times \int_0^\infty \frac{dk\, k}{\alpha} \sinh(\alpha s^a) \sinh(\alpha s^b) e^{\alpha(h^a - h^b)} R_{Nl}^{(1)}(r_i^a, r_o^a; k) R_{Nl}^{(1)}(r_i^b, r_o^b; k).$$

This same analysis can be performed for radially and azimuthally oriented magnetizations.

Chapter 3
APPARATUS

This experiment was originally intended to be a quick upgrade of Cook's Fourier-Bessel experiment correcting known flaws in the test bodies with improved materials and fabrication procedures while also implementing new features that facilitated more precise alignments [19]. The first major upgrade was an improved test-mass design that we detail in Chapter 4. Our second major improvement was the addition of three in-situ Physik Instrumente actuators to align and position the electrostatic screen. This required a re-design of a majority of the lower half of the vacuum chamber. In the course of this upgrade process we made several other improvements to the apparatus. The details of these upgrades are given below.

3.1 Apparatus Improvements

3.1.1 In-Situ Screen Actuators

In Cook's experiment, the screen was aligned to the attractor using a measuring microscope and then installed in the apparatus. This caused problems because environmental changes, especially slow thermal drifts, caused the micron-scale alignment to deteriorate. Following Cook's suggestions, we re-designed the whole lower portion of the apparatus vacuum chamber to accomodate three M-227K063 vacuum-compatible actuators from Physik Instrumente, see figure 3.1. The actuators had 10mm of travel with encoders to track the position with 1μm repeatability. The actuators supported the electrostatic screen on a flexure above the attractor test-mass allowing us to adjust the tip and tilt of the screen and set it parallel to the attractor surface in vacuum. Additionally, we were able to translate the screen relative to the attractor test-mass and simultaneously measure capacitance as a function of the encoder positions to determine separation.

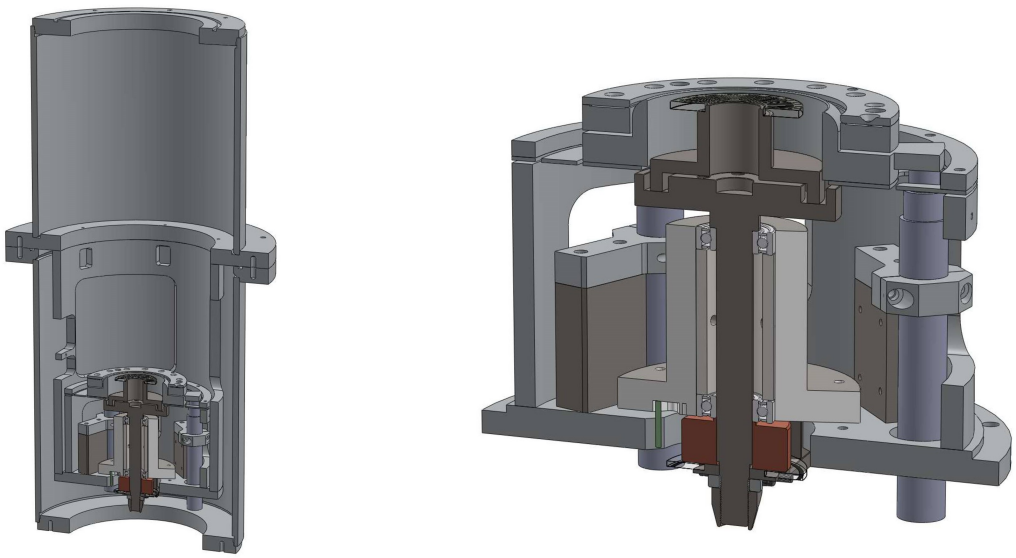

Figure 3.1: **Diagrams of lower apparatus - Left:** Cut-away drawing of the re-designed lower portion of the vacuum chamber. The larger diameter accommodated three vacuum-compatible actuators with micron repeatability. **Right:** Detail of actuators supporting stretched screen on flexure and attractor turntable.

3.1.2 Apparatus Tilt

The apparatus was supported on three adjustable instrument feet which allowed us to change the tilt of the apparatus to make the screen parallel to the pendulum test-mass. Previously, adjusting the instrument feet and apparatus tilt required entering the thermal enclosure which caused long term drifts in apparatus tilt and pendulum twist as temperatures equilibrated. We added two remotely-controllable stepper motors on two of the three instrument feet which allowed us to adjust tilts more frequently without introducing thermal drift.

3.1.3 Vacuum Chamber and Spider

We redesigned the lower half of the vacuum chamber to accommodate the new in-situ actuators. The portion of the appartus that hangs from the upper portion of the chamber

and holds the turntable and fixed mirrors for the angle readout (colloquially known as the "spider") was also made larger and out of thicker material. This was intended to stiffen the spider to any flexing from the tiny friction in the turntable bearing. A flexure pressing the lower portion of the vacuum can against the spider was still needed to decrease a 1ω signal in the measured pendulum twist.

3.1.4 Calibration Turntable

The torque measurements were calibrated with a known gravitational signal provided three brass spheres on a turntable external to the vacuum chamber. We increased the calibration turntable diameter to accommodate the new vacuum chamber and to provide a larger aperture for the fixed cables that powered the turntable motor, angle encoder, etc. This allowed us to make calibration measurements throughout the science data collection.

3.1.5 Foil Stretcher

The electrostatic screen foil-stretcher was redesigned in a fashion similar to that employed in the parallel-plate ISL experiment [26] with a circular clamping mechanism and only three points to tension the screen. This design still left one side of the screen visually open for managing dust and provided a more uniform tension.

3.1.6 Attractor tip-tilt

We replaced the attractor "cup", the titanium piece that held the attractor test-mass on the turntable, with one that decoupled the tip-tilt and radial adjustments. The new tip-tilt screws were #0-80 brass screws that compressed phosphor-bronze springs and allowed for finer adjustments than the previous version, see figure 3.2.

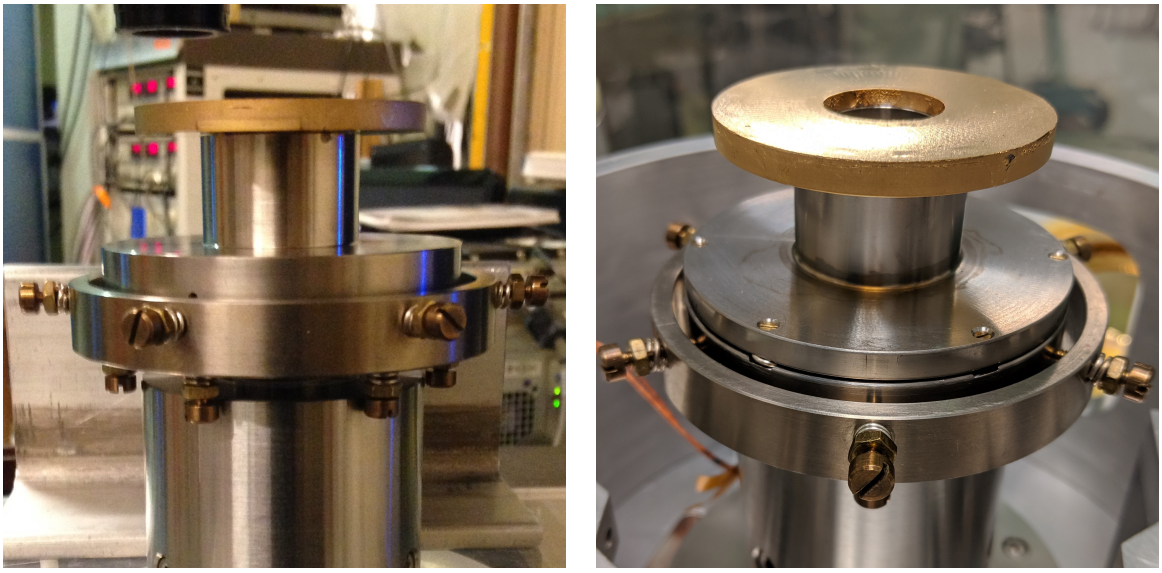

Figure 3.2: **Attractor "cup" comparison to previous Fourier-Bessel experiment** - The original tip-tilt stage (left) leveled the attractor test-mass with three tensioned #4-40 screws below the cup and adjusted the runout with three screws outside the cup. The tip-tilt adjustment was improved (right) with finer pitch screws on top of the cup to decouple tip-tilt from the runout adjustment.

3.1.7 Ion Pump

The original turbomolecular pump used to achieve vacuum was coupled to the instrument through a flexible bellows which caused significant tilts of the apparatus when evacuated and increased tilt coupling to changes in atmospheric pressure. We replaced the turbo pump with an ion pump (Agilent StarCell 20L/s) which still achieved pressures of $1 - 2\mu$Torr and decreased the tilt coupling.

3.1.8 Thermal Enclosure Temperature Control

A digital control loop replaced a broken analog temperature controller for the thermal enclosure box. The digital PID controller set a Neslab RTE-17 water bath chiller temperature

which was coupled to a large copper plate and a Honda radiator with a circulating fan to lock the temperature of the thermal enclosure. The average temperature variation at the autocollimator was only ±5.2mK in the science data.

3.2 Apparatus Preparation

We installed the majority of upgrades in the summer of 2016. Several alignment steps were necessary for achieving small test-mass separations before the apparatus could commence with data taking, detailed in Chapter 5. The general procedure for preparing the apparatus for data taking was as follows

1. Align attractor tilt and runout, pendulum test-mass tilt, and electrostatic screen to the attractor test-mass (see Chapter 5).
2. Clean pendulum side to achieve smallest separations to the screen.
3. Bake the apparatus, fiber, and ion pump ($\approx 50^\circ$ C) to lower vacuum pressure and remove drift in equilibrium angle, θ_0.
4. Turn on the ion pump and detach the turbo-pump and roughing pump system.
5. Close the thermal enclosure, turn on water and air circulation systems, and start temperature-control loops to lock the air temperature in the enclosure.
6. Level the screen to the attractor test-mass while finding minimum attractor separation without evidence of touching.
7. Measure attractor-screen capacitance versus separation and reset screen position to minimum attractor separation.
8. Level the electrostatic screen to the pendulum test-mass by tilting the apparatus.
9. Perform pendulum-screen capacitance versus separation scan.
10. Center the pendulum test-mass above the attractor test-mass rotation axis gravitationally.
11. Re-measure pendulum-screen capacitance versus separation.
12. Begin normal data taking procedure.

Chapter 4

TEST-MASS FABRICATION

The platinum foil test-masses were key components of the experiment. The fabrication process was similar to that used by Cook, [19], except for the gluing step which was based on a procedure described in the dissertation work of D. Weld, [59]. The main components of the fabrication were determining the thicknesses of the foils, measuring the mass removed in the patterns from machining, making precise measurements of the pattern shape, and the gluing procedure.

4.1 Thicknesses

We started with a set of four 50μm thick and two 100μm thick 65mm×65mm platinum foils from GoodFellow. Before cutting any patterns in the platinum foils, we measured the platinum foil thicknesses. We developed an improved method over the previous iteration's use of a precision micrometer by using an OGP ZipLite 250 SmartScope touch-probe. Each measurement consisted of a 60mm×60mm grid of points scanned through x, y-positions and then reversed. The reversal within each scan averaged out temperature drifts and gave a repeatability better than 1.5μm. The foil measurement was paired with a background measurement of the underlying glass substrate using the same procedure. The 20×20-point foil and background scans were then subtracted to obtain the thicknesses. Each foil thickness measurement consisted of four foil and background scan pairs including one measurement with flipping the foil about the y-axis and another rotating the foil by 90°. A single scan could be done in approximately 45 minutes. In total, each of the six foils were scanned four times with fives background substrate scans between each foil scan.

We determined the average thickness in the 120-fold and 18-fold pattern locations by

averaging over the intersected area, see figure 4.1. The four scan pattern thicknesses were averaged and the scatter in the means gave the uncertainty for each foil.

	Foil					
Symmetry	#1	#2	#3	#4	#5	#6
18ω	$52.93 \pm .46$	$54.13 \pm .57$	$98.67 \pm .52$	$98.63 \pm .65$	$53.82 \pm .47$	$54.75 \pm .48$
120ω	$52.88 \pm .36$	$54.34 \pm .49$	$98.92 \pm .46$	$98.60 \pm .72$	$54.10 \pm .39$	$54.86 \pm .40$

Table 4.1: Touch-probe foil-thickness measurements [μm] in 18- and 120-fold wedge pattern regions for each platinum foil.

We employed this same touch-probe method for determining the thickness of the electrostatic shield. The nominally 10μm-thick beryllium-copper foil had a thickness of $9.2 \pm 0.5\mu$m.

4.2 Pattern Machining and Mass Removal

A stack of six foils, sandwiched between two 0.127mm thick beryllium-copper foils that provided additional stiffness to the stack, was cut with a wire-electric discharge mill (EDM). The stack was clamped between two several millimeter thick molybdenum plates with a set of dowel pin alignment holes and oversized versions of the wedge patterns. The oversized holes in the molybdenum provided additional stiffness to the stack. The final ordering of the stack was then:

1. beryllium-copper foil 1
2. Platinum foil 1 (50μm)
3. Platinum foil 2 (50μm)
4. Platinum foil 3 (100μm)
5. Platinum foil 4 (100μm)
6. Platinum foil 5 (50μm)
7. Platinum foil 6 (50μm)

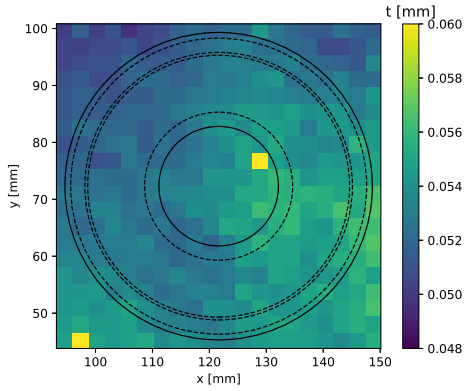

(a) Foil(2) original orientation.

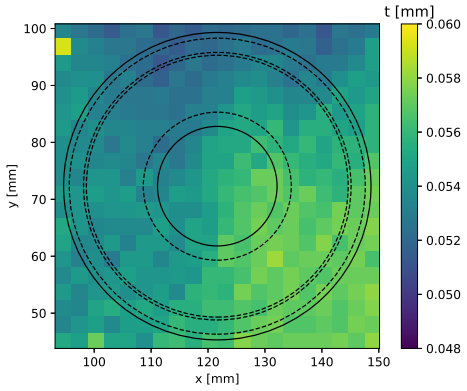

(b) Foil(2) flipped over.

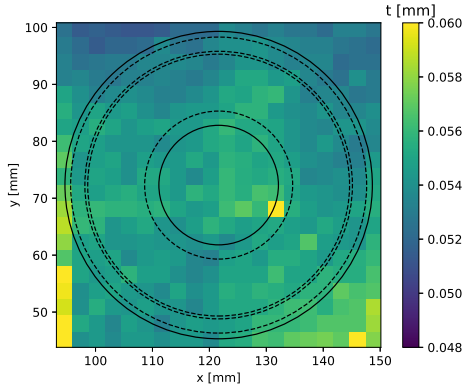

(c) Foil(2) rotated 90°.

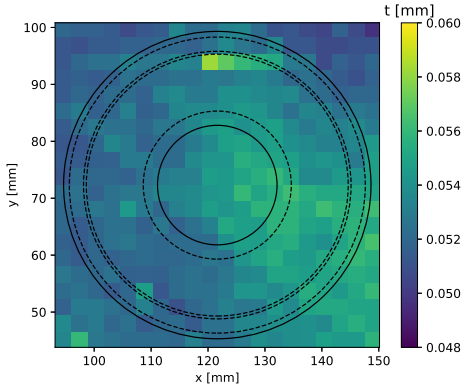

(d) Foil(2) original orientation.

Figure 4.1: **Four touch-probe scans of platinum foil-(2) with background touch-probe scan subtracted** - The x,y-coordinate offsets are arbitrary, coming from the touch-probe coordinates. The solid lines denote the region covered by the test-mass pattern, and the dotted lines denote the inner and outer radii of the 18- and 120-fold wedge patterns. The thickness measurements are averaged over the regions between dotted lines. Scans (b) and (c) have been corrected to match the orientation of scans (a) and (d).

8. beryllium-copper foil 2

The cutting procedure started with cutting a set of alignment holes into the stack that preserved the orientation of the foils and broke any rotational or inversion symmetry so that no foil would be flipped over or misaligned in any step between cuts. Additionally each foil received a set of identifying marks on a portion of the foil exterior to the final pattern to maintain the foil identification. Once the alignment holes and identifying marks were cut, the foils were returned from the shop, and were cleaned and weighed.

The cleaning and weighing were iterated until no more residue from the cutting was cleaned away and the weighings converged. The cleaning steps consisted of 15 minute rounds in an ultrasonic bath of isopropyl alcohol. The second set of cuts were the 18-fold pattern followed by a round of cleaning and weighing. It was discovered after the 18-fold pattern had been cut that a slight burr remained on the cut edge of the foils by using a stereo-microscope. The burrs were roughly 5-10μm in width and height. The burrs were persistent through ultrasonic cleanings in isopropyl alcohol or Na_2SO_8 (a copper etchant) but would easily flake off with a slight amount of force. Each cut edge was carefully inspected under the stereo-microscope and any burr was manually removed by gently touching with a wooden applicator to avoid scratching the rest of the platinum foil. The third set of cuts was the 120-fold pattern, again followed by a round of cleaning, weighing, and careful burr removal. Finally, the inner and outer cuts were performed one after the other, followed by one last round of cleaning and weighing.

The foils were weighed on a Sartorius LA310S analytical balance with 0.1mg resolution that is calibrated yearly by NorthWest Instrument Services. An extra piece of 50μm-thick platinum foil was cleaned and weighed in the same steps as the test-mass foils as a control, and a set of four class M2 calibration weights were weighed as well at each step to ensure the linearity of the balance. The total mass removed in the 18- and 120-fold patterns are given in table 4.2.

	Foil					
Symmetry	#1	#2	#3	#4	#5	#6
m_{18}	0.21732(10)	0.22402(8)	0.40671(12)	0.40955(10)	0.22235(8)	0.22302(11)
m_{120}	0.63469(12)	0.65749(13)	1.19204(10)	1.19856(13)	0.65248(15)	0.65369(11)

Table 4.2: Mass removed [g] in 18- and 120-fold wedge patterns in foils 1-6. These final values include a ≈.01% correction for buoyancy in air.

4.3 Pattern Geometry

We inspected the dimensions of the platinum foils with an OGP SmartScope to verify radial and angular dimensions of the slots before gluing to the substrate. To avoid systematic bias in the measuring microscope, each scan of a foil was repeated with the foil flipped about the y-axis and rotated by 90°. This maintained an equivalent layout of the wedge pattern, so the scanning routine did not have to be remade each time. The following data come from 12 sets of data, two for each of the six foils. The edge scan data gave a measure of the average radii, centers, and subtended angles for the wedge patterns.

4.3.1 Measurement

The foils were placed directly on the SmartScope table, which was wiped down with alcohol. A glass slide was placed on top of the foil and held in place with a weight to keep the foils flat, as the SmartScope moved in relatively quick and jerky movements. We measured each 18- and 120-fold wedge using the SmartScope edge-tracing routine.

The edge-tracing measurements gave a list of xy-positions which we separated into radial arcs and axial spokes for each of the relevant portions of the pattern. A single trace took approximately 4 hours and collected around 30,000 points with 100μm spacing, see figure 4.2.

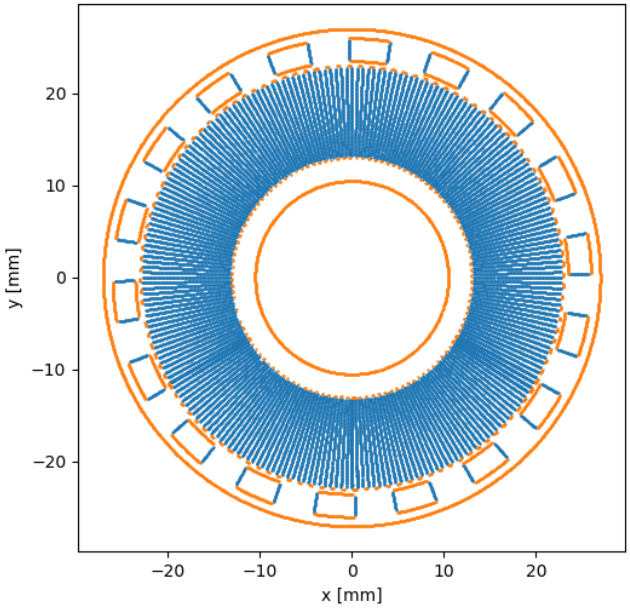

Figure 4.2: **Edge trace of platinum foil #4** - The points designated as the axial spokes are shown in blue and the points designated as the radial arcs in orange. We scanned each foil twice.

4.3.2 Radii and Concentricities

We determined the inner and outer radii of the wedge patterns for our torque calculations. Additionally, the 18- and 120-fold patterns were designed to be concentric, but limits in the ability to re-align the patterns when cut separately required us to measure this as well.

We measured if the patterns were concentric at the same time as determining the radii by separating out the radial portions of the traced edges and fitting to a circle. The inner and outer radii for each foil are given in table 4.3.

The center of the outer diameter for the inner wedges was assumed to be the center and was then subtracted from all of the data points. Additionally, flipped/rotated data was

	Foil					
Radius	#1	#2	#3	#4	#5	#6
Interior	10.4955(26)	10.4951(26)	10.4939(27)	10.4964(26)	10.4950(26)	10.4950(26)
IR_{120}	13.0049(57)	13.0032(50)	13.0043(48)	13.0046(52)	13.0045(49)	13.0032(59)
OR_{120}	22.9983(15)	22.9971(15)	22.9973(16)	22.9980(15)	22.9990(16)	22.9981(16)
IR_{18}	23.5057(11)	23.5052(11)	23.5054(11)	23.5062(11)	23.5049(11)	23.5047(11)
OR_{18}	25.9996(10)	25.9983(10)	25.9978(10)	25.9997(10)	26.0002(10)	25.9996(10)
Exterior	27.0094(6)	27.0091(6)	27.0088(6)	27.0103(6)	27.0095(6)	27.0092(6)

Table 4.3: Inner and outer radii [mm] of 18- and 120-fold patterns and inner and outer radius of test masses.

flipped/rotated in software to match to the un-flipped/rotated data.

As all 6 of the foils were cut in a stack at once, they all had the same offset in concentricity of the two wedge patterns. The scatter of the centers determined the location of the 18-fold pattern relative to the 120-fold pattern.

	Foil					
Symmetry	#1	#2	#3	#4	#5	#6
$\Delta c_{18,120}$	9.3±1.1	6.8±1.1	8.6±1.0	10.2±1.1	7.8±1.1	6.6±1.1

Table 4.4: Difference in center locations [μm] of 18- and 120-fold wedge patterns for each foil given.

4.3.3 Subtended Angle

The angle subtended by the wedges in the 120-fold and 18-fold patterns decreases the torque amplitudes like cosine of the difference from the nominal angle. The radial portions of each

wedge were separated into subsets and the fit center removed. The subtended angle was fit by converting to polar coordinates, averaging the angle value of each edge, and taking the difference between every other adjacent edge, given in table 4.5.

	Foil					
Symmetry	#1	#2	#3	#4	#5	#6
β_{18}	9.9842(14)	9.9809(15)	9.9796(14)	9.9837(13)	9.9876(10)	9.9854(19)
β_{120}	1.4879(11)	1.4915(7)	1.4895(8)	1.4895(9)	1.4914(8)	1.4904(8)

Table 4.5: Subtended angle [degrees] of removed wedges in each of the patterns in degrees.

4.3.4 Overcut Parameter

The Smartscope measurements of the subtended angles and inner and outer radii were both subject to an uncertainty due to the ability to locate the edge of the wedge patterns. Our gravitational torque measurements only cared about the average location of the masses in the wedges, but the optical edge-tracing method used for the Smartscope measurements was more likely to see protruding burrs in the pattern edges and not divots. We accounted for this bias in our measurements by defining an overcut parameter, ϵ, that accounted for the roughness of the edges. The subtended angles were quadratic in the overcut error whereas the radii had a linear dependence. We made a crude estimate of the overcut from the fit residuals of the radial points by comparing their median to the average, $\epsilon = 0.2 \pm 0.4\mu$m.

4.4 Gluing Procedure

Because the thin platinum foils were not self-supporting, they had to be rigidly mounted to an NBK-7 glass substrate. We decided to completely fill the slots in the wedge pattern of the foils with the epoxy that would attach the foils to the substrate. The resulting flat surfaces of the mounted test-masses simplified the models of the gravitational torques and

the electrical capacitances of the test-bodies. The requirements were to completely fill the wedges while maintaining the flatness of the substrate and foils and to avoid imparting dust or bubbles in the epoxy.

A low viscosity epoxy, Stycast 1266, was chosen, inspired by work done by Weld in [59]. Stycast 1266 is a two component low-viscosity epoxy with a resin (Part A), and hardener (Loctite Catalyst 23LV, inadvertently substituted for Part B), that allowed it to completely fill the wedge slots. And, because it cures at room temperature, there was less likelihood of the test-mass warping due to thermal stresses. The flat surface was achieved by gluing the platinum foil to the glass substrate pressed against an optical flat but with the requirement that it not adhere to the optical flat. Again, a practical solution was found by Weld, who pressed against a flat sheet of thin aluminum foil on the optical flat. Because the epoxy did not adhere well to the aluminum foil, the foil could be peeled away once the epoxy had cured. We followed this strategy with several types of foils including various thicknesses, tempers, and types of foil to find one that left a smooth finish and peeled away easily. We found the best results using a 0.071mm thick copper foil from McMaster-Carr.

The gluing procedure was as follows. Approximately 5g of the epoxy resin was placed in a small glass vial and pumped under low vacuum, 1e-3 Torr, for at least 30 minutes. After pumping, 28% by weight of Catalyst 23LV was added to the vial along with a glass sealed magnetic stirrer. The two components were mixed under roughing vacuum for 10 minutes to thoroughly mix the two components and to allow any gas from the mixture to be pumped away. This procedure clearly reduced the number and size of bubbles evolving from the mixture.

Each platinum foil was glued with Stycast 1266 under about 200lbs of force between optical flats to an NBK-7 glass disk. The final gluing assembly was a layered stack as follows: a large optical flat with a thin Teflon sheet beneath to prevents scratches, a sacrificial 0.071mm thick copper foil, roughly ten drops of mixed Stycast 1266, the patterned platinum foil pressed into the glue with glass stirrer, the glass annulus substrate, a 27mm diameter optical flat with thin Teflon sheet underneath to prevent gluing to the glass annulus, and

finally an aluminum disk with cylindrical hole with a 3/4" steel ball seated in the hole to make contact with the press. The stack was assembled in a jig that aligned the centers of the test-mass foil and glass substrate with two U-shaped rectangular Teflon blocks. The teflon blocks were clamped in position once the pieces were aligned, see figure 4.3a. The epoxy did not adhere well to the Teflon and could therefore be removed once cured. Every step aside from the pumping under vacuum and the pressing was performed in a laminar flow hood to avoid allowing dust into the mixture.

The use of Catalyst 23LV was a mistake that still worked. The Safety Data Sheet (SDS) suggests Catalyst 23LV is nearly the same as the Stycast 1266 hardener but with the addition of polypropylene glycol diamine, a non-ferromagnetic molecule. The mistake was initially unnoticed since the epoxy still hardened and adhered to the glass incredibly well. Because there was the possibility of a slight difference in density from that reported in the datasheet, we explicitly measured the epoxy density, see below.

4.5 Surface Scans

Foils #2 and #3 were glued to 3mm glass substrates to serve as pendulum test-masses, and foils #1 and #4 were glued to 5mm glass substrates to serve as attractor test-masses. The test-masses were then gold-coated by a sputter source with approximately 100nm of gold with a titanium adhesion layer. We measured the surface roughness off of the reflective surface with the SmartScope laser distance probe in a non-contact manner. The surface scans gave a rough estimate of the prevalence of bubble defects in the glue, heights of the wedges relative to the glue filling, warping of the test-mass, surface roughness, and the thickness of the residual glue film.

Bubbles in the glue left holes down to the glass substrate that were visible in the scan. The volume was estimated by summing the total number of scan points well below the surface and multiplying by the area spacing between scan points. The estimated bubble volume in the glued foils was less than 0.3 mm^3 and lead to a $< 1\%$ effect on the nominal density of the glue and therefore $< 0.1\%$ effect on the torque amplitudes.

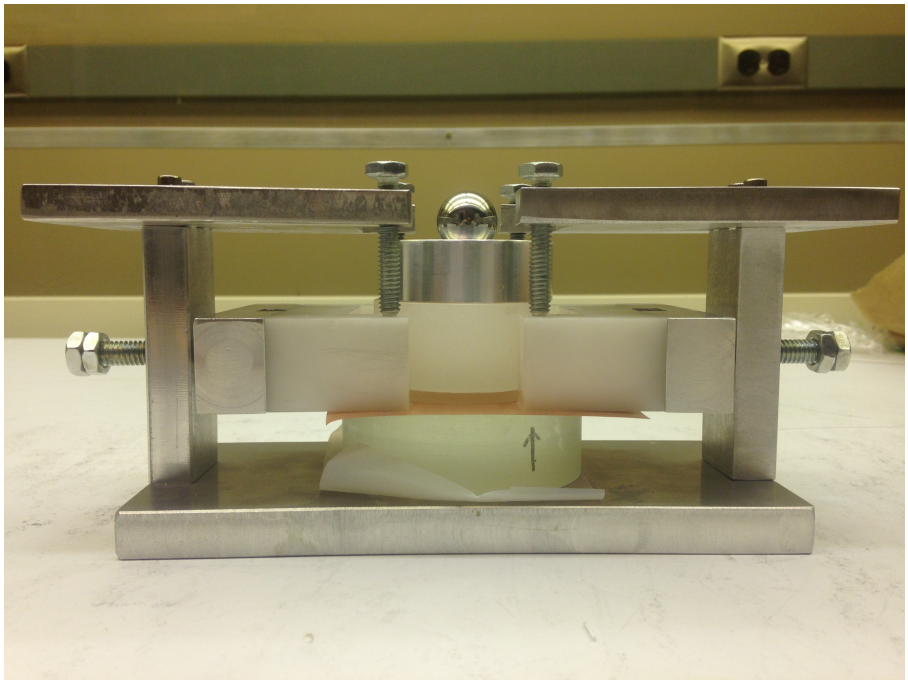

(a) Side view of gluing jig.

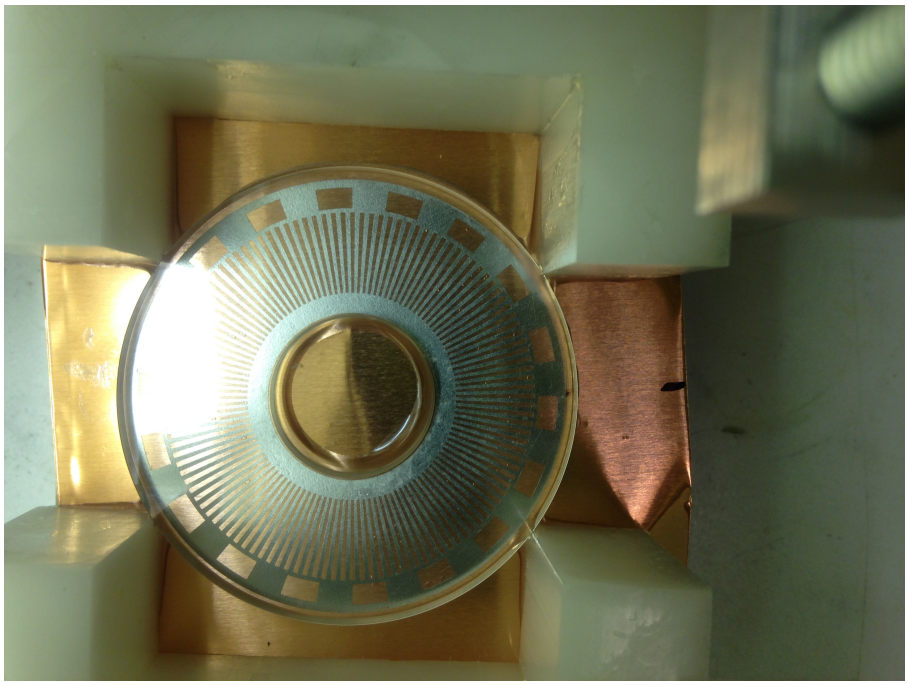

(b) Top view of gluing jig.

Figure 4.3: **Gluing jig** - The sacrificial copper foil was part way through removal from the right-hand side of the lower image. The square Teflon clamps centered the glass disk above the platinum foil.

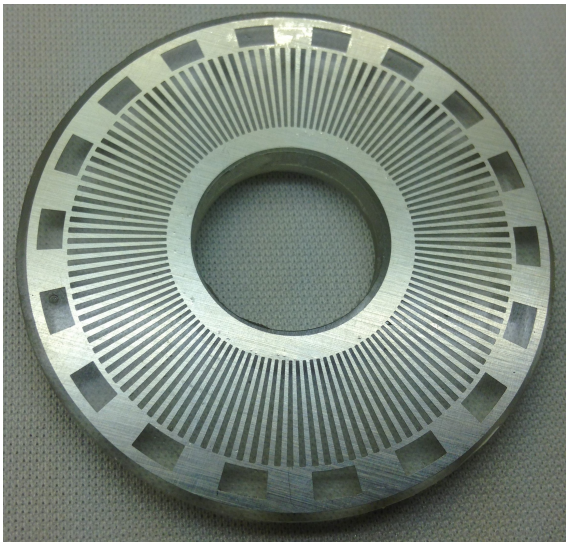

(a) Epoxied test-mass, foil-(4).

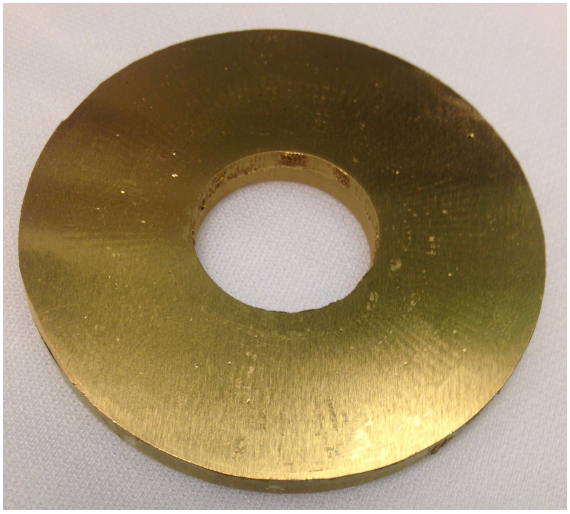

(b) Gold-coated test-mass, foil-(2).

Figure 4.4: **Photos of glued and gold-coated test-masses**

It was also visible by eye that the glue surface over the holes was slightly depressed compared to the glue film over the platinum. Points between the inner and outer radii of the wedges were selected and the average depression was determined, as noted in table 4.6. These values were included in the source modeling but contributed negligibly to the predicted torque.

	Foil			
Symmetry	#1	#2	#3	#4
18ω	1.7(2)	1.6(2)	2.3(3)	1.7(3)
120ω	0.21(1)	0.53(1)	0.77(1)	0.38(1)

Table 4.6: Difference in surface height of platinum wedge to glue-filled wedge in μm.

We chose test-masses #2 and #4 to serve as the pendulum and attractor. There was a

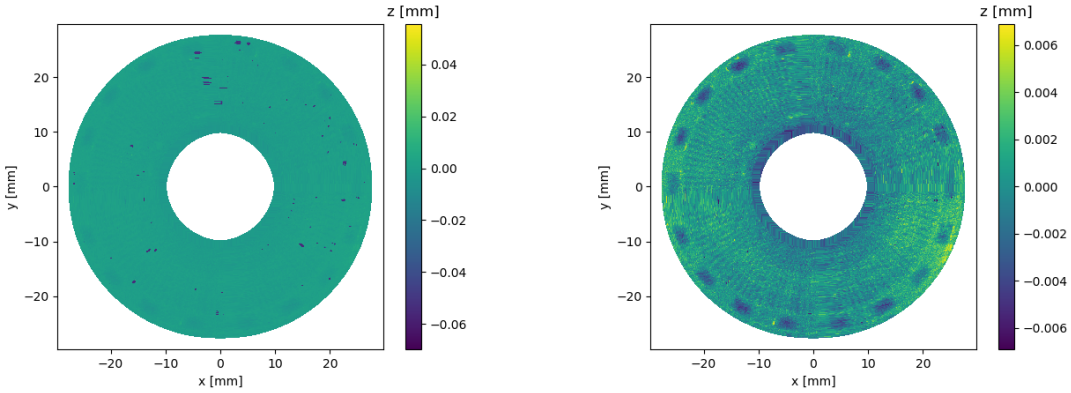

(a) Plane-subtracted scan of glued 50micron thick platinum foil #1 on 5mm thick glass annulus.

(b) Scan of glued 50micron thick platinum foil #1 on 5mm thick glass annulus with variance cut to view fine-details.

Figure 4.5: **Scan of the pendulum test-mass surface** - The scan on the left has the offset tilt plane subtracted. Some bubbles are visible in the glue, going down 50μm to the glass substrate. There are additionally some bits of dust or scatters from the measurement that read high. The right-hand image has an additional variance cut at 2.5σ on height and shows small dips in between the platinum wedges.

2.3μm "potato chip" warping of the pendulum test-mass surface and approximately 2.3μm RMS surface height variation. The attractor test-mass showed $< 1\mu$m of warping with only 1.5μm RMS surface height variation.

It was also possible to find small a location where the copper foil had peeled away some of the glue from the platinum surface on both the attractor and pendulum test-masses. This allowed us to estimate the thickness of the residual epoxy film on the surface of the test-masses. We compared the average height of the region free from glue to a nearby region with the glue film still present, see figure 4.6. The resulting measurements of the residual glue thickness are given in table 4.7.

Test-mass	Glue Film Thickness [μm]
#2	1.3 (0.5)
#4	2.6 (1.2)

Table 4.7: Thickness of residual glue film on top of test-mass platinum foil after gluing given in μm.

4.6 Epoxy Density

The density of Stycast 1266 was given in the datasheet as 1.12 g/cm^3, but our use of the wrong hardener required a separate measurement of the glue density. To verify the density, a separate batch of glue was mixed in the same degassing and stirring procedure as in the preparation for the foil gluing. The epoxy was poured into a Teflon container and allowed to cure. We extracted the cured epoxy from the Teflon container and cut a cylinder on a lathe.

The cylinder was weighed on the same Sartorius LA310S analytical balance. The height and diameter were measured with a Mitutoyo 389-711-30 digital micrometer. The density could be determined to better than a percent to be 1.162 $\pm$ .004 g/cm^3, see table 4.8. This was a 3% difference from the nominal correctly mixed Stycast 1266. The transparent test-

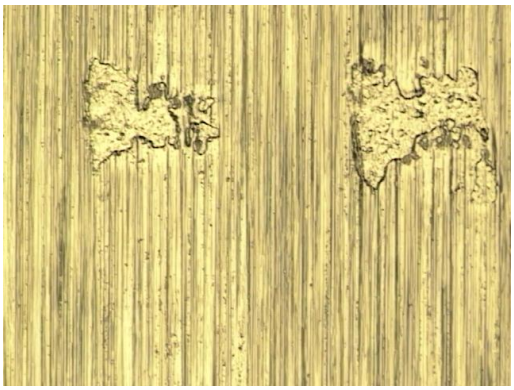

(a)

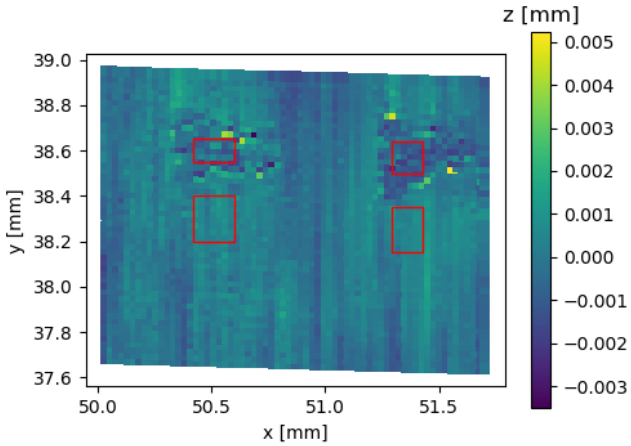

(b)

(c)

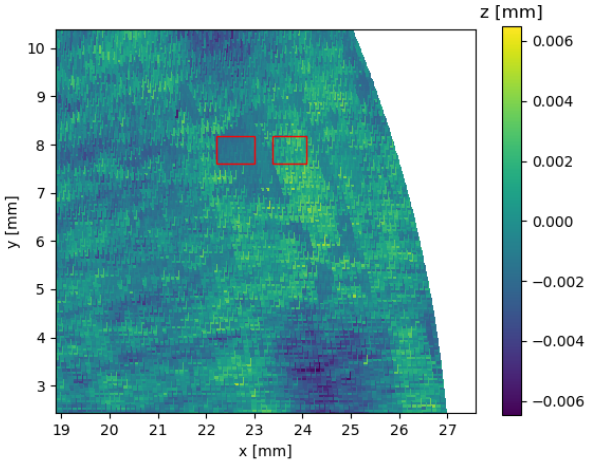

(d)

Figure 4.6: **Glue free regions of test-masses** - These regions of pendulum and attractor test-masses (a, c) with glue-free platinum surfaces were scanned with the Smartscope. The surface-scans (b, d) were used to estimate the thickness of the glue film above the test-mass surface by comparing the height in the regions enclosed by the red boxes.

Quantity	Value ± Uncertainty	unit
Mass	5.7216 ± .00005	g
Buoyancy	0.006 ± .001	g
Diameter	19.168 ± .017	mm
Height	17.076 ± .006	mm
Thermal Expansion	0.000 ± .0003	mm
Density	1.162 ± .004	g/cm^3

Table 4.8: Stycast 1266 density measurement.

sample had no apparent bubbles in comparison to the glued test-masses that could trap bubbles in between the wedges.

Chapter 5

ALIGNMENT

Many aspects of this experiment depended heavily on precise alignment of the source and detector: the smallest achievable separations were possible only when all surfaces were nearly parallel, torque sensitivity relied on centering both pendulum and source on the turntable axis, and simple torque calculations relied on cylindrical symmetry of the test-mass arrangement. The various alignments were made by adjusting four angles and two radial offsets, see figure 5.1. The angles were the tilt of the pendulum test-mass relative to the vertically hanging fiber Ψ_P, the tilt of the attractor test-mass relative to the turntable rotation axis Ψ_A, the tilt of the screen relative to the turntable rotation axis Ψ_S, and the angle of the screen relative to vertical Ψ_V. The first radial offset was the displacement of the center of the attractor test-mass from the turntable rotation axis $\vec{r}_A(\phi)$, which changed orientation with the turntable angle ϕ. The second radial offset was the displacement of the center of pendulum test-mass from the turntable rotation axis $\vec{r}_P$. In every angular alignment, we measured $\widetilde{\Psi}_X = \Psi_X - \pi/2$ as the deviation from perpendicular. Ultimately, we measured torques as a function of the separation between the pendulum and attractor test-masses. The measurement and alignment of these parameters is described here along with a description of our methods for determining the separation between the test-masses

5.1 Pendulum Perpedicularity

The torque sensitivity was maximized when the bottom surface of the pendulum test-mass was perpendicular to the fiber axis and varied as $\cos(\widetilde{\Psi}_P)$. This angle could also limit the minimal achievable separation between the pendulum and the electrostatic screen, and its perpendicularity was measured as follows. The usual electrostatic screen was removed and

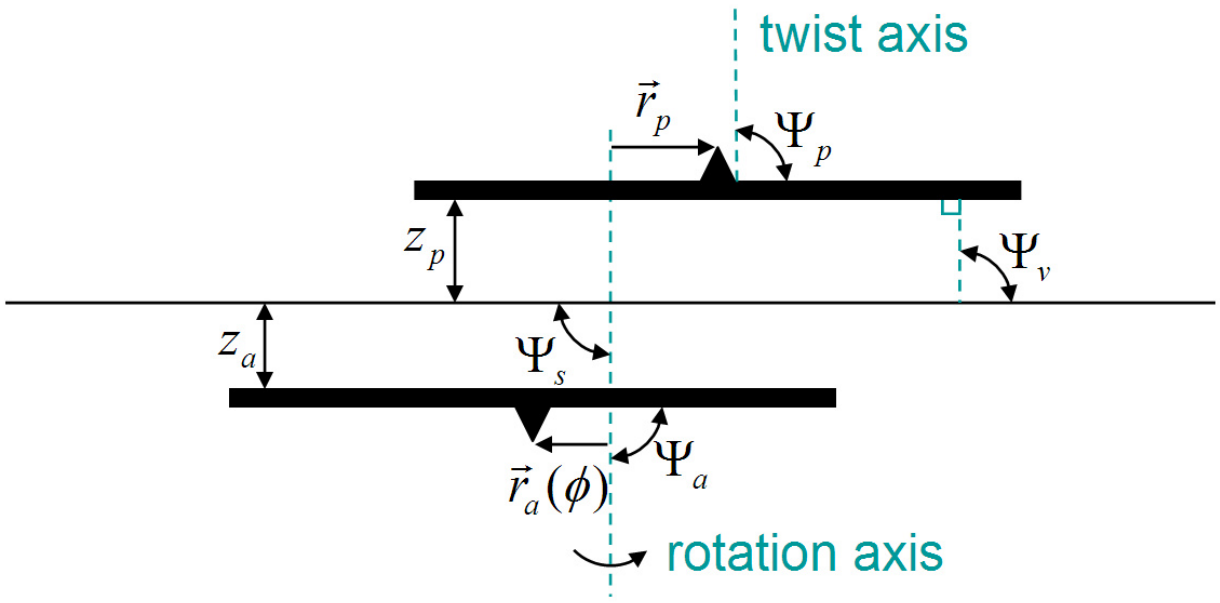

Figure 5.1: **Diagram of experimental alignment parameters as given in [19] page 70** - In every angular alignment, we measured $\widetilde{\Psi}_X = \Psi_X - \pi/2$ as the deviation from perpendicular.

replaced by a split copper plate. The pendulum was driven with a sinusoidal voltage and the currents from the two resulting capacitors formed from the pendulum with either half of the plate were converted to voltages, amplified, and measured with lock-in amplifiers in the out-of-phase component relative to the drive modulation signal. As the pendulum rotated through a complete revolution, the difference between the two capacitance values was sinusoidally modulated proportional to the tilt of the test-mass relative to vertical. The measurement was independent of the tilt of the split plate relative to vertical which only appeared as a DC offset in the difference signal.

The pendulum was leveled by adjusting the four screws that tilted the "top-hat" portion of the pendulum on a wave-washer clamped above the mirror. The tilt screws were adjusted to minimize any modulation in the difference signal from the pendulum oscillation. We

quantified the residual tilt by inducing a known tilt on the pendulum, accomplished by placing a small brass nut on the edge of the glass disk of the test-mass. A calculation of the change in center of mass from a 0.01970g #00-90 brass nut induced a 215μrad tilt. Our measurements, figure 5.3, show that the pendulum disk was leveled to $\widetilde{\Psi}_P = 82 \pm 9\mu$rad. The reduction in lever-arm from the test-mass tilt reduced the torque by a factor of $(1 - 4 \times 10^{-9})$ which was entirely negligible. This tilt was equivalent to a 2.5μm change in pendulum-screen separation at the edge of the test-mass relative to the average test-mass separation. The pendulum could not be leveled much further as the 1ω pendulum twist signal was diminished to roughly the same amplitude as the 2ω twist signal from the hyperbolic curvature of the test mass. This parameter was held fixed once the experiment was put under vacuum.

5.2 Runout

The attractor test-mass sat on a tip-tilt stage centered by three phosphor-bronze #4-40 screws on the turntable. These centering screws allowed us to adjust the position of the attractor test-mass relative to the turntable rotation axis $\vec{r}_A$, hereafter referred to as runout. We knew from measurements of the test-mass pattern geometry that the center of the 18- and 120-fold patterns disagreed by $\Delta c_{18,120} = 8.3 \pm 3.3\mu$m. Because the 120-fold torque was more sensitive than the 18-fold torque to radial misalignment, we centered on the 120-fold pattern.

To measure the runout, we mounted the turntable on the SmartScope, and aligned the optics such that a line tangential to the outer edge of a single 120-fold wedge was aligned with the x-axis. We then rotated the turntable by hand, re-centering the cross-hairs above every fifth 120-fold wedge by moving only along the y-axis. Any runout appeared as a sinusoidal change in the y-axis value with the turntable rotation.

The new method of fabricating the test masses with glue-filled wedges lead to significant difficulty in determining the radial alignment. Some of the wedges were easily discernable by eye, but to ensure we found each wedge, we placed an angular scale on the turntable in order to make 15° turns.

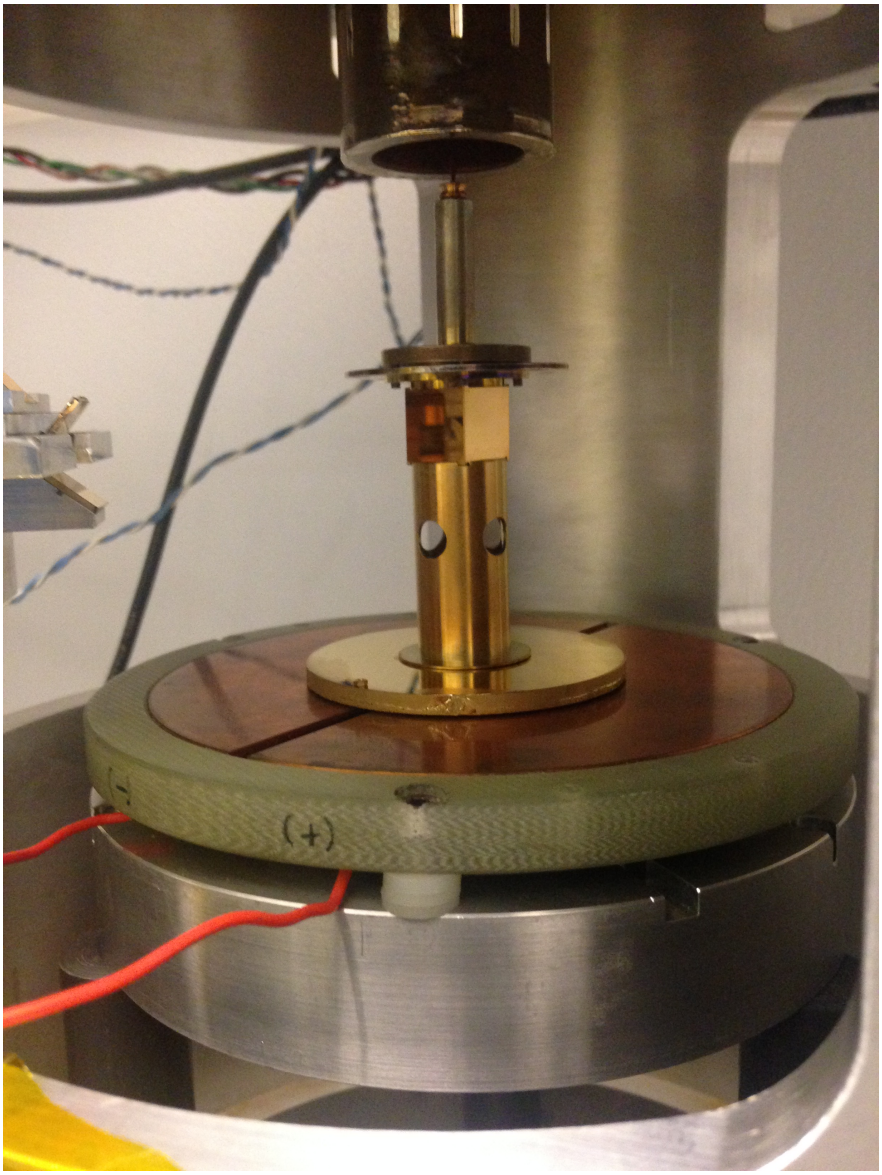

Figure 5.2: **Pendulum suspended above a split copper plate to form two capacitors** - The pendulum was driven with 1V at 1kHz to drive current through the wires connected to either end of the split plate. The current was measured with a lock-in amplifier and allowed us to measure the tilt of the pendulum test-mass. A brass nut used to calibrate the tilt is visible at the edge of the test-mass.

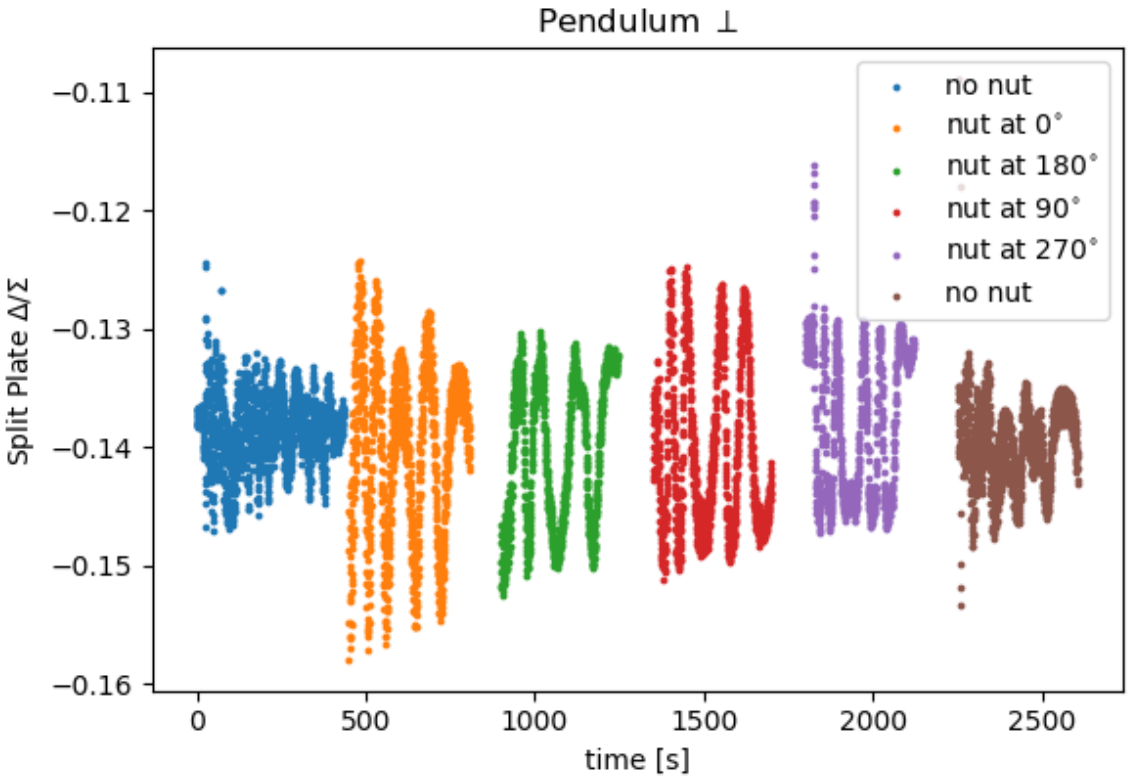

Figure 5.3: **Pendulum perpendicularity measurements and calibration** - Plots of the pendulum oscillation over the split-plate capacitor without the calibration weight (blue), with the calibration nut at 0° relative to a mark on the glass disk (orange), with the calibration nut at 180° (green), at 90° (red), at 270° (violet), and without the calibration weight again (brown). The decaying amplitude present in all of the measurements comes from air damping of the swing mode after the initial excitation. The spike at the beginning of the last two measurements arises from the initial excitation of the twist amplitude.

The centering errors were estimated from our ability to return to the same position. The process was repeated for the 18-fold pattern with 20° turns as a verification. We were able

to minimize the 120ω runout to $r_A = 7.5 \pm 1.8\mu$m, see figure 5.4, which was fixed for the duration of the experiment.

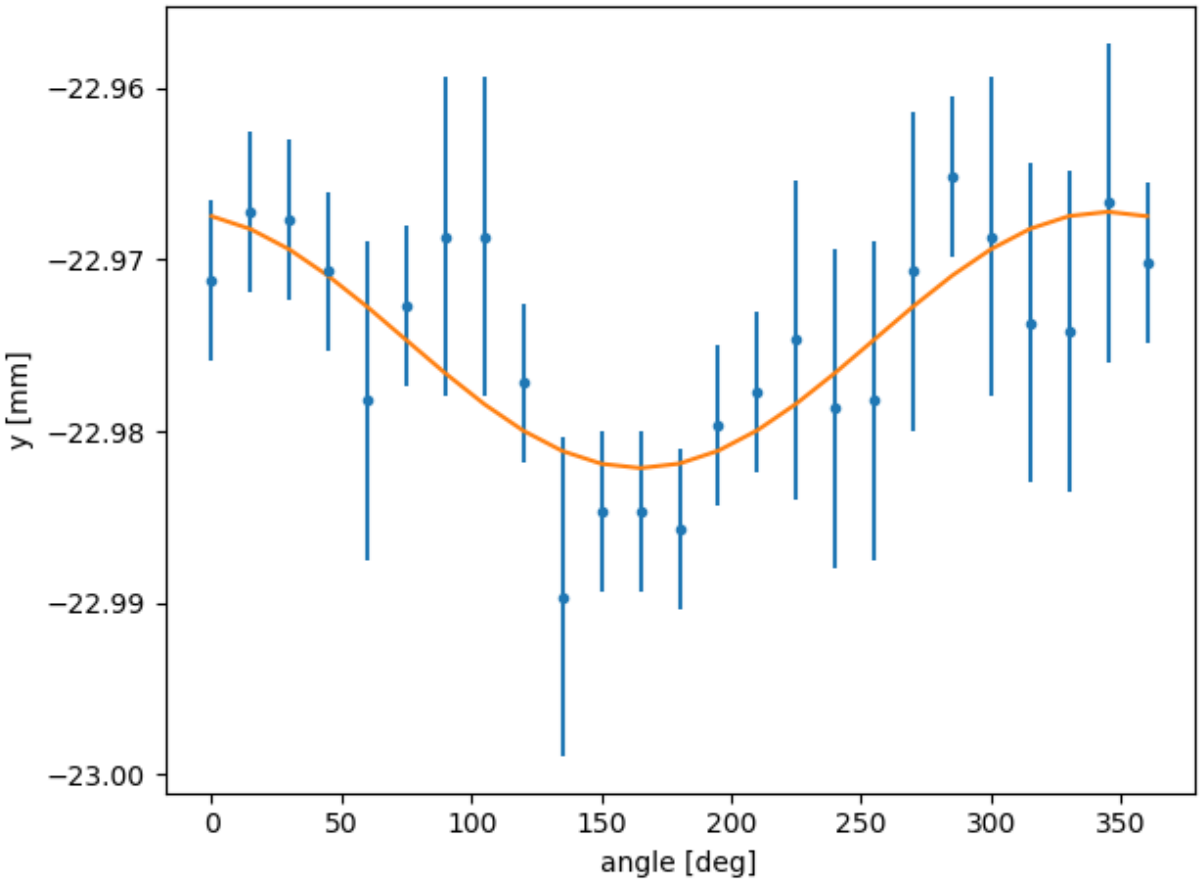

Figure 5.4: **Attractor runout** - Measurements of the displacement of 120-fold wedges along the y-axis of the measuring microscope vs. turntable angle determined the attractor runout. The errors were estimated from our ability to return to a single wedge position multiple times.

5.3 Turntable Leveling and Bearing Rumble

The minimum attractor-screen separations depended on the perpendicular alignment of the source mass to the turntable axis. Imperfections in the bearings also could lead to vertical displacements of the source mass with angle. The non-perpendicularity of the source mass with respect to the rotation axis (wobble) and the vertical displacement of the test-mass with rotation (rumble) were measured with the SmartScope. The turntable was mounted on the measuring microscope and the surface height measured over two patches on opposite sides of the test-mass, near the outside edge of the pattern. We measured the surface height by reflecting a laser off the reflective gold surface of the source mass. We rotated the attractor through twelve angles by hand and the difference in height of opposite patches determined the wobble while the average of the heights determined the common-mode rumble in the bearings.

The source mass was made perpendicular to the turntable axis by adjusting three #0-80 screws on the top half of the source "cup". This was a slight change from the previous version in that it decoupled the adjustment of the leveling from the radial alignment on the turntable, although the opposite did not hold, i.e. radial adjustments still affected leveling, see figure 3.2. Bearing rumble could not be adjusted. We were able to decrease the wobble to an approximately 2.5μm amplitude over the 27.5mm radius which we held fixed for the duration of the experiment.

5.4 Tilted Plate Approximation

Many of our alignments required parallelizing flat conductive plates. A simple approximation to the capacitance of a tilted plate against an infinite conductive plane serves to illustrate our methods. The capacitance from a disc parallel to an infinite sheet can be found by integrating over infinitesimal area elements divided by the separation over ϕ from $-\pi/2$ to $\pi/2$. If $\phi = 0$ is along the x-axis, divide the disc into strips along the x-axis, with length along x, $2R\cos\phi$, and width along y, $d(R\sin\phi) = R\cos\phi d\phi$.

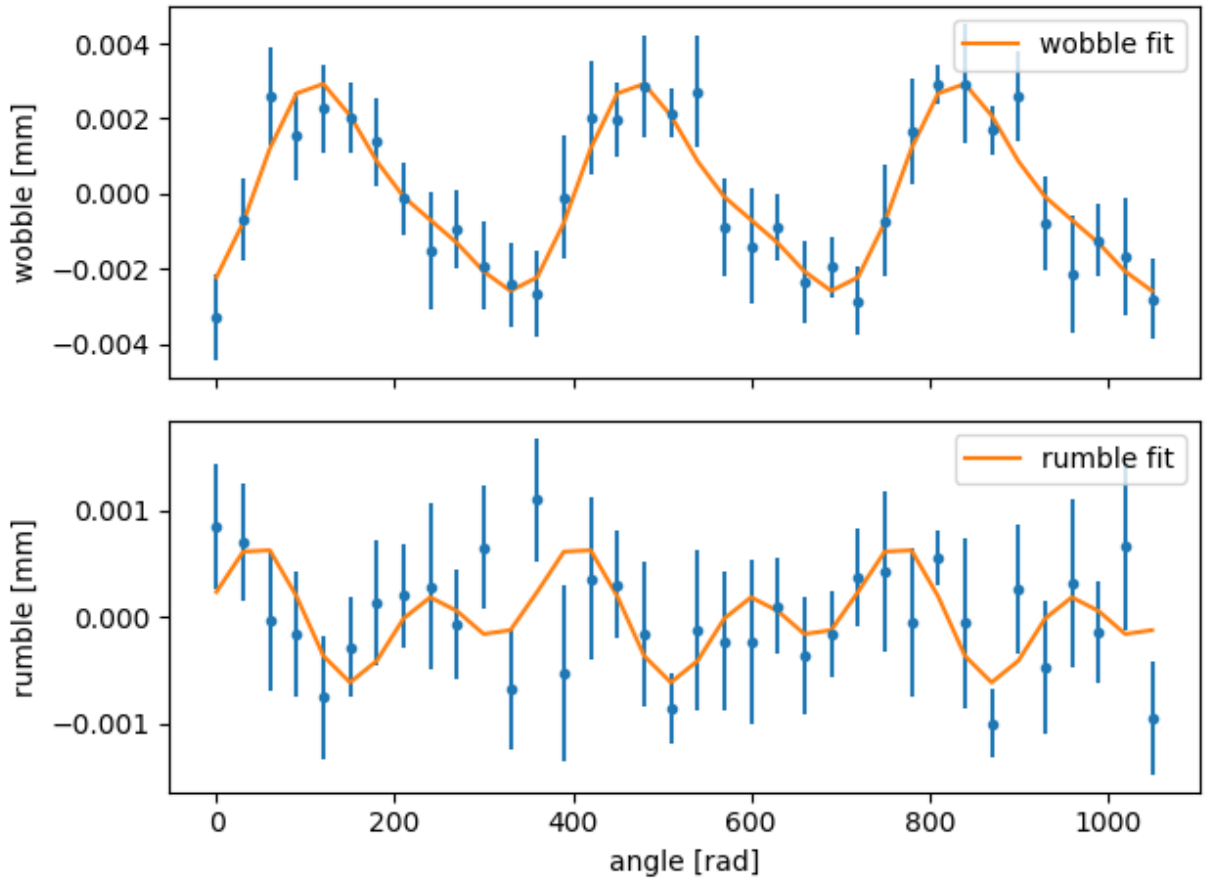

Figure 5.5: **Non-Perpendicularity of attractor foil to rotation axis: height displacement vs turntable angle** - Measurements of the test-mass surface height at points opposite each other were taken at 12 turntable angles over 3 rotations. The fit is to the first two harmonics of the rotation in the difference (wobble) and average (rumble) of the height displacement.

$$\begin{aligned} C_u &= \epsilon_0 \int_{-\pi/2}^{\pi/2} \frac{2R\cos\phi \;\; R\cos\phi d\phi}{d} \\ &= \epsilon_0 \int_{-\pi/2}^{\pi/2} \frac{2R^2\cos^2\phi}{d} d\phi \\ &= \frac{\epsilon_0 \pi R^2}{d} \end{aligned} \tag{5.1}$$

Now we want to find the extrema of the capacitance as the disc is rotated through 360°. Without loss of generality we can assume the plate is tilted about the rotation axis by α and the disc is tilted by β, both along the y-axis. The area stays the same to first order in α and β, but the distance becomes a function of ϕ.

$$\overline{d} = d + R\sin(\phi)\sin(\alpha - \beta)$$

If we assume $\alpha, \beta \ll 1$:

$$\overline{d} = d + R\sin(\phi)(\alpha - \beta)$$

We expand out to second order in both α and β and integrate in ϕ yielding:

$$C = \epsilon_0 \pi \left(\frac{R^2}{d} + \frac{R^4(\alpha - \beta)^2}{4d^3} \right) = C_u \left(1 + \frac{\Delta C_c}{C_u} + \frac{\Delta C_{1\omega}}{C_u} \right)$$

Two things stand out:

1. There is a constant offset of $\Delta C_c / C_u = \frac{R^2(\alpha^2+\beta^2)}{4d^2}$
2. If the disk rotates, i.e. $\overline{\alpha} \in (-\alpha, \alpha)$. The 1ω amplitude goes like $\Delta C_{1\omega}/C_u = \frac{R^2 \alpha\beta}{2d^2}$

We used the quadratic dependence of the capacitance between tilted planes to align the electrostatic screen to the attractor and pendulum test-masses.

5.5 Attractor-Screen Leveling

One major upgrade of this iteration of the experiment over the previous, was the addition of three Physik Instrumente M-227K063 vacuum compatible actuators with 10mm of travel and 1μm repeatability that supported the electrostatic screen. These actuators allowed us make the screen perpendicular to the attractor rotation axis in-situ and additionally to perform scans of capacitance vs actuator position to verify the attractor-screen separation.

The leveling procedure was to tilt the screen at a fixed attractor-screen separation z_A in order to minimize their capacitance along two axes, see figure 5.6. This was performed iteratively over smaller screen tilt angles and at smaller z_A. To account for the residual tilt of the attractor test-mass to its rotation axis, we leveled the screen at various turntable

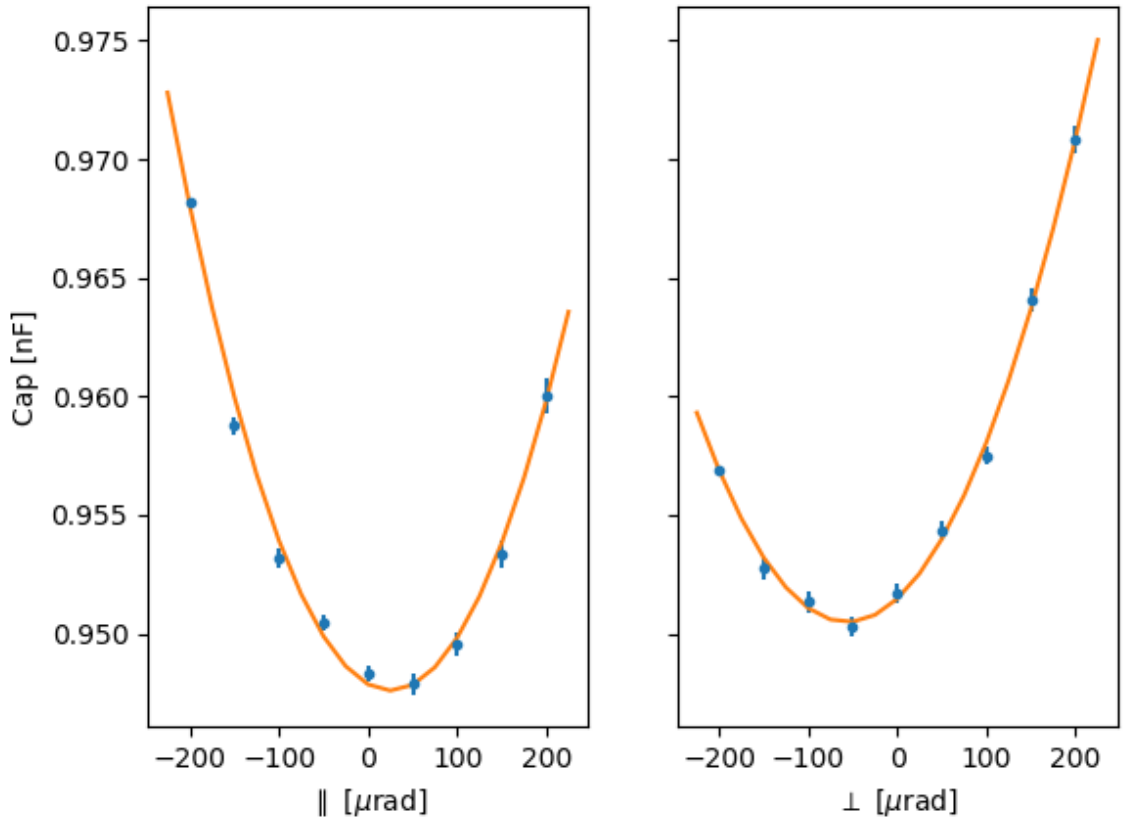

Figure 5.6: **Attractor-screen capacitance dependence on screen tilt along orthogonal axes** - The screen was tilted along axes parallel and perpendicular to actuator-0 to align the screen to the attractor test-mass. The capacitance minimum occurred where the surfaces were parallel.

angles. When the screen was perpendicular to the rotation axis, leveling to the attractor would require a screen tilt of $\Delta\widetilde{\Psi}_S = \widetilde{\Psi}_A$ along one direction and a tilt of $\Delta\widetilde{\Psi}_S = -\widetilde{\Psi}_A$ with the turntable rotated 180°, see figure 5.7. We measured the tilt necessary to align the screen to the attractor at various turntable angles (see figure 5.8), and found the attractor tilt was $\widetilde{\Psi}_A = 54 \pm 9$ μrad and the screen tilt was $\widetilde{\Psi}_S = 0 \pm 18\mu$rad.

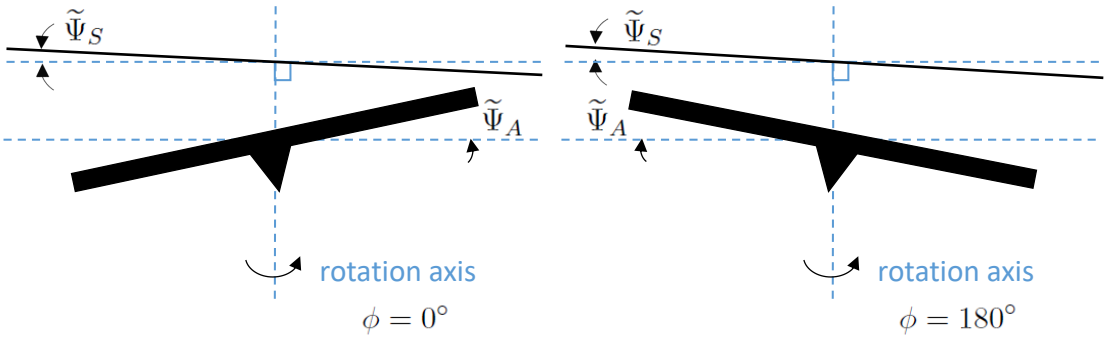

Figure 5.7: **Attractor-screen tilt alignment at opposite turntable angles** - We aligned the screen to the attractor test-mass at various turntable angles. When perpendicular to the rotation axis, the change in the screen tilt to match the attractor test-mass at opposite turntable angles was equal and opposite. In the above example, the screen must be tilted by $\Delta\widetilde{\Psi}_S = \widetilde{\Psi}_S + \widetilde{\Psi}_A$ at $\phi = 0°$ and by $\Delta\widetilde{\Psi}_S = \widetilde{\Psi}_S - \widetilde{\Psi}_A$ at $\phi = 180°$

5.6 Pendulum-Screen Leveling

After the screen was made parallel to the attractor, we aligned the screen to be parallel to the pendulum disk. The pendulum was lowered near the screen and the entire apparatus was tilted via stepper motors controlled remotely via an Arduino Uno attached to leveling screws at two of the the three feet of the apparatus support. The capacitance between the pendulum and screen was monitored as a function of apparatus tilt, measured with the Applied Geomechanics Instrument (AGI) tiltmeters. The capacitance was roughly quadratic in the difference in tilt angles, and so was minimized when the two surfaces were parallel,

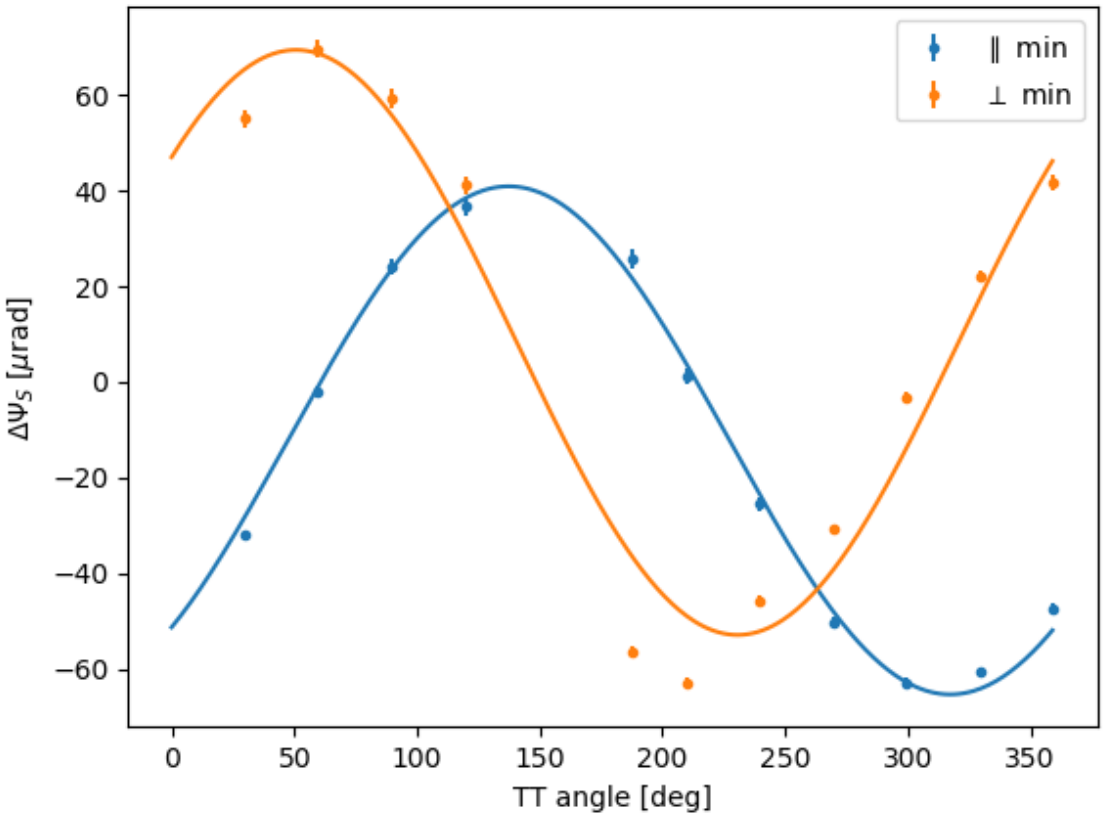

Figure 5.8: **Change in screen tilt to match attractor at various turntable angles** - We aligned the screen to the attractor test-mass at various turntable angles. At each angle, the screen was tilted along axes parallel and perpendicular to actuator-0 to find the capacitance minimum. The change in screen tilt to align to the test-mass with turntable angle gave a measure of attractor wobble and residual tilt of the screen relative to the rotation axis.

see figure 5.9.

Over the course of data taking, we measured the apparatus tilt drift, figure 5.10. The change in tilt affected the centering of the pendulum test-mass on the turntable axis, $\vec{r}_P$, due to the meter long fiber. The change in center was related to the change in center position by

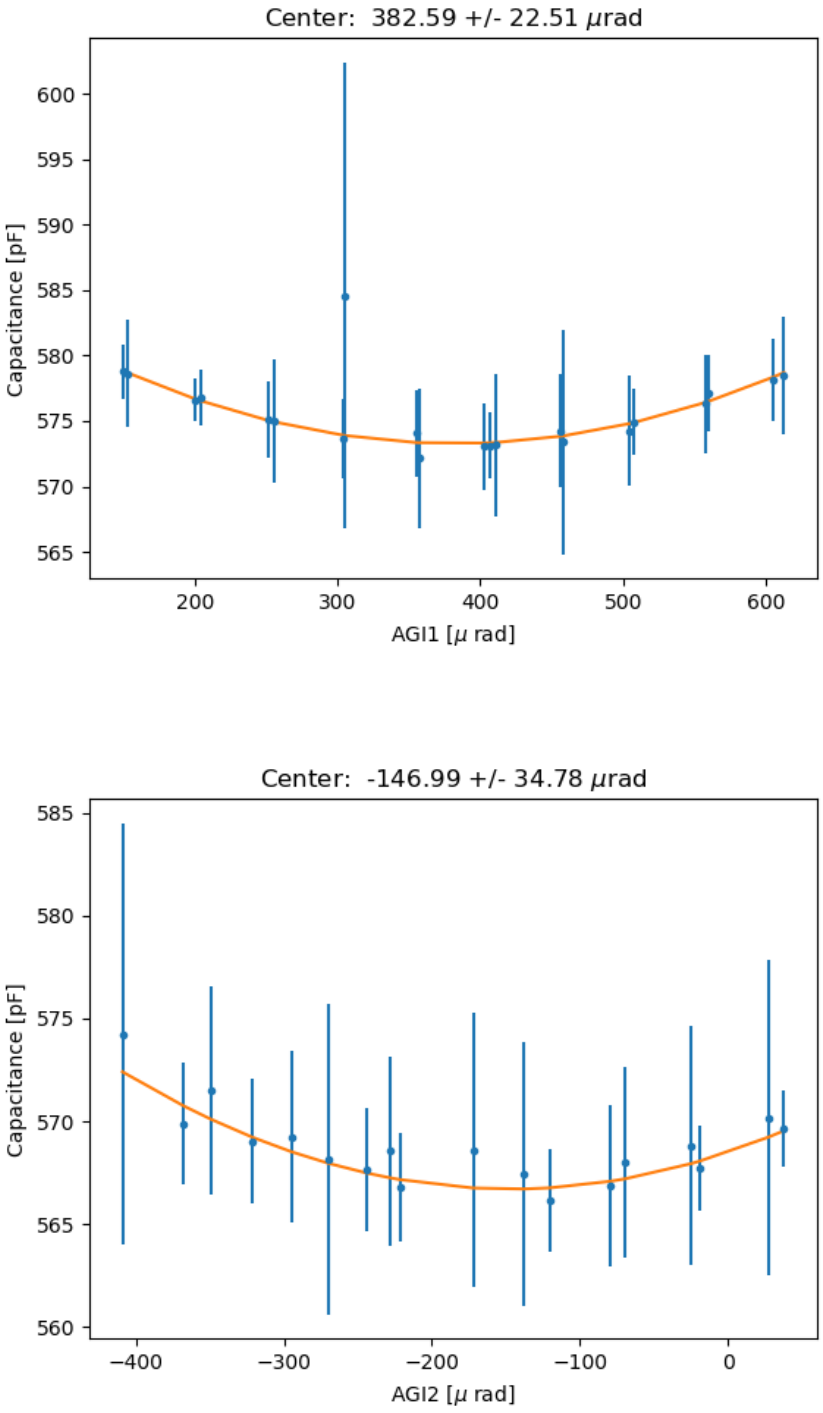

Figure 5.9: **Capacitance as a function of apparatus tilt along two axes** - We tilted the apparatus to align the pendulum and screen by finding the minimum in capacitance. Each AGI tiltmeter axis was effectively independent of the 120° opposite axis when tilted along the corresponding support leg.

$$\Delta x_0 = -L_f \frac{\sqrt{3}}{2} \Delta\theta_2$$
$$\Delta y_0 = L_f \left(\Delta\theta_1 + \frac{1}{2} \Delta\theta_2 \right)$$

where L_f is the length of the fiber, and $\Delta\theta_1$ and $\Delta\theta_2$ correspond to the change from vertical as measured along the axes of the AGI. This effect was verified by taking science data with the pendulum test-mass displaced by 100μm radially from the turntable rotation axis, and then taking a second set of data with the apparatus tilted to shift the turntable axis under the pendulum test-mass.

The apparatus was only re-leveled once between 170 and 175 days into the dataset when the ion pump failed and the apparatus was re-baked. After re-locking the ion pump, the apparatus was tilted back roughly to the predetermined vertical position.

5.7 Separation

The face-to-face separation of the test-masses, s, was a key variable in the experiment. The total separation was determined by four components, the pendulum to screen separation z_P, the attractor to screen separation z_A, the screen thickness t_s, and the thickness of the residual glue on the test-mass surfaces t_g. The screen thickness was determined in the same way as the platinum foils, see section 4.1, and the glue thickness by surface scans, see section 4.5. The pendulum-screen (attractor-screen) separations were measured in the same way as in Cook's work[19]. COMSOL Multiphysics® models were created with a geometry of the pendulum (attractor) and screen electrodes and the separation was swept in the model to output a capacitance. We fit the models with measured data of pendulum (attractor) to screen capacitance as functions of separation.

5.7.1 COMSOL Models

The pendulum and attractor capacitance models could be separated due to the electrostatic isolation provided by the berylium-copper screen. Since the glue-filling in this iteration of

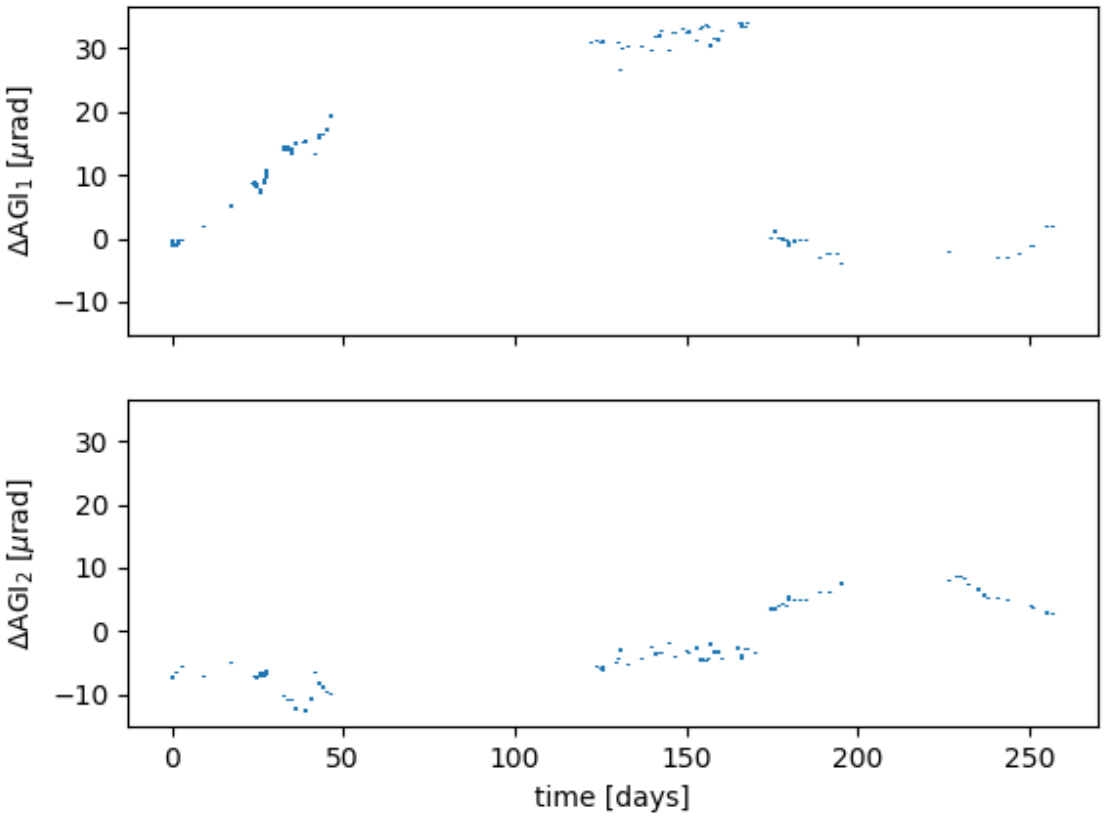

Figure 5.10: **Drift in apparatus tilt over the course of the dataset** - We monitored the AGI readings over each data run tracking the tilt of the apparatus. There was a sharp jump at 168 days in the tilt position when the ion pump failed and the apparatus was subsequently tilted back roughly to the predetermined vertical position.

the experiment uniformly filled the wedge patterns, the models were much simpler than those used by Cook.

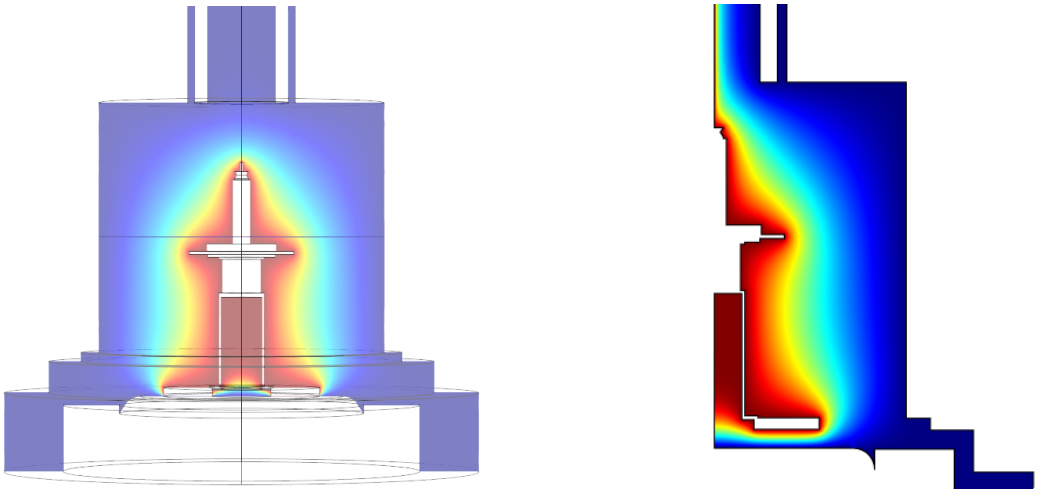

Figure 5.11: **Pendulum COMSOL models** - The pendulum was set to a 1V potential and the screen and housing structure were set to ground in both 3D (left) and 2D-axisymmetric(right) models. The color indicates the electric potential in the surrounding vacuum.

Pendulum Model

Two models were created for the pendulum, a fully 3D model and a 2D axisymmetric model symmetric about the fiber axis, figure 5.11. The fully 3D model allowed us to estimate the contributions from the non-axisymmetric components that contributed at larger separations, such as the mirror cube, calibration spheres, and cutouts in the pendulum post. The 2D model could be computed much faster and with a higher mesh density such that the predictions converged to within 0.1%.

Geometric features not included in the model were the slight height mismatch in the epoxy filling of the wedge-patterns, the hole in the mu-metal shield for the angle read-out access, and the fixed mirrors for the angle read-out.

Attractor Model

The attractor model was created as a 2D axisymmetric model symmetric about the turntable axis and included the entire turntable bearing housing out to the electrostatic screen support structure, figure 5.12. Non-axisymmetric components that were not included were: the 3-fold screen alignment actuators, the 6-fold screws that held the screen to the flexure, and the 6-fold screws that adjusted the runout and tip-tilt of the attractor test mass pattern.

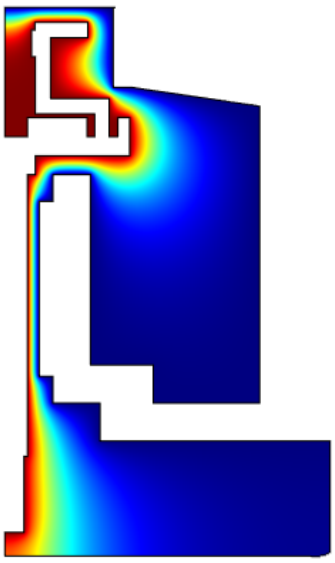

Figure 5.12: **Attractor 2D-axisymmetric COMSOL model** - The turntable was set to a 1V potential and the screen and support structure were set to ground. The color indicates the electric potential in the surrounding vacuum.

5.7.2 Z-scans

Throughout the science data collection we measured the pendulum-screen capacitance and the attractor-screen capacitance. We also recorded dial-indicator positions of the pendulum vertical translation stage and encoder positions of the screen actuators. These tools allowed

us to also perform dedicated measurements of pendulum-screen (attractor-screen) capacitance as a function of dial-indicator (actuator encoder) position, which we referred to as z-scans.

For the pendulum z-scans, we began with a separation of several millimeters to the screen and stepped logarithmically closer to the point of contact with the screen. At each step we recorded the z-stage dial-indicator position and average capacitance value and error. Similarly for attractor z-scans, we translated the screen to a couple millimeter separation to the attractor test-mass and stepped logarithmically closer to attractor, recording both the average actuator encoder position and the capacitance and error. Example z-scans for both the pendulum and attractor sides are shown in figures 5.13, 5.14, respectively.

5.7.3 Fitting

The COMSOL data was interpolated with a third-order spline to create a model for capacitance as a function of separation. This served as the basis for a model with which to fit the z-scan data. The full four-parameter ($\vec{a} = [C_0, G, z_0, \delta z]$) model is given by

$$\overline{C}(z, \vec{a}) = C_0 + GC(z - z_0) + \frac{1}{2}(\delta z)^2 C''(z - z_0), \tag{5.2}$$

where $C(s)$ is the spline-interpolated capacitance function, C_0 is an offset capacitance, G is a gain correction, z_0 sets the zero-separation point, and δz is a nonlinear correction using the second derivative of the spline model which can be interpreted as the bounce amplitude or change in separation due to tilt.

The z-scan data was fit to equation 5.2 with a nonlinear least-squares fit (Levenberg-Marquardt) minimizing the χ^2 function given below with respect to the model parameters,

$$\chi^2 = \sum_i \frac{(C_i - \overline{C}(z_i, \vec{a}))^2}{\sigma_{C_i}^2 + \left(\frac{\partial \overline{C}(z_i, \vec{a})}{\partial z}\right)^2 \sigma_{z_i}^2}. \tag{5.3}$$

Here, C_i and σ_{C_i} are the z-scan measured capacitance and error, $\overline{C}(z_i, a)$ is the model prediction at the measured micrometer position, and $\frac{\partial \overline{C}(z_i, \vec{a})}{\partial z}\sigma_{z_i}$ is the capacitance model error

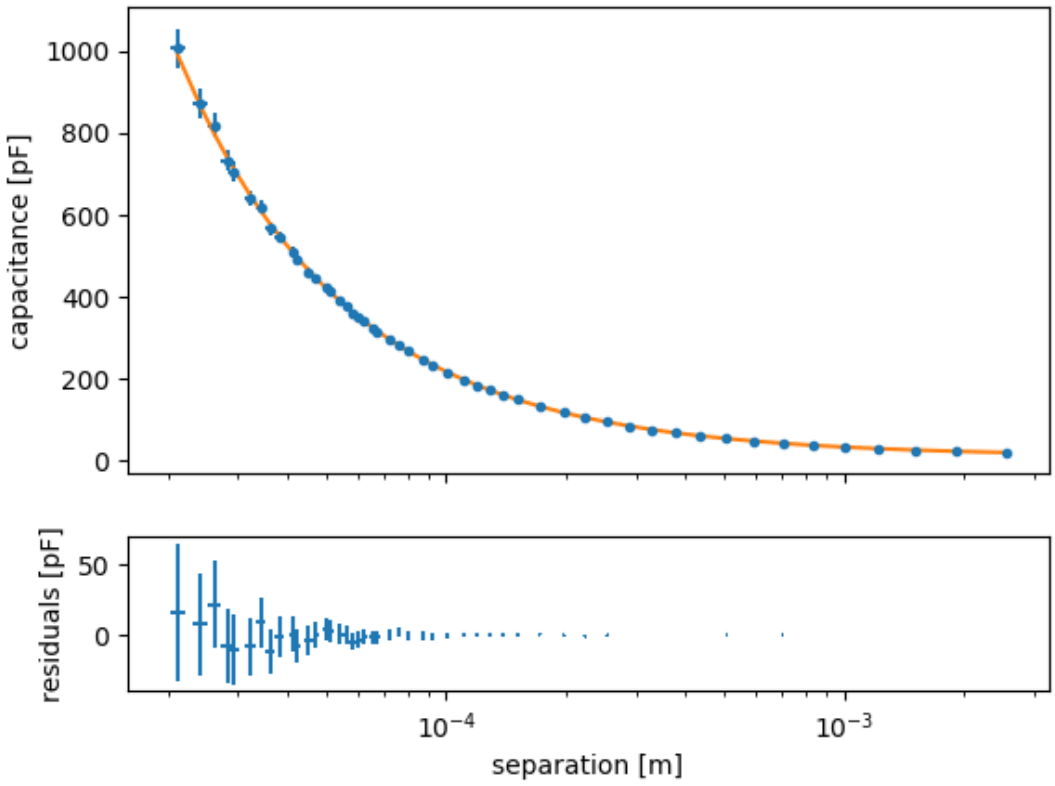

Figure 5.13: **Pendulum z-scan** - The pendulum was raised to a separation of approximately 3mm from the screen. The position at which the pendulum contacts the screen was derived from a fit of the COMSOL model to the scan data giving $z_{0,P} = -34.2 \pm 0.8\mu$m.

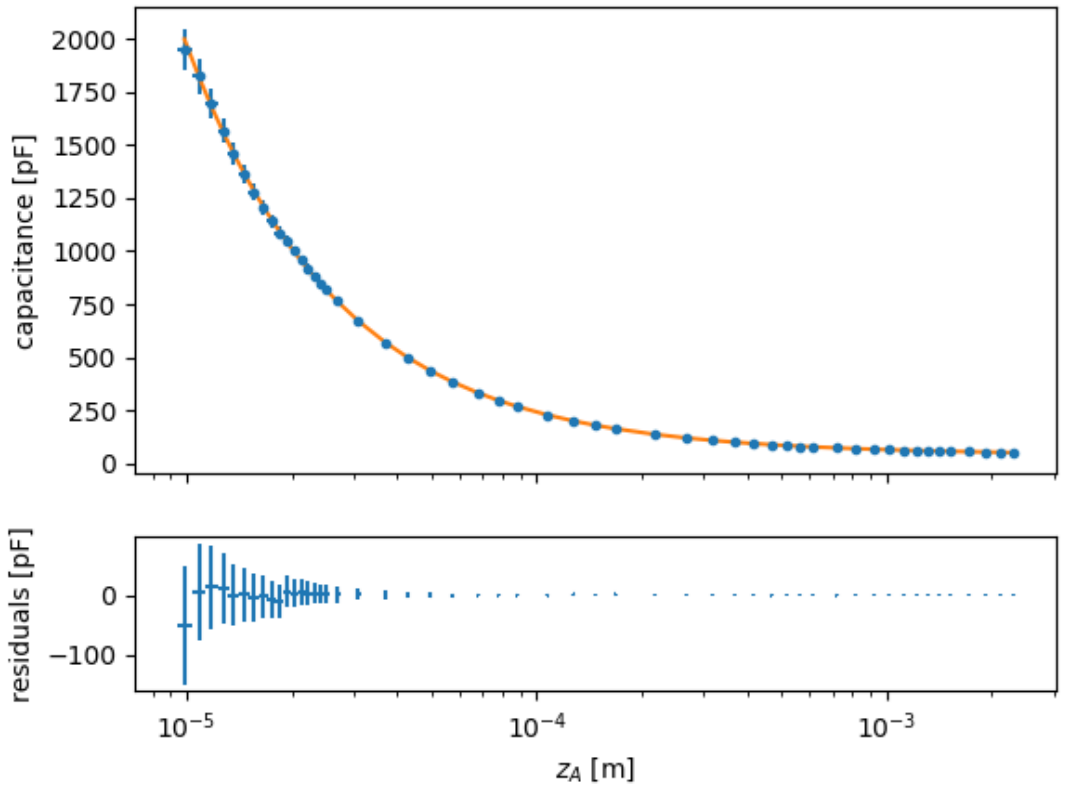

Figure 5.14: **Attractor z-scan** - The screen was raised to a separation of approximately 3mm from the attractor test-mass. The position at which the screen contacts the attractor was derived from a fit of the COMSOL model to the scan data giving $z_{0,A} = 1133.8 \pm 0.4\mu$m.

due to micrometer position uncertainty.

5.7.4 Separation Measurement

We created a mapping of capacitance to position by spline-interpolating our fit capacitance model to the pendulum(attractor) z-micrometer values. This function, $Z_{P(A)}(\overline{C})$ allowed us to map capacitance values to a pendulum(attractor) position. In order to find the true separation, we took the weighted average of the separation derived from the capacitance measurement along with dial indicator measurement, achieving μm level uncertainties.

5.7.5 Achieving Minimal Separations

We spent much of our effort achieving the smallest attractor-screen separations. With the screen aligned to the attractor test-mass, we stepped the screen closer to the attractor up to the point of contact and slightly beyond ($\approx 50\mu$m). With the screen pressed into the attractor, a high spot on the test-mass would cause visible deformations of the stretched screen. We searched with a stereo-microscope for the high points, carefully removed the screen, and searched for the offending dust particle. The dust particles or glue specks were often loosely embedded in the glue surface and could easily be wiped away with a clean room wipe or poked away with a soft wooden applicator. We ultimately achieved an attractor-screen separation of $z_A = (13.5 \pm 0.4)\mu$m face-to-face.

The pendulum-screen separation was more difficult to minimize. We performed several steps of wiping the screen, assembling the apparatus, aligning the apparatus to the pendulum test-mass, and then checking the minimum achievable separation. We searched for similar point defects on the pendulum test-mass surface, by pressing a spare stretched electrostatic-screen into the test-mass. Offending dust particles or glue specks could be wiped away or carefully removed. Ultimately, we were able to achieve separations of $z_P \lessapprox 20\mu$m before the surfaces touched, although we could not always operate the torsion balance simultaneously.

5.7.6 Stability

We took a total of 15 z-scans throughout the data-set. The z-micrometer value was reset twice between the first three z-scans. Throughout much of the science data we took a z-scan roughly every two weeks, figure 5.15. We saw the pendulum z_0 position drift by 0.74μm/week, likely from relaxation in the vertical damper.

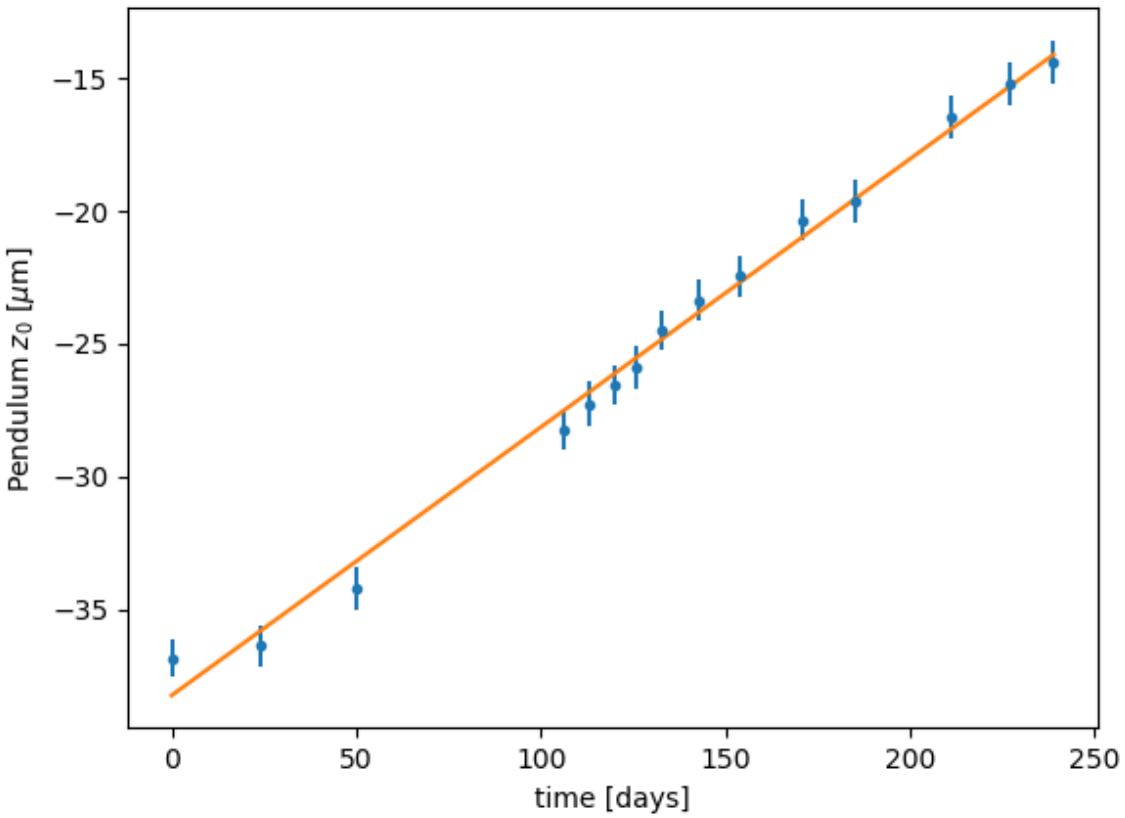

Figure 5.15: **Drift in the micrometer position of pendulum-screen contact,** $z_{0,P}$ - We performed 15 pendulum z-scans over the course of data taking, each giving a measure of $z_{0,P}$. The first two points have been shifted by known offsets accounting for a z-micrometer reset before the third point.

In order to preserve the close separation of the attractor to the screen, we only performed two attractor z-scans throughout the data-set. However, we regularly took data to check the attractor-screen separation. We found the attractor z_0 position drifted by less than 1.5μm.

5.8 Gravitational Centering

The process of centering the pendulum test-mass above the attractor test-mass rotation axis was done as a set of science data runs in the same process as detailed in Chapter 7. The pendulum was translated at a fixed vertical separation to various (x,y)-positions to search for the maxima in the 18ω and 120ω torques. The Newtonian and Yukawa torques were known to be maximized when the pendulum test-mass was aligned to the attractor rotation axis. In particular, the 120ω torque was the most sensitive signal to a radial misalignment, but could be difficult to resolve when misaligned by more than a millimeter. When the pendulum was misaligned by several millimeters, it was easier to measure the 18ω torque to roughly align the axes. The radially aligned center position was ultimately determined with a set of five runs translating around the 120ω torque maximum position along each axis.

The gravitational centering was performed once roughly at the beginning of the data taking before the initial pendulum-screen leveling. After the leveling the apparatus, the centering was performed again. The ion pump failed 168 days into the data-taking interval and the apparatus was re-attached to the turbo pump and baked again. The gravitational centering was not repeated until the end of the dataset. The center position in this third set disagreed with the initial center positions by $\approx$ 23μm in each axis. We corrected the subsequent data for the change in center position. We believed discrepancy was due to a change in tilt of the apparatus in removing the ion pump, and re-attaching it to the apparatus after the failure. A final set of gravitational centering runs were taken 40 days later to verify the center position after the ion pump failure. The final two centering datasets are plotted in figure 5.16.

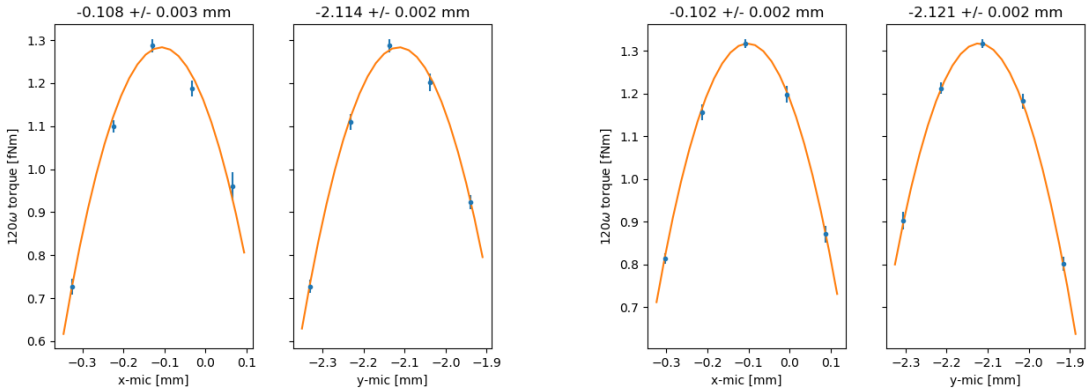

Figure 5.16: **Two sets of gravitational centering data** - The third set of centering data (left) was taken after the ion pump failure. The fourth set (right) was taken approximately 40days later. The blue points show 120ω torque measurements and the orange curves shows the best fit paraboloid to the combination of both x- and y-translations in each set.

5.9 Experimental Parameters

Here we summarize the values obtained through the complete set of alignments. We varied the pendulum-screen separation over the course of data-taking to make the measurement so only give the uncertainty on the point of contact with the screen. The screen position was adjusted at one point in the data-taking process, but the overall attractor-screen separation remained fixed throughout. The apparatus tilt and horizontal center were both changed once during data-taking; we only display the first value for each center position.

Parameter	Value ± Error	Units
$\widetilde{\Psi}_A$	58 ± 9	μrad
$\widetilde{\Psi}_S$	0 ± 18	μrad
$\widetilde{\Psi}_P$	82 ± 9	μrad
AGI_1	383 ± 23	μrad
AGI_2	-147 ± 35	μrad
r_A	7.5 ± 1.8	μm
x_0	-0.130 ± 0.004	mm
y_0	-2.138 ± 0.003	mm
$\overline{z_A}$	13.5 ± 0.4	μm
$z_{0,P}$	- ± 0.8	μm

Table 5.1: **Alignment parameter measurement summary** - Most angular alignments were determined as a deviation from perpendicular, $\widetilde{\Psi}_X = \Psi_X - \pi/2$, see figure 5.1. The point at which the pendulum and screen made contact $z_{0,P}$ drifted slightly throughout the dataset, so we only display its uncertainty. The apparatus tilt (AGI_1, AGI_2) and horizontal center (x_0, y_0) are given as measurements of the AGI and horizontal dial indicators, respectively, where the zero was arbitrary.

Chapter 6

DIRECT MEASUREMENTS OF TEST-MASS MAGNETIC PROPERTIES

A test set-up with a magnetically shielded anisotropic magnetoresistance (AMR) probe and a rotating turntable was developed for investigating stray magnetic fields for the spin-dependent force experiment [52]. After a period of disuse, we rebuilt the set-up to investigate a possible permanent magnetic contamination in the platinum foils cut with wire EDM. A new stepper motor and driver were installed, additional mu-metal shielding was added to decrease background fields, slight timing errors in the data acquisition system were corrected, and a 200× amplifier with 1s low-pass filter were added to the AMR probe output.

6.1 Measurement

The measurement apparatus consisted of a rotating turntable made of non-magnetic materials and an AlphaLab Inc. single-axis milliGaussmeter AMR probe on a three axis stage positioned above the turntable, all enclosed in a mu-metal box. Measurements consisted of rotating a test-mass on the turntable under the AMR probe. The AMR probe data were filtered to attenuate harmonics associated with the stepper motor that drives the turntable. We also made the same measurement without the test-mass to remove effects associated with the background. We binned the data in each data run by turntable angle and fit harmonics to the difference of the two measurements.

6.1.1 Filtering

There were three hardware low-pass filters in the system and an additional software filter in the analysis. The first two were first order low-pass RC filters: one in the AMR sensor itself

($\tau = .33$s) and the other on the amplifier ($\tau = 1$s). The response for each low-pass filter of order p and time constant τ can be modeled as:

$$\chi_{LP}[\omega] = \frac{1}{(1 + i\omega\tau)^p}$$

The third hardware filter came from the averaging associated to the finite size of the 1mm $\times$ .2mm sensor itself. The spatial filter is actually a fairly complicated response of the Fourier-Bessel convolution of the magnetic field within the region occupied by the sensor and so could be calculated in a similar manner to the torque of spin dipole-dipole interaction. We simply approximated this response of the finite size of the sensor as a moving average filter with angular frequency given by radial position of the sensor over the sensor width.

We also implemented a software FIR filter at the 200ω frequency to remove the effect of higher harmonics associated to the stepper motor.

6.1.2 Binning

The data were broken into cuts of turntable angle and then binned by angle into N_b bins. The binning serves as a low-pass moving-average filter (so long as the high-frequency noise is not aliased by wrapping the data by angle). The response for a rectangular filter with M points is:

$$\chi_{MA}[\omega] = \frac{\sin(\omega M/2)}{M \sin(\omega/2)}$$

where ω is angular frequency, $M = f_s T_0/N_b$ is the number of samples in a bin, f_s is the sample rate, and T_0 is the turntable period. The residuals from the binned and background subtracted data can then be fit with harmonics of the turntable and corrected for filter responses.

6.1.3 Fitting

The filtered and binned data and background runs were subtracted, and the residuals fit with sine and cosine of turntable harmonics, most importantly the 18ω and 120ω. We also compared adjacent background runs and fit the residuals of their difference for the same harmonics to estimate errors. We then corrected for the amplitude attenuation factors associated with each of the filters.

6.2 Results

We initially had four 50μm thick platinum test-masses cut with wire EDM. Two of these foils showed a significant magnetic contamination, which led us to discover that some stainless steel was used in our initial cutting procedure. The stainless steel sheets had provided structural support to the cutting stack of platinum foils. We then had a second batch of six (four 50μm-thick and two 100μm-thick) platinum test-masses cut replacing the stainless steel pieces with beryllium-copper sheets as described in Chapter 4. We again measured these test-masses in the AMR probe set-up.

The AMR probe measurements were all performed before the actual torsion balance experiment. In retrospect, we might have searched for a z-oriented magnetic signal induced from the Earth's field, see section 10.1. However, this would have required removing the magnetic shielding and the size of the probe would have prevented placing the sensor closer than 1mm. Additionally, the finite size of the sensor attenuated any potential 120ω signal by about a factor of $10\times$, therefore a majority of the measurements were done with the sensor over the 18ω portion of the pattern. The binned data and background from the platinum attractor at .5mm is shown in figure 6.1. The binned residuals of the two test-masses used in this experiment at .5mm are shown in figure 6.2. We summarize the results of the fits in table 6.1. Our platinum test-masses showed no sign of a significant magnetic contamination, but the fits were not resolved enough to completely rule out a magnetic torque even at the fNm level.

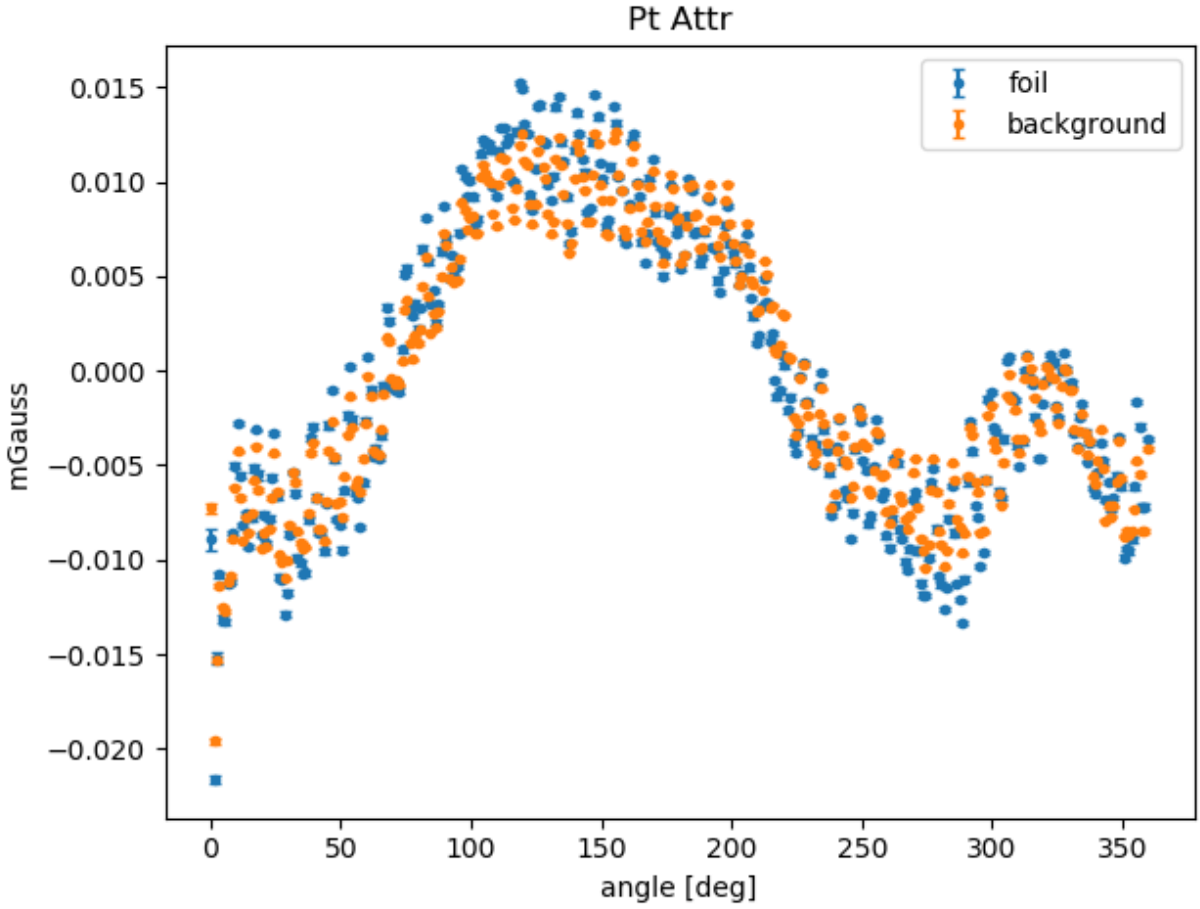

Figure 6.1: **Measurements of the $\widehat{\phi}$-oriented magnetic fields and backgrounds of the platinum attractor test-mass** - Data and background runs have been filtered and then binned by turntable angle.

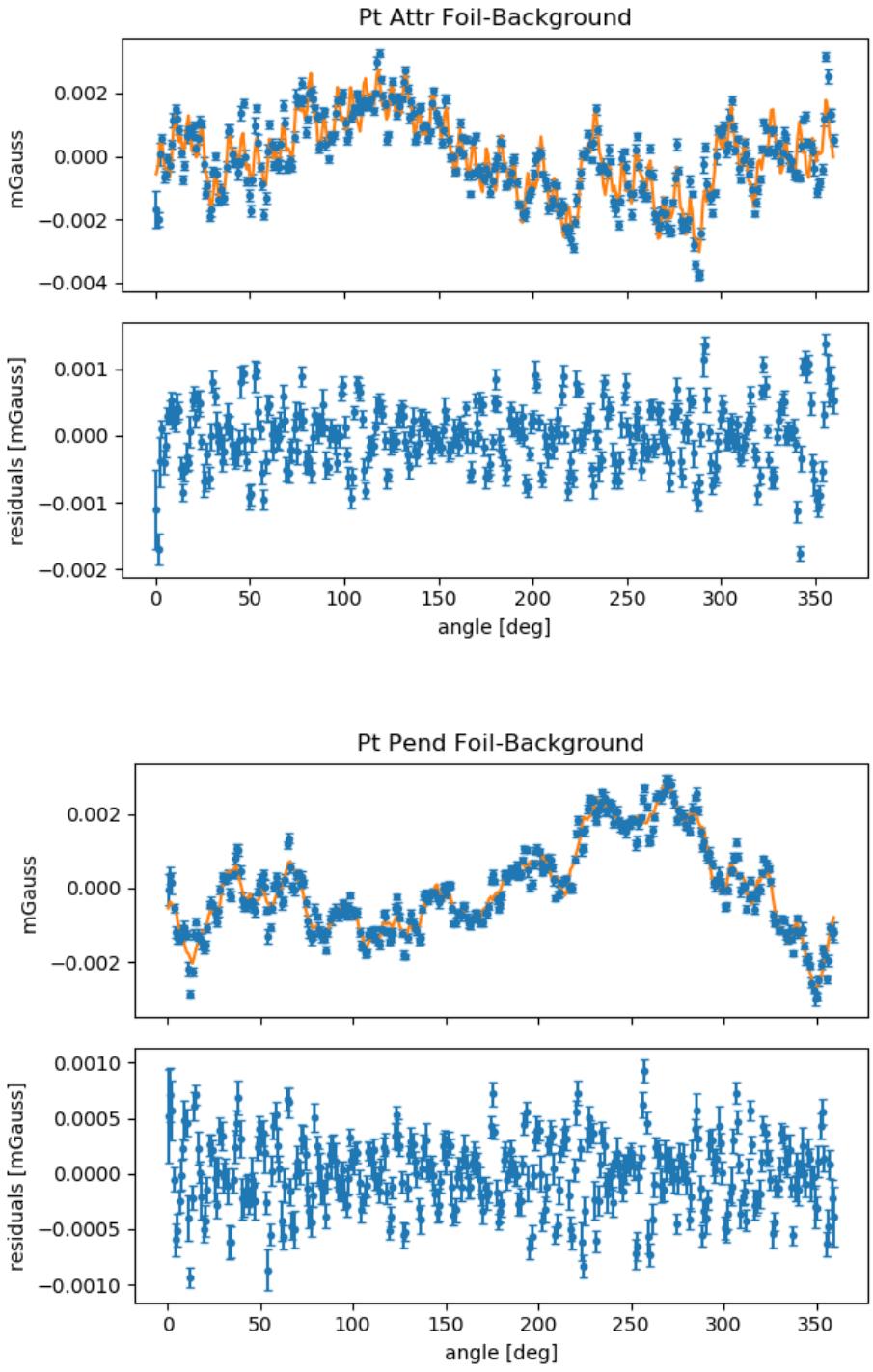

Figure 6.2: **Measurements of the $\widehat{\phi}$-oriented magnetic fields of the platinum test-masses** - Orange curves show fits to several low order harmonics, known harmonics of the turntable motor, as well as $18\omega, 54\omega$, and 120ω.

	$B_{18\omega}$	$B_{54\omega}$	$B_{120\omega}$
Pt Attr.	0.072 ± 0.346	0.181 ± 0.091	0.284 ± 0.193
Pt Pend.	0.156 ± 0.197	0.216 ± 0.257	0.443 ± 0.842

Table 6.1: Measured magnetic field in $\widehat{\phi}$-direction with AMR probe set-up at the $18\omega, 54\omega$, and 120ω components. The platinum test-masses (Pt Attr. and Pt Pend.) were both measured at a separation of .5mm. These results are consistent with no effect, $\chi^2 = 7.78$ with 6 degrees of freedom and $P = 0.26$. All values are given in μGauss.

Chapter 7

DATA TAKING PROCEDURES

After completing alignment and assembly of the apparatus (see Chapter 5), there were several steps to prepare the instrument for each run collected for science data. The process of arranging each data run and the subsequent analysis are given below.

7.1 Data Collection Procedure

The normal science data collection for the experiment took place in several repeated steps. The procedure was as follows:

1. Move pendulum to desired (x, y, z) coordinate.
2. Center pendulum on detector, and excite amplitude to cover expected extent of the detector to be covered in the data run.
3. Perform "sweep" run. Sweep runs typically lasted for $5T_0$, where $T_0 \approx 341$s was the free torsional period of the pendulum.
4. Start attractor turning and minimize free torsion amplitude. The attractor period was typically set to $36T_0$ to place the 18ω and 120ω signals in a frequency region of high torque sensitivity.
5. Take data run. Most data runs were about a day in length. However, runs at the closest separations were often cut short by a large excitation in twist angle from seismic disturbances. An example plot of twist angle in a single run is shown in figure 7.4.
6. Stop attractor turning and set pendulum free torsion amplitude to cover the extent of the detector covered in the previous data run.
7. Perform sweep run.
8. Approximately weekly, perform pendulum capacitance versus separation scans and

calibration runs.

7.2 Non-Linearity of the Twist Angle Scale

The raw outputs of the autocollimator were read out as a difference and sum (Δ, Σ) of the two currents from either side of a position sensitive detector (PSD). This was nominally converted to angle using the known lever arm of the autocollimator and the number of bounces off of the pendulum mirror, a purely geometrical calibration. In this case, the gain from the optical lever arm was 100 (3mm long PSD and a 30cm focal length lens) and there were two bounces off of the pendulum which give a factor of 4 in angle. As the beamspot, reflected from the pendulum mirror, crossed from one side of the PSD to the other, the Δ signal ranged between $\approx [-\Sigma, +\Sigma]$. So to first order the angle was linear in diff over sum, $\widetilde{\theta} = \frac{1}{100\times4\times2}\frac{\Delta}{\Sigma}$, where the extra factor of 2 occurs because Δ/Σ changes by two units as the laser beam sweeps from one end of the detector to the other.

Our measurements consisted of torques at four harmonics of the attractor rotation frequency, but non-linearity of the angle readout could lead to false power at higher harmonics. We corrected for the non-linearities in the detector due to small non-linearities in the PSD, and a mis-match in gains on the two sides of the preamplifiers for the PSD. This correction procedure consisted of performing "sweep" runs where we mapped out the non-linearities in the detector and measured the free oscillation period using the linearity of the pendulum torsional oscillator. We always performed sweep runs with the attractor turntable stopped. We excited the pendulum amplitude using the pendulum suspension rotational stage so that the twist angle covered the detector width of corresponding data runs. The amplitude had to be large enough that the autocollimator signal was dominated by the harmonic motion of the pendulum and not by noise and slow drifts. Here we reiterate the explanation given by Kapner [36].

To account for gain mismatching we measured the sum signal's dependence on the difference signal and subtracted a linear fit, $\Sigma' = \Sigma - g\Delta$, see figure 7.1. The difference Δ and corrected sum Σ' signals were converted to angle as a low order polynomial in Δ/Σ.

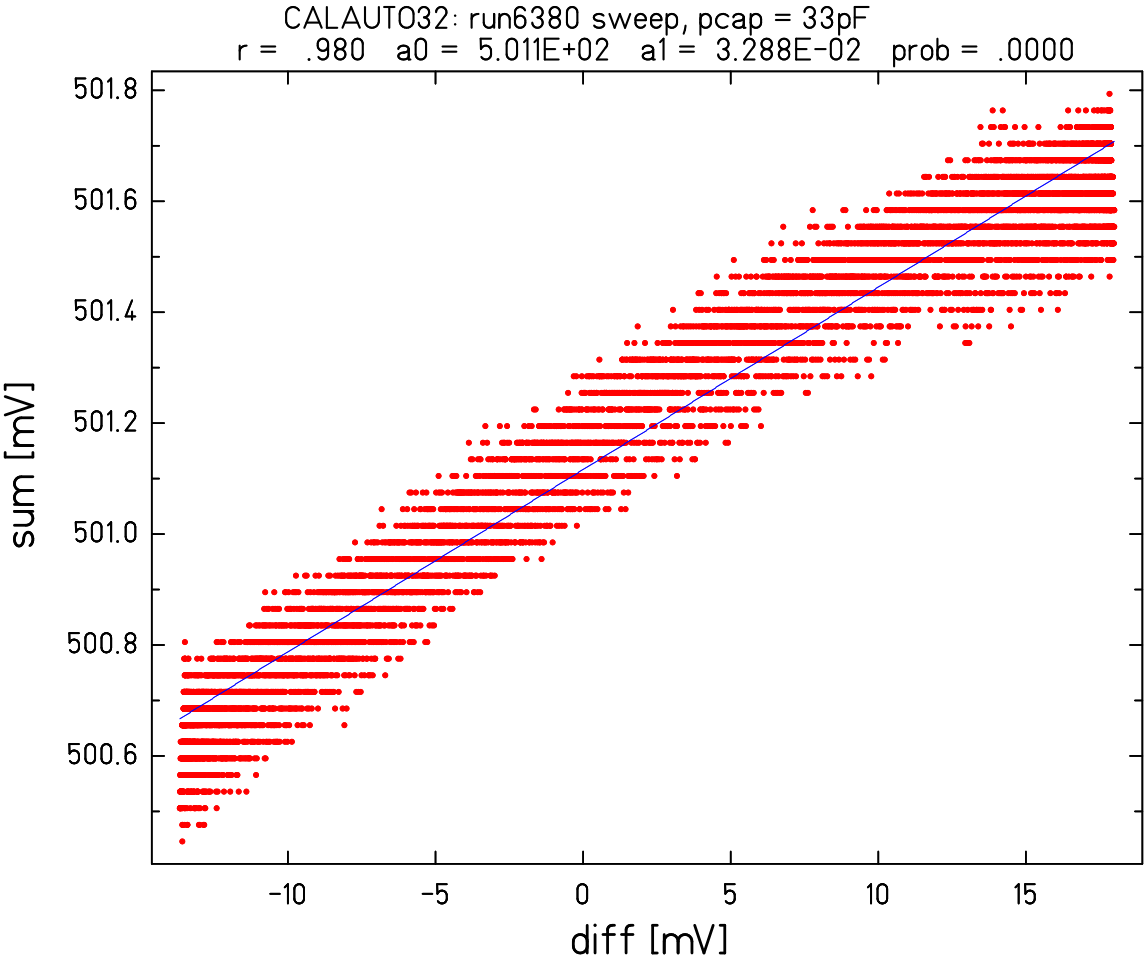

Figure 7.1: **Autocollimator gain correction** - We measured the dependence of Σ on Δ in sweep runs and corrected for gain mismatch in the pre-amplifiers.

$$\widetilde{\theta} = c_1 \left(\frac{\Delta}{\Sigma'}\right) + c_2 \left(\frac{\Delta}{\Sigma'}\right)^2 + c_3 \left(\frac{\Delta}{\Sigma'}\right)^3 + c_4 \left(\frac{\Delta}{\Sigma'}\right)^4 \tag{7.1}$$

To account for other detector non-linearities, we observed the pendulum oscillation over several periods and fit the observed twist angle to a pure damped oscillator with low order polynomial drift (see figure 7.2) given as:

$$\widetilde{\theta}_0 = D(t) + A\sin(\omega_0 t)e^{-t/\tau} \tag{7.2}$$

Here A is the amplitude of the twist signal, ω_0 is the free torsional frequency of the pendulum, τ is the decay time, and $D(t)$ is a drift term.

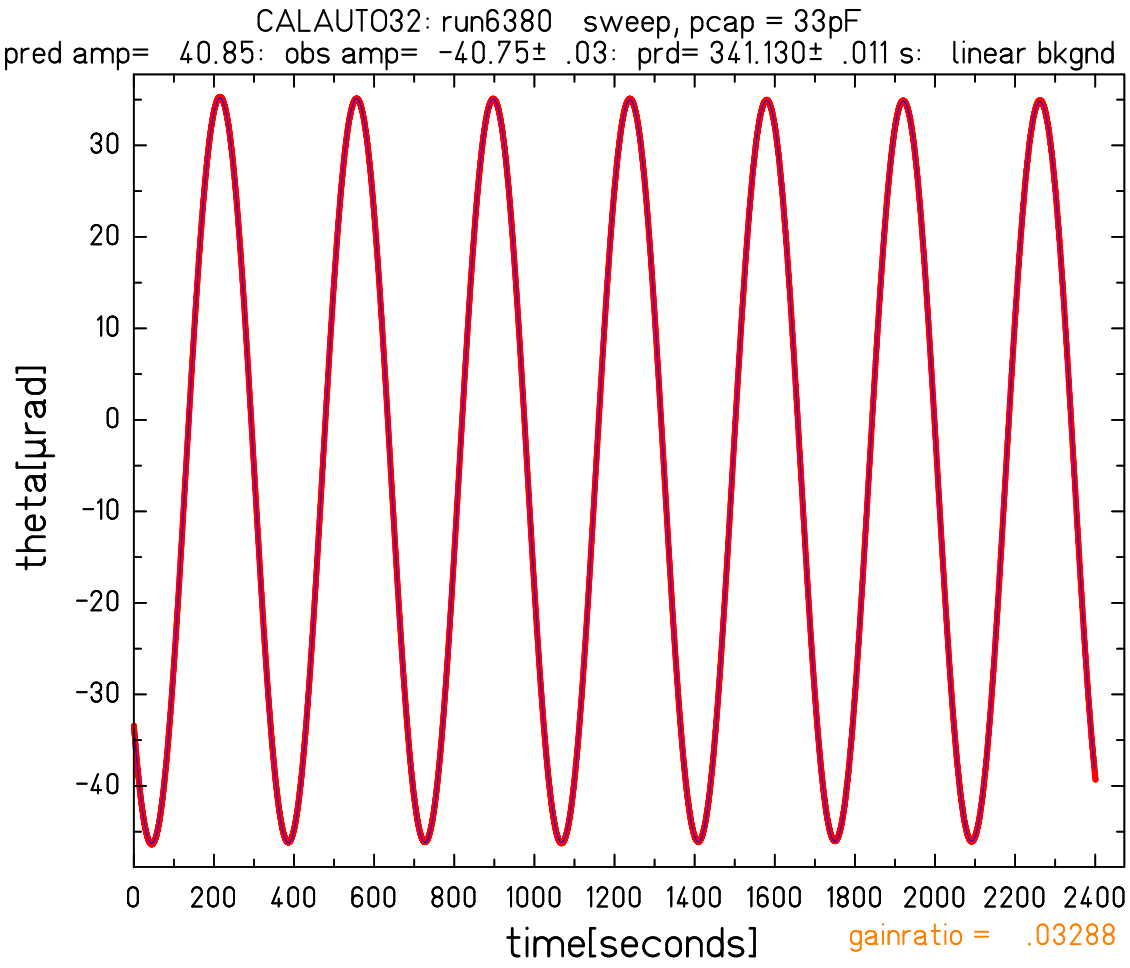

Figure 7.2: **Decaying sinusoid fit to large amplitude pendulum twist** - We performed sweep runs where the pendulum twist-angle covered a large portion of the detector. We fit the twist-angle to a decaying sinusoid.

With our fit coefficients for the damped sinusoid, we then observed the residual depen-

dence on the angle. The residuals were fit with a low order polynomial of the fit angle $\widetilde{\theta}$, see figure 7.3. Plugging equation 7.1 into the fit and collecting into powers of Δ/Σ' yielded new values for the coefficients of c_i in terms of the original c_i and the residual fit coefficients a_i.

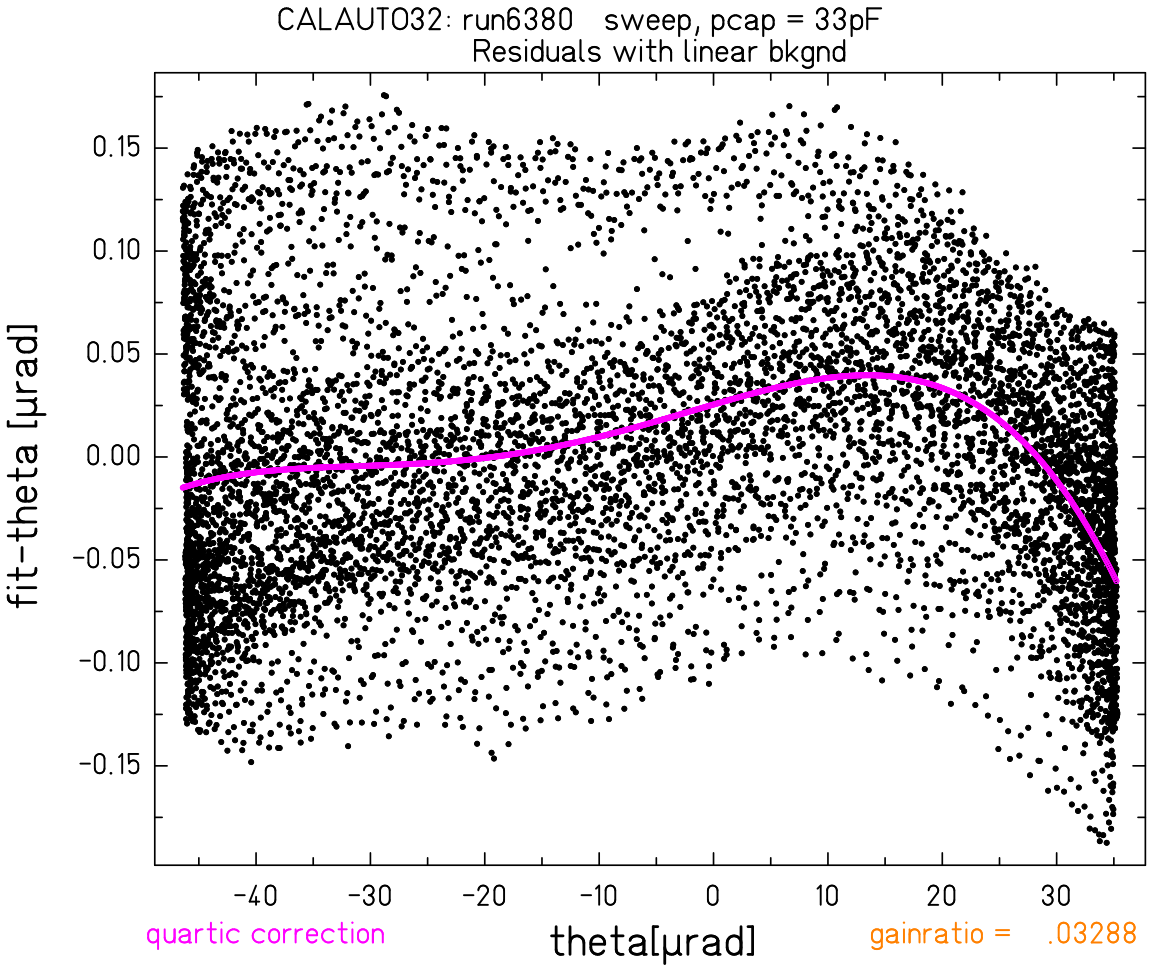

Figure 7.3: **Residuals of twist angle fit relative to fit angle** - The fit residuals relative to twist-angle map out non-linearities in the detector. We fit these residuals to a low order polynomial (e.g. a quartic).

$$\begin{aligned}
\widetilde{\theta}_0 - \widetilde{\theta} &= a_0 + a_1\widetilde{\theta} + a_2\widetilde{\theta}^2 + a_3\widetilde{\theta}^3 + a_4\widetilde{\theta}^4 \\
\widetilde{\theta}_0 &= a_0 + (a_1+1)\widetilde{\theta} + a_2\widetilde{\theta}^2 + a_3\widetilde{\theta}^3 + a_4\widetilde{\theta}^4 \\
\widetilde{\theta}_0 &= c'_0 + c'_1\left(\frac{\Delta}{\Sigma'}\right) + c'_2\left(\frac{\Delta}{\Sigma'}\right)^2 + c'_3\left(\frac{\Delta}{\Sigma'}\right)^3 + c'_4\left(\frac{\Delta}{\Sigma'}\right)^4
\end{aligned} \tag{7.3}$$

The sweep runs also provided a measurement of the decay time and of the pendulum free oscillation period, T_0, since electrostatic interactions with the screen introduced an addtional torsional spring constant.

7.3 Fitting

7.3.1 Filtering

The dominant signal in the measured twist angle, see figure 7.4, was due to the pendulum free oscillation. The free oscillation was deliberately damped down before the start of each run, but the high Q of the pendulum fiber thermally drives large amplitude changes at the resonant frequency. We followed cook's practice of applying a 4-pt digital filter that suppressed the free torsional oscillation as well as linear drifts (see figure 7.3 of Cook's thesis [19]). The definition of the 4-pt filter was

$$\widetilde{\theta}(t) = \theta(t + \frac{T_0}{8}) - \theta(t - \frac{T_0}{8}) + \theta(t - \frac{3T_0}{8}) - \theta(t + \frac{3T_0}{8}) \tag{7.4}$$

We linearly interpolated between the nearest samples in the case that an eighth of a period was not an integer number of samples. An example of the filtered twist angle data is plotted in figure 7.5.

7.3.2 Cut Analysis

Each data run was divided into "cuts" of one sixth of an attractor rotation which was chosen to match the repetition of the wedge patterns every 60°. For each cut, the filtered twist angle $\widetilde{\theta}$ was fit as a function of attractor angle ϕ with

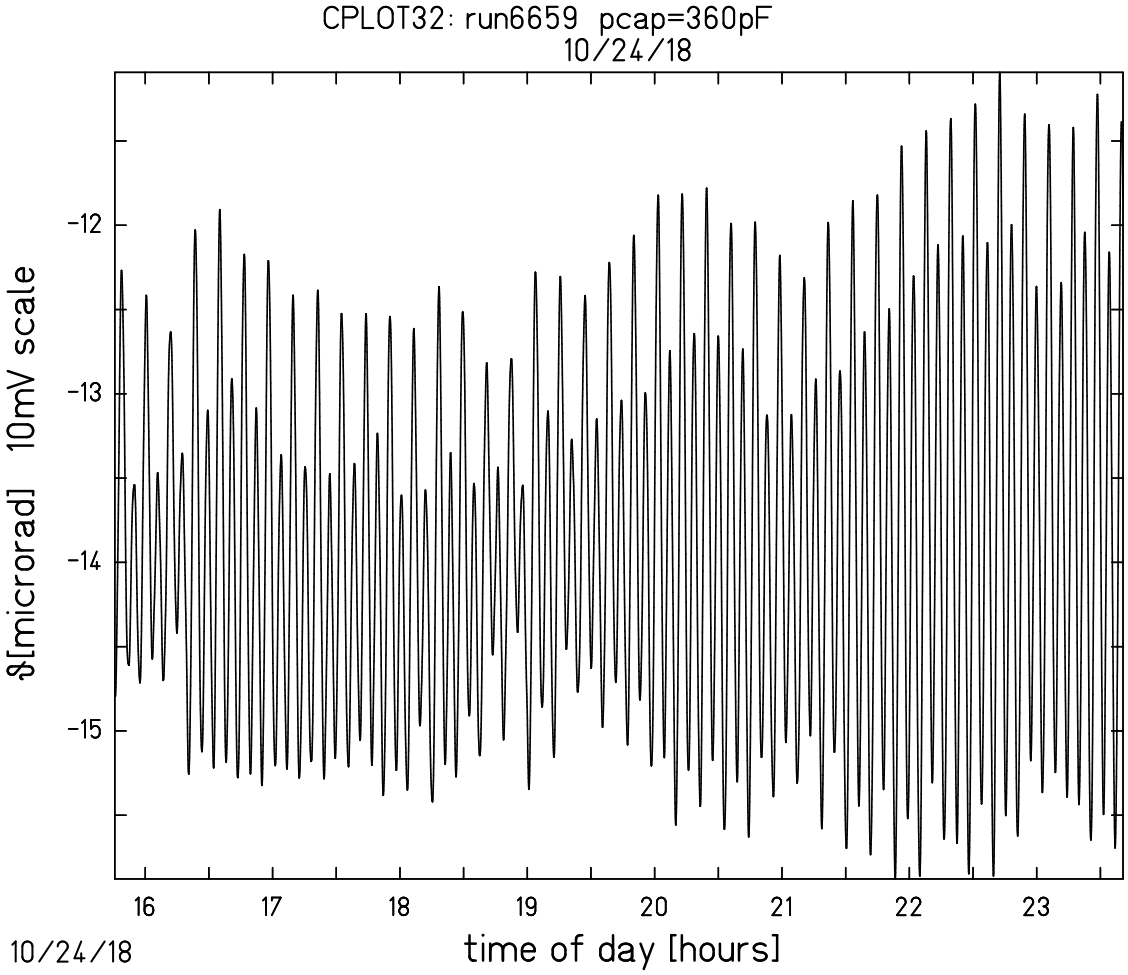

Figure 7.4: **Raw twist signal example** - This science data run, run6659, was taken at 81μm. The attractor turntable rotation period was 12420s $\approx$ 3.5hours. Approximately half of the day-long data run is plotted.

$$\theta(\phi) = \sum_n \left(C_n \cos(n\phi) + S_n \sin(n\phi)\right) + \sum_{m=0}^{2} D_m P_m.$$

This is just a linear least-squares fit to sum of harmonic coefficients at the signal frequencies (n=18, 54, 90, 120) and quadratic polynomial drift terms to account for slow changes in the equilibrium angle given in terms of Legendre polynomials P_m. An example fit to a single

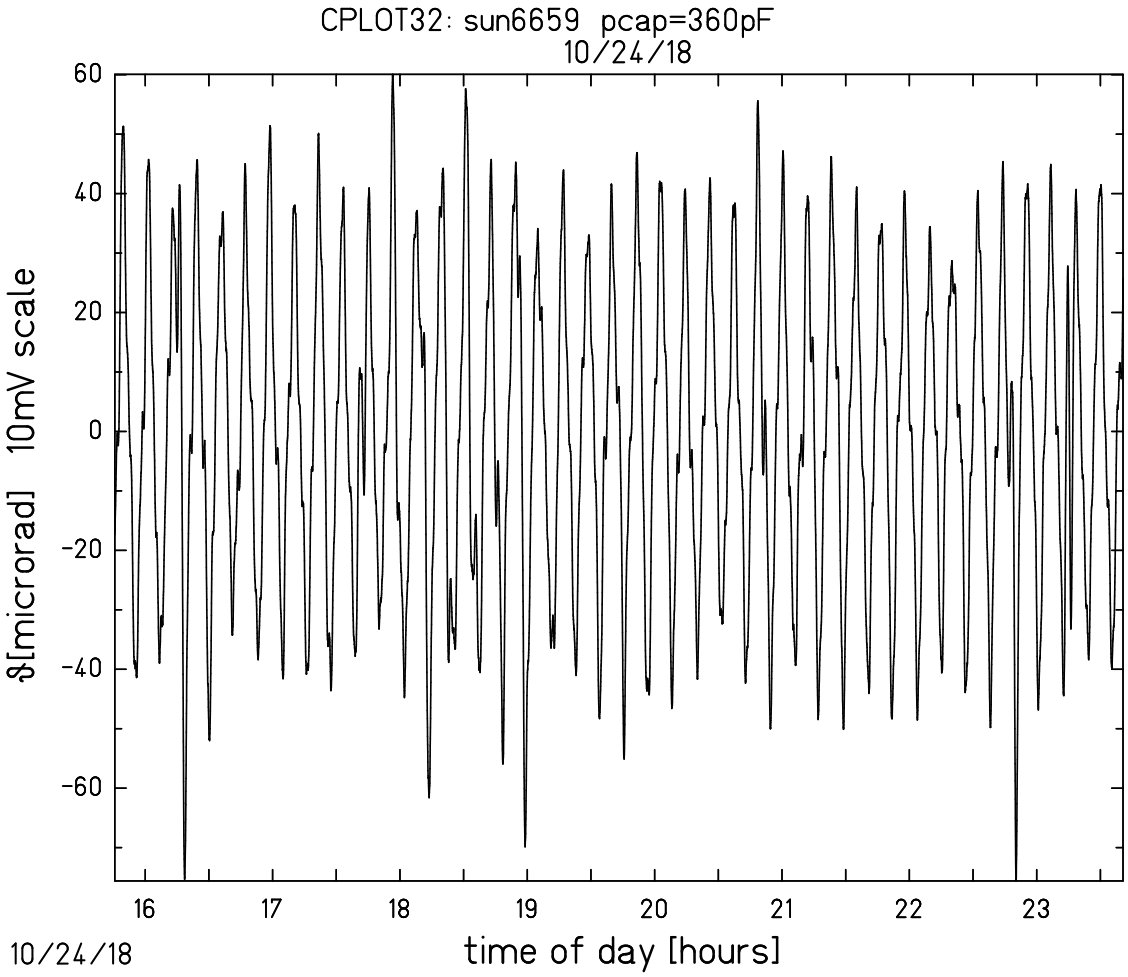

Figure 7.5: **Twist signal filtered with** $4-$**pt filter** - The 4-pt filtered twist angle removes the free torsional oscillation which constitutes the largest amplitude signal in the twist angle data.

cut is shown in figure 7.6.

7.3.3 Cut Rejection

A χ^2-statistic was generated for each cut j of the total N_j cuts defined as

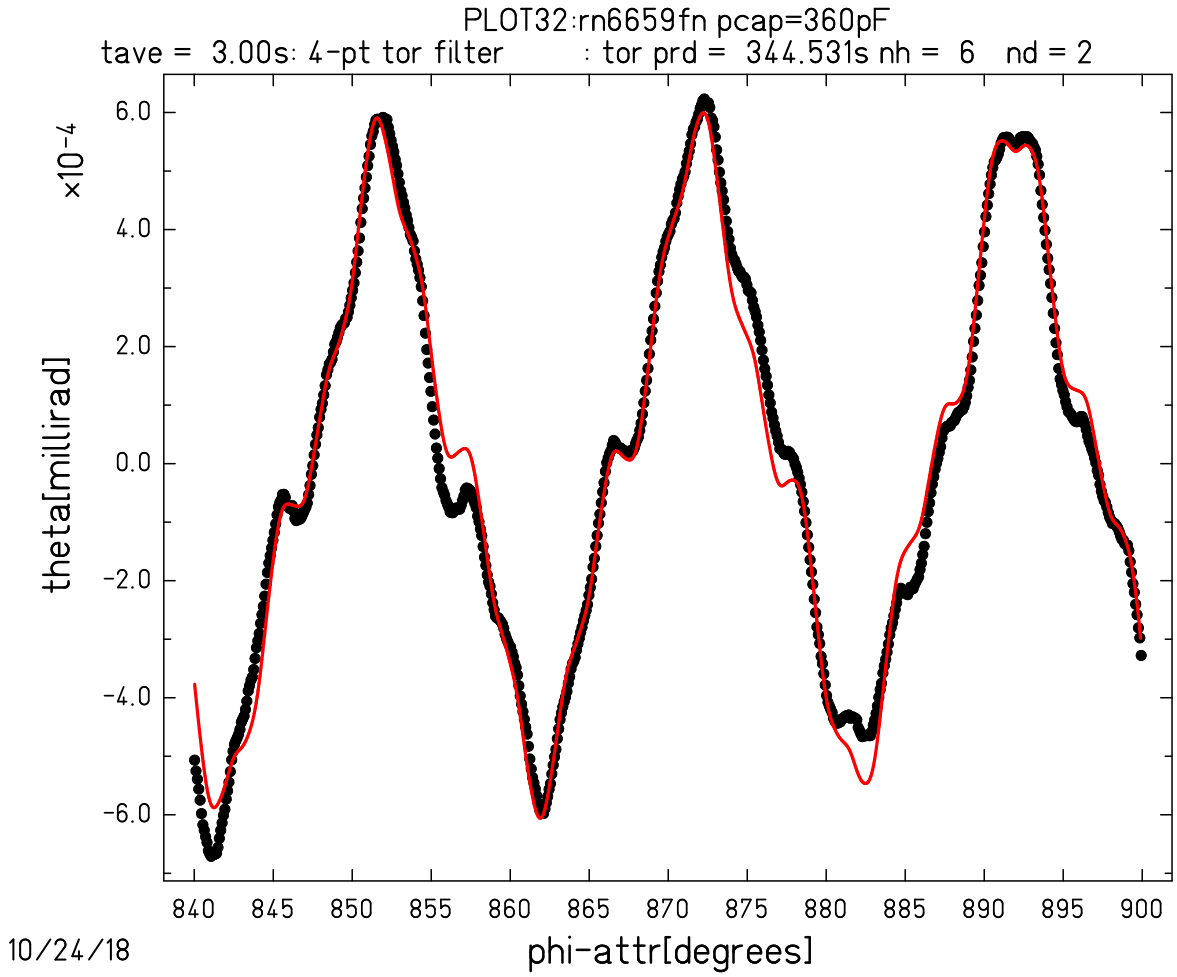

Figure 7.6: **Single data cut of filtered twist signal** - A single 60° cut from run6659 with the fit to 18, 54, 90, and 120ω harmonics of the attractor rotation.

$$\chi_j^2 = \sum_{i=1}^{N_j} (\widetilde{\theta}_i - \theta(\phi_i))^2.$$

The expected torque signals were approximately stationary and so we discarded any cuts with anomalously large χ^2 value which were indicative of a transient disturbance. A total of 205 cuts were rejected in this manner out of the 5174 cuts in all 95 data runs.

7.3.4 Combining Data

All cuts in a single data run that passed the χ^2 condition were averaged with equal weighting to give the mean harmonic cosine(sine) amplitudes. The standard deviation of the mean was determined by the scatter in the cuts.

$$\begin{aligned} \overline{C_n} &= \frac{1}{N_c}\sum_{j=0}^{N_c} C_{n,j}, \qquad \overline{S_n} = \frac{1}{N_c}\sum_{j=0}^{N_c} S_{n,j} \\ \sigma_{\overline{C_n}} &= \sqrt{\frac{1}{N_c}\frac{1}{N_c-1}\sum_{j=0}^{N_c}(C_{n,j}-\overline{C_n})^2}, \quad \sigma_{\overline{S_n}} = \sqrt{\frac{1}{N_c}\frac{1}{N_c-1}\sum_{j=0}^{N_c}(S_{n,j}-\overline{S_n})^2} \end{aligned} \tag{7.5}$$

7.3.5 Filter Corrections

The fit amplitudes of filtered twist angle were corrected for the frequency dependent amplitude and phase responses of the 4-pt notch filter, hardware low-pass filters, software averaging, and inertial response of the torsion balance. Here, an imaginary component represents a rotation in phase of the measured signal, such that a purely imaginary response would be a rotation of a sine amplitude into a cosine.

4-pt Filter

The 4-pt notch filter response can be determined for an arbitrary sinusoid input, $\theta(t) = \theta(\omega)e^{i\omega t}$ as follows:

$$\begin{aligned} \theta_{4pt}(\omega)e^{i\omega t} &= \theta(\omega)e^{i\omega t}\left(e^{i\omega\frac{T_0}{8}} - e^{-i\omega\frac{T_0}{8}} - e^{i\omega\frac{3T_0}{8}} + e^{-i\omega\frac{3T_0}{8}}\right) \\ &= 2i\left(\sin\left(\frac{\omega T_0}{8}\right) - \sin\left(\frac{3\omega T_0}{8}\right)\right)\theta(\omega)e^{i\omega t} \\ &= 2i\left(\sin\left(\frac{\pi\omega}{4\omega_0}\right) - \sin\left(\frac{3\pi\omega}{4\omega_0}\right)\right)\theta(\omega)e^{i\omega t} \\ &= \chi_{4pt}(\omega)\theta(\omega)e^{i\omega t} \end{aligned} \tag{7.6}$$

analog low-pass filter

The lock-in amplifiers used to measure the autocollimator Σ and Δ signals had a 2-pole low-pass filter with a 3s time constant, τ_{lp}. The response of the filter on the twist angle θ was mostly due to the filter on Δ because the Σ signal was effectively constant

$$\begin{aligned}\theta_{\mathrm{lp}}(\omega) &= \frac{1}{(1+i\omega\tau_{lp})^2}\theta(\omega) \\ &= \chi_{lp}(\omega)\theta(\omega)\end{aligned}$$

moving average filter

The data acquisition system averaged several samples (typically N=60) to produce a single data record. In this way the ADC sample rate ω_s of 20Hz was reduced to a recording rate of about 0.3Hz. The response for this symmetric box average was

$$\begin{aligned}\theta_{avg}(\omega) &= \frac{1}{N}\csc\left(\frac{\pi\omega}{\omega_s}\right)\sin\left(\frac{\pi\omega N}{\omega_s}\right)\theta(\omega) \\ &= \chi_{avg}(\omega)\theta(\omega)\end{aligned}$$

pendulum response

The equation of motion for the torsion balance was that of a simple spring with internal loss

$$I\ddot{\theta}(t) + \kappa\left(1+\frac{i}{Q}\right)\theta(t) = N(t)$$

where I is the moment of inertia of the pendulum, κ is the torsional spring constant of the fiber, and Q is the quality factor of the fiber. The frequency response was then:

$$N(\omega) = I\omega_0^2\left(1-\left(\frac{\omega}{\omega_0}\right)^2+\frac{i}{Q}\right)\theta(\omega)$$

where $\omega_0 = \sqrt{\frac{\kappa}{I}}$.

Final correction

Including all of the attenuation and phase corrections, the torque was

$$N(\omega) = I\omega_0^2 \left(1 - \left(\frac{\omega}{\omega_0}\right)^2 + \frac{i}{Q}\right) \chi_{lp}^{-1} \chi_{avg}^{-1} \chi_{4pt}^{-1}(\omega) \theta_{4pt}(\omega) \tag{7.7}$$

7.4 Turntable Rotation Period

The choice of turntable rotation period, T_A was determined by several constraints. Because the 18- and 120-fold patterns repeat every 60°, we choose to analyze the data in cuts of one sixth of a turntable rotation. This ensured that there were an integer number of signal oscillations in a single cut so that the different signal frequencies were orthogonal. It also required us to drop less data when a cut was excluded in the case of an external disturbance. We set the turntable rotation period to be an integer multiple of 6 times the pendulum free torsional period, $T_A = 6mT_0$ so that each cut also contained an integer number of free torsional oscillations.

The minimum in the observed torque power spectral density occurred a bit above the pendulum resonant frequency. We wanted to place the 120ω signal in the lowest noise region, which required $m \leq 20$.

We required that neither the free resonance nor its first two harmonics occur at one of the signal frequencies, $m \notin [1, 3, 5, 9, 10, 15, 20]$. This ensured that any non-linearities did not mix power in the free torsion amplitude into the signal frequencies.

The 4-pt filter also had additional zeros at many even harmonics of the pendulum free torsional frequency. We required that the 18ω, 54ω, 90ω, and 120ω not occur at a filter zero, $m \notin [1, 4, 5]$. This restricted the turntable frequency to $m \in [2, 6, 7, 8, 11, 12, 13, 14]$. The majority of the runs were taken with $m = 6$ and $T_A = 36T_0$ in order to place the 120ω at the torque minimum. For runs at separations greater than 1mm, the 120ω signal to noise ratio was small and so $T_A = 12T_0$ placed the 18ω near the torque minimum instead. Additionally at separations less than 70μm, the low frequency torque noise increased and the pendulum

resonant frequency decreased, so that $T_A = 12T_0$ allowed us to resolve both the 18ω and 120ω simultaneously, figure 7.7. This choice required sacrificing some torque sensitivity in the 120ω at the shortest separations.

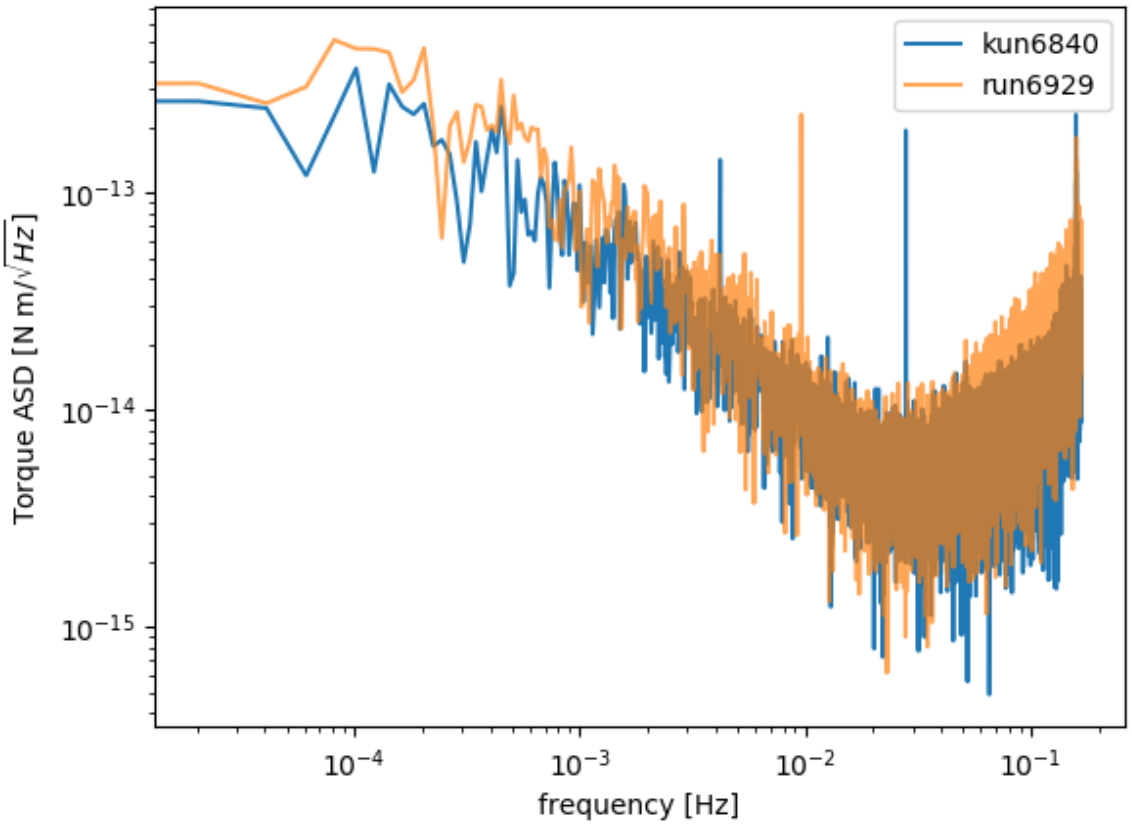

Figure 7.7: **Comparison of turntable rotation rates** - The torque noise of run6840(blue) and run6929(transparent orange) at similar separations $z_p \approx 28\mu$m were comparable, but the turntable rotation rate was faster in run6840. The 18ω signal in run6929 (1.4 mHz) was below the ambient noise, but at the faster turntable rate of run6840 the 18ω torque (4.2 mHz) was well resolved. The 120ω torque was resolved equally well.

7.5 Missing Reads

Occasionally the data acquisition would skip a reading that could be seen by a jump in turntable angle of twice the average turntable angle step. These jumps in angle lead to a slight discrepancy in the assumed turntable rotation speed which was determined by the time of arrival of the encoder index mark. A total of seven runs were fixed by linearly interpolating the data between samples around the missed reading, denoted by kunXXXX in Appendix A. The fix had negligible impact on the harmonic fits against turntable angle, but made power spectrum estimates cleaner.

Chapter 8

CALIBRATION

There were two factors that determined the conversion of the autocollimator angle readout into torques. First, the autocollimator output was converted to twist angle, and second, the angles were converted to torques. We separately verified the torque scale by injecting a known gravitational torque as a direct calibration.

8.1 Angle Calibration

As discussed in Chapter 7, we performed sweep runs to correct for non-linearity in the autocollimator. The twist signal was a low order polynomial of the ratio of Δ and Σ signals of the autocollimator where the linear coefficient was given approximately by the geometric factors of the optical components (3mm long PSD and a 30cm focal length lens),

$$\widetilde{\theta} = c_1 \left(\frac{\Delta}{\Sigma'}\right) + c_2 \left(\frac{\Delta}{\Sigma'}\right)^2 + c_3 \left(\frac{\Delta}{\Sigma'}\right)^3 + c_4 \left(\frac{\Delta}{\Sigma'}\right)^4 \tag{8.1}$$

.

The sweep runs also provided a measurement of the pendulum free oscillation frequency (ω_0) and the the decay time ($\tau = \frac{2Q}{\omega_0}$, where Q is the quality factor), both of which were used to convert twist angle measurements to torque. However, the sweep runs did not provide any verification of the geometrical angle calibration, so we still treated the the true angle as only proportional to the non-linearity-corrected geometrical angle.

$$\theta = C\widetilde{\theta} \tag{8.2}$$

8.2 Angle to Torque Conversion

For a simple spring, one might naively use the torsional spring constant to convert angles to torques. However, the torsional spring constant was sensitive to various changes in the experiment and additional electrostatic or other restoring torques may arise dependent on the environment (for instance the proximity of the pendulum to the electrostatic screen). Instead of the torsional spring constant, we used our knowledge of the mass and dimensions of the pendulum to construct an accurate model of the moment of inertia of the pendulum along with a measurement of ω_0 taken both before and after the data run in our "sweep" runs. Since the moment of inertia of the pendulum was static, the measurement of ω_0 captured any changes to the torsional spring constant. We also accounted for the frequency dependence of the response due to losses in the fiber or through viscous damping. Our uncertainty in the autocollimator calibration and the moment of inertia related our final torque measurements N_{meas} to the true torques N_{true} such that single scale factor, γ, related our predicted torques to the measured torques as follows

$$\begin{aligned} N(\omega) &= \left[-I\omega^2 + i\omega\frac{I\omega_0}{Q_V} + \kappa(1+\frac{i}{Q_A})\right]\theta(\omega) \\ &= I\omega_0^2\left[1-\left(\frac{\omega}{\omega_0}\right)^2 + i\left(\frac{\omega}{\omega_0 Q_V}+\frac{1}{Q_A}\right)\right]\theta(\omega) \\ &= CI\omega_0^2\left[1-\left(\frac{\omega}{\omega_0}\right)^2 + i\left(\frac{\omega}{\omega_0 Q_V}+\frac{1}{Q_A}\right)\right]\widetilde{\theta}(\omega) \\ &= \frac{1}{\gamma}\widetilde{I}\omega_0^2\left[1-\left(\frac{\omega}{\omega_0}\right)^2 + i\left(\frac{\omega}{\omega_0 Q_V}+\frac{1}{Q_A}\right)\right]\widetilde{\theta}(\omega) \\ &= \frac{1}{\gamma}N_{meas}(\omega) \end{aligned} \tag{8.3}$$

The product of moment of inertia, torsional frequency squared, and angular scale set the overall scale for the conversion of angles to torques. And although the frequency could be measured well below 0.1% relative error, the moment of inertia was assumed to only be modeled to 1%, and the geometric calibration and stability of the autocollimator calibration

was likely about 1%. This motivated our use of an external calibration source via an induced gravitational torque signal with known amplitude.

8.2.1 Moment of Inertia

We made a detailed model of the geometry and mass distribution of our pendulum which were used to determine the moment of inertia and the low order gravitational multipole moments. The model was built in `MULTIN` which calculated the moment of inertia, the gravitational multipole moments, and also the masses of the individual sub-components [23]. We verified the calculation by weighing the sub-components, which agreed to $\sim 1\%$. We then adjusted the component density to correct for the mass discrepancy. The test-mass and glass disk were replaced in 2018 on the same pendulum body and fiber. This gave two consistent estimates of the fiber torsional spring constant from the computed moments of inertia and measured torsional periods. Additionally, we took a set of runs, see section 8.3, without the three pendulum calibration spheres. This gave a third measurement of the spring constant via moment of inertia calculation and period measurement.

8.3 Calibration TurnTable

Instead of attempting to account for both of the errors in the geometrical calibration and the moment of inertia estimate, we calibrated the overall torque scale by injecting a known gravitational octapole torque. The calibration 3ω torque had a known amplitude, was placed at the same frequency as the science data 120ω torque, and was unaffected by any new short range physics. The torque was gravitationally sourced by three brass spheres placed on a turntable external to the vacuum chamber which acted on the three spheres placed near the top of the pendulum fig 8.1. These both had large (3,3) multipole moments which created a 3ω torque, where ω is the outer turntable rotation rate. The injected torque from the outer spheres on the inner spheres has an analytic expression when the turntable is centered radially on the pendulum spheres.

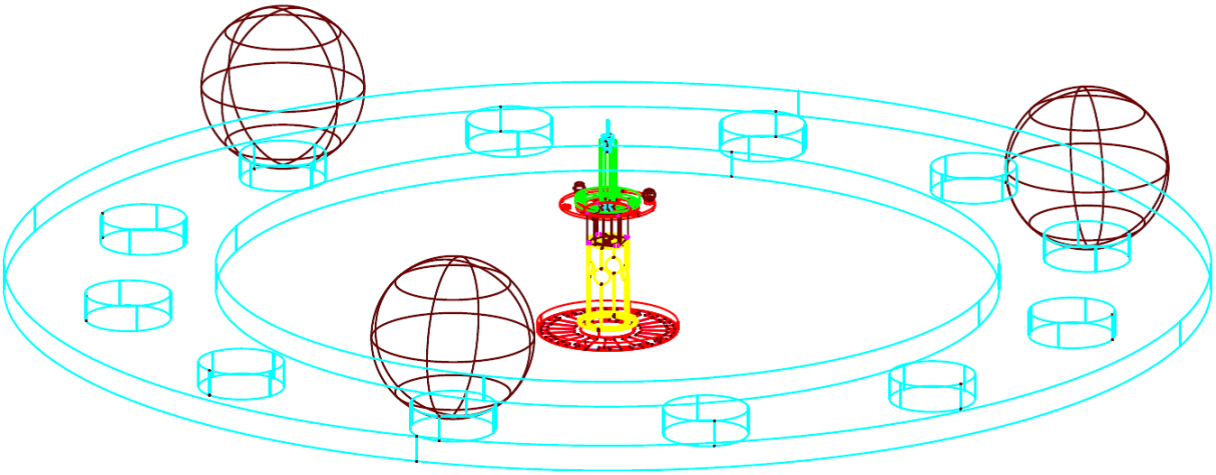

Figure 8.1: **Gravitational model of pendulum and calibration turntable** - The model was generated and calculated in `MULTIN`.

$$N(\phi, z) = 3GMmrR \sum_{i=0}^{2} \frac{\sin(\phi + i2\pi/3)}{(r^2 + R^2 + z^2 - 2rR\cos(\phi + i2\pi/3))^{3/2}} \tag{8.4}$$

We calculated the torque at various angles and fit for the 3^{rd} harmonic. We also numerically estimated the dependence of the predicted torque amplitude on the geometric parameters (R, r, m, M, z) by computing the derivatives and again fitting for the 3^{rd} harmonic.

8.3.1 Centering the turntable laterally

Centering requirements for the calibration turntable on the pendulum were less strict in this iteration of the experiment due to the increased diameter of the outer turntable. The 3ω torque signal was quite insensitive to misalignments of the turntable axis to the pendulum position. A 1cm horizontal displacement gave only a $\sim$ 1% increase in torque, but the turntable was limited to displacements of $\sim$ 8mm around the apparatus. To center the turntable laterally, we employed the same method as in previous iterations [36]. In addition

to the three spheres on the outer turntable, we placed a pair of additional spheres sitting opposite each other on the turntable. These created large $Q_{2,2}$ and $Q_{4,4}$ moments which coupled to the $q_{3,3}$ moment of the pendulum calibration spheres when radially mis-centered. In the frame of the outer turntable, a translated pendulum $q_{3,3}$ moment becomes a $q_{4,4}$. The centering procedure consisted of translating the outer turntable in the two axes of the plane to minimize the 4ω measured torques. The 4^{th} harmonic was used instead of the 2^{nd} since simple tilts and other defects couldf show up as $q_{2,2}$ moments of the pendulum.

theoretical calculation

The theoretical 3ω calibration torque for the laterally displaced turntable was calculated with `MULTIN` and checked with the `PointMatrix Gravity` library [26]. The pendulum was designed to have minimal $q_{4,4}$ moment, but it was not identically zero. With the centering spheres in place we saw a slight contribution to the 3ω torque with horizontal displacement. The torques were calculated by computing the inner moments of the pendulum and the outer moments of the calibration turntable. The assumption of rotating inner moments and translating the outer moments laterally was equivalent to rotating outer moments and translating the pendulum, allowing us to map out the 3 and 4ω torques as a function of outer turntable position using `MULTIN`.

We used `PointMatrix Gravity` as a second method of computing the torques. The relevant components of the pendulum with 3-fold and 4-fold symmetry as well as the calibration turntable were approximated with discrete points with masses matched to the uniform density of the corresponding components. The calibration turntable points were translated and rotated to compute torques on the pendulum at each angle and position and then fit for the harmonic content.

The above calculations verified that the translation of the inner $q_{3,3}$ moment from the pendulum spheres were the only nontrivial contribution to the 4ω torque, giving rise to a 4ω torque amplitude linear in the displacement from centered. The calculations also validated the observed coupling to the 3ω signal with translations as well.

Lateral Centering Fit

Having verified that the translation of the inner $q_{3,3}$ moment contributed linearly in displacement from the origin to an inner $q_{4,4}$ and hence 4ω torque, [23] eqn.14, we then performed a weighted linear fit to our cosine and sine amplitudes and errors as a linear function of calibration turntable position (x^c, y^c).

$$N_c(x^c, y^c, x_0^c, y_0^c) = c_0(x^c - x_0^c) + c_1(y^c - y_0^c) = c_0 x^c + c_1 y^c + c_2$$
$$N_s(x^c, y^c, x_0^c, y_0^c) = s_0(x^c - x_0^c) + s_1(y^c - y_0^c) = s_0 x^c + s_1 y^c + s_2$$

Here, the radially centered position of the calibration turntable is (x_0^c, y_0^c). A re-arrangement of the fit coefficients $(c_0, c_1, c_2, s_0, s_1, s_2)$ gave the center positions, and the errors propagate from the linear fit using the Jacobian.

$$(x_0, y_0) = \left(\frac{c_2 s_1 - c_1 s_2}{c_1 s_0 - c_0 s_1}, \frac{c_0 s_2 - c_2 s_0}{c_1 s_0 - c_0 s_1} \right)$$
$$\nabla x_0 = \left[\; s_1 x_0, \quad s_1 y_0, \quad s_1, -c_1 x_0, -c_1 y_0, -c_1 \right] \frac{1}{c_1 s_0 - c_0 s_1}$$
$$\nabla y_0 = \left[-s_0 x_0, -s_0 y_0, -s_0, \quad c_0 x_0, \quad c_0 y_0, \quad c_0 \right] \frac{1}{c_1 s_0 - c_0 s_1}$$

Figure 8.2 shows our lateral centering data cosine and sine fits with errors. The measured center position of the calibration was found to be $(x_0^c, y_0^c) = (-312.08 \pm 0.12, -317.27 \pm 0.12)$ mm. The calibration uncertainty contribution to the 3ω signal is discussed in section 8.4.

8.3.2 Centering the turntable vertically

We centered the turntable vertically by removing the two extra lateral centering spheres and then translated the turntable vertically. The z-axis of the calibration turntable stage had a much larger range of motion so we could directly look to maximize the 3ω torque as a function of the turntable position, fig 8.3. The vertical center of the calibration turntable was found to be $z_0^c = -291.32 \pm 0.53$ mm.

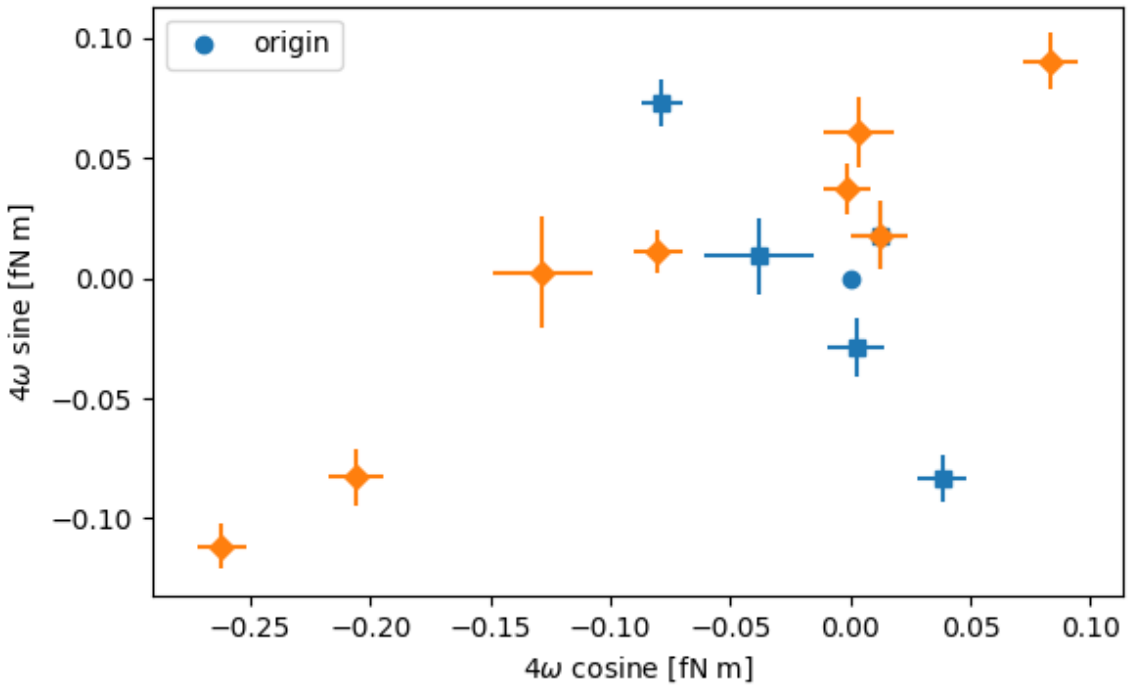

Figure 8.2: **Calibration 4ω centering torque signal at various turntable (x, y) positions with pendulum position fixed** - We laterally translated the calibration turntable about the pendulum to center horizontally by minimizing the 4ω torque. Measurements taken by translating along the x-axis are shown in blue with squares, and along the y-axis in orange with diamonds.

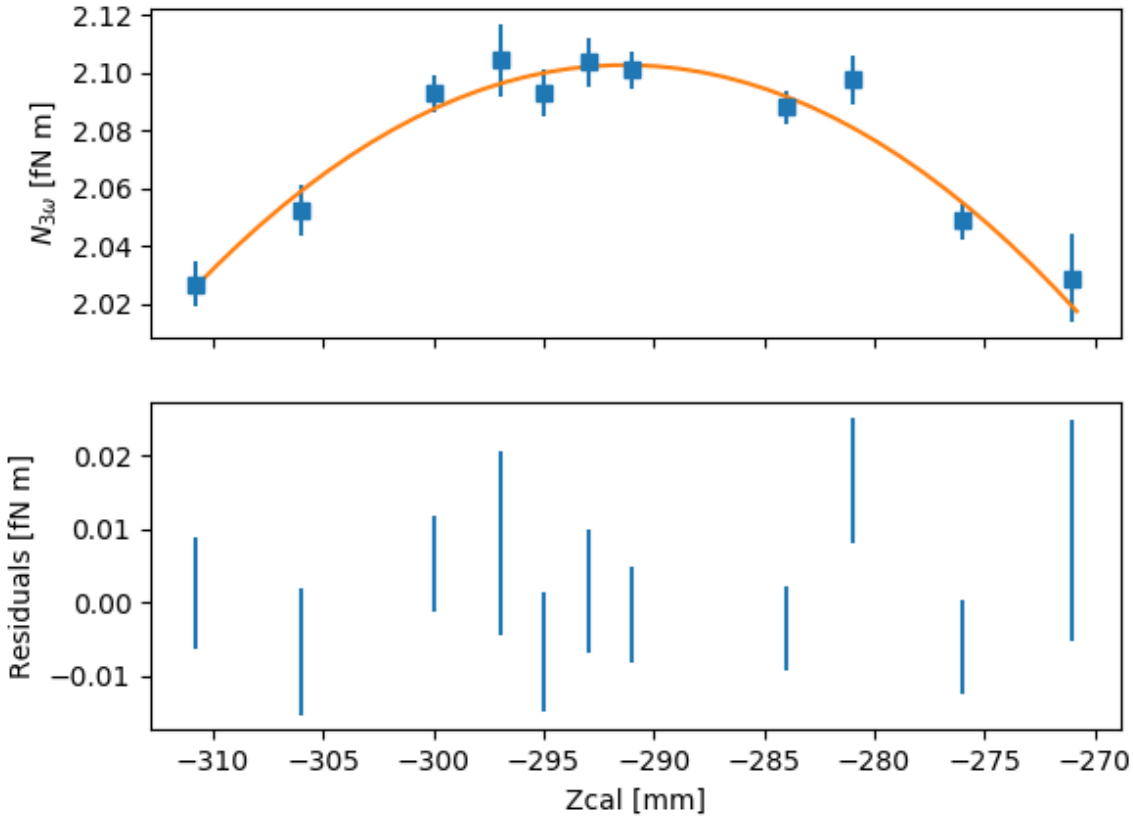

Figure 8.3: **Calibration 3ω torque signal as a function of turntable vertical height at a fixed pendulum position** - We translated the calibration turntable about the pendulum to align vertically by maximizing the 3ω torque. Measurements are shown in blue with a quadratic fit in orange.

8.4 Calibration data

The calibration data were taken approximately every two weeks at a fixed pendulum and calibration turntable position to verify the stability of the angle readout, see fig 8.4. The lateral and vertical positioning of the turntable were measured after a majority of the science data were taken. The initial rough alignment of the calibration turntable led to a correction to the predicted calibration values. The vertical misalignment was 3.65 ± 0.53 mm and the lateral misalignment was 6.78 ± 0.17 mm. We used the measured quadratic fit to the vertical displacement data to determine the vertical displacement correction of $-2.70 \pm 0.79 \times 10^{-3}$ fNm. We used a quadratic fit to the theoretical radial displacement calculations to determine the radial displacement correction of $4.20 \pm 0.21 \times 10^{-3}$ fNm.

The theoretical prediction was based purely on the coupling to the 3−fold spheres on the pendulum. We verified that no other parts of the calibration turntable or pendulum contributed to the 3ω torque by measuring the 3ω torque in two null configurations. We measured the torque from the calibration turntable with the large outer spheres removed acting on the pendulum and pendulum spheres (run6911). We also measured the torque from the calibration turntable with large outer spheres acting on the pendulum with the pendulum spheres removed (run7377, run7379, run7381, run7383, run7385). Neither null configuration resolved a 3ω torque at 2σ. More measurements without the external calibration spheres would have resulted in a lower statistical uncertainty in the torque calibration measurement. A full list of calibration runs and calibration centering runs can be found in Appendix A.

8.4.1 Metrology

The inner calibration spheres were weighed on a Sartorius LA310S analytical balance with .1mg resolution that is calibrated yearly by NorthWest Instrument Services. The outer calibration spheres were weighed on a Citizen CT-8000H, 8000g × .1g resolution scale. The scale calibration was checked with a class M2 2kg weight with an uncertainty of .3g which was a factor of 5 better than the scatter of the masses in the three large spheres used for the

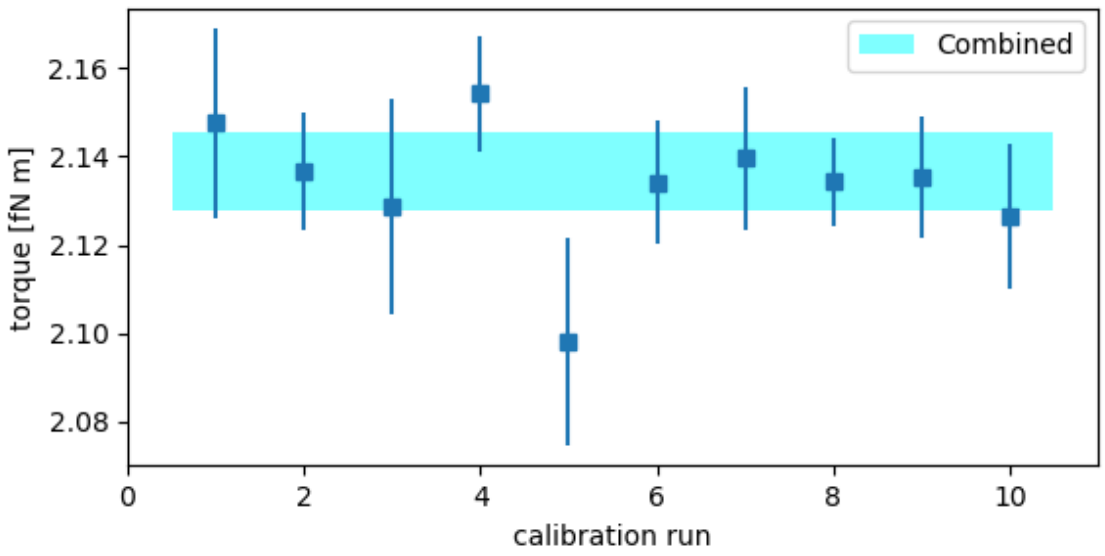

Figure 8.4: **Measurements of the calibration turntable over the course of the data taking** - Each point represents a single calibration run measurement of the 3ω torque assuming the nominal autocollimator geometric calibration discussed in 8.1. The blue band is the combined mean calibration torque with uncertainty.

calibration. The bolt circle that set the radial position of the inner spheres, r, was measured with the edge-tracing routine of the SmartScope.

We measured the tilt of the calibration tray relative to its rotation axis, θ_C, with a dial indicator at a fixed position as it rotated. We measured the runout of the calibration tray relative to the rotation axis, δ_r, with a dial indicator. Both were found to deviate by less than 1mm.

8.4.2 Error table

Below we list the measured components and error contributions to the calibration scale, table 8.1. The dominant errors comes from the uncertainty in radial position of the inner and outer spheres. The error contributions from the radial positions were estimated from the analytic formula for the 3ω torque, equation 8.4. We included corrections to the predicted torque since the final centering of the calibration turntable was performed after the majority of the science and calibration data were taken. The mis-centering in vertical position lead to a smaller torque whereas the radial mis-centering lead to a larger calibration signal. Torque corrections from the runout and tilt of the calibration turntable were negligible.

Quantity	Value	Uncertainty	δN (fNm)	σ_N (fNm)
G	6.6742×10^{11} m^3 kg^{-1} s^{-2}	-	-	-
m	4.8159×10^{-4} kg	1.0×10^{-7} kg	-	2.09×10^{-4}
M	1.1366 kg	.0014 kg	-	1.25×10^{-3}
r	1.648×10^{-2} m	1.1×10^{-5} m	-	2.71×10^{-3}
R	1.905×10^{-1} m	6.0×10^{-5} m	-	3.33×10^{-3}
δ_0	6.78×10^{-3} m	1.68×10^{-4} m	4.75×10^{-3}	2.35×10^{-4}
ζ_0	3.65×10^{-3} m	5.31×10^{-4} m	-2.70×10^{-3}	7.85×10^{-4}
θ_C	7.87×10^{-3} rad	5.25×10^{-5} rad	-2.28×10^{-6}	2.22×10^{-4}
δ_r	0.44×10^{-3} m	0.01×10^{-3} m	1.00×10^{-5}	5.62×10^{-4}
N_{cal}	$2.1094 + .0021$ fNm		0.0046 fNm (systematic)	
N_{meas}	2.1368 fNm		0.0089 fNm (statistical)	
$\gamma = \frac{N_{Meas}}{N_{Cal}}$	1.012	0.0047		

Table 8.1: Calibration scale error table. Various geometric, mass, and position measurements contributed to the uncertainty of the predicted calibration torque. The ratio of the measured torque assuming the nominal autocollimator calibration and moment of inertia relative to the predicted torque gave the overall calibration scale.

Chapter 9

STATISTICAL NOISE SOURCES

A variety of noise sources contributed to the torque measurements, often increasing the torque noise at the closest pendulum to screen separations.

9.1 Thermal Fiber noise

The measured angle θ from the torsion balance could be modeled as a harmonic oscillator with moment of inertia I, spring constant κ, viscous damping coefficient Q_v, internal damping coefficient Q_a, and forcing torque τ.

$$I\ddot{\theta}(t) + \frac{I\omega_0}{Q_v}\dot{\theta}(t) + \kappa\left(1 + \frac{i}{Q_a}\right)\theta(t) = \tau(t)$$

Here the undamped free oscillation frequency is given as $\omega_0 = \sqrt{\kappa/I}$. The Fluctuation Dissipation Theorem implies that the pendulum experiences random thermally driven torques with a frequency spectrum of

$$\langle\tau^2(\omega)\rangle = \frac{4k_BT}{\omega}$$

The angle thermal noise is then given by

$$\langle\theta^2(\omega)\rangle = \frac{4k_BT}{\omega}\left(\frac{\omega}{\omega_0 Q_v} + \frac{1}{Q_a}\right)\frac{1}{\left(1 - \left(\frac{\omega}{\omega_0}\right)^2\right)^2 + \left(\frac{\omega}{\omega_0 Q_v} + \frac{1}{Q_i}\right)^2}$$

At the lowest frequencies ($\lessapprox$ .01Hz), this thermally driven noise dominated our torque noise spectrum. Throughout our analysis, we treated the velocity damping component as negligible, $Q_v \to \infty$. Velocity induced damping however could arise from magnetic noise, pressure noise, or electrostatic noise.

9.2 Autocollimator

The major contribution to statistical noise at high frequencies ($\sim$ 0.01-1Hz) was from the autocollimator. It was characterized by $1/f^2$ noise in power leveling off into white noise at about 0.1Hz. It was likely dominated by electronic voltage noise and flicker noise at low frequencies.

9.3 Separation-Dependent Noise Sources

The thermal fiber torque noise and autocollimator read-out noise were well understood and characterized, but there existed several other potential sources of torque noise that depended on the pendulum separation to the screen.

9.3.1 Seismic Patch-field Coupling

One relevant statistical source of noise was the coupling of seismic translation noise into the twist motion. This translation to twist coupling was much stronger at smaller separations between the pendulum and the screen. This was strong evidence that the coupling arose from the non-linear dependence of the equilibrium angle and the free torsional period on the "patch"-fields as discussed in section 10.2.2 below. The seismic environment was noticeably noisier during the day especially due to the bus routes that pass near the lab. Large twist impulses were often coincident with pendulum-screen capacitance impulses suggesting an excitation of the vertical translation mode "bounce" amplitude, see figure 9.1. The torque noise at pendulum separations below 30 μm was significantly larger during the day with impulses that often exceed the detector range when operated outside of the hours of 2-6am (when the public buses were not running). In fact the data run at the closest pendulum-screen separation was during a campus and bus route closure due to snow. This seismic coupling motivates several potential upgrades for this experiment.

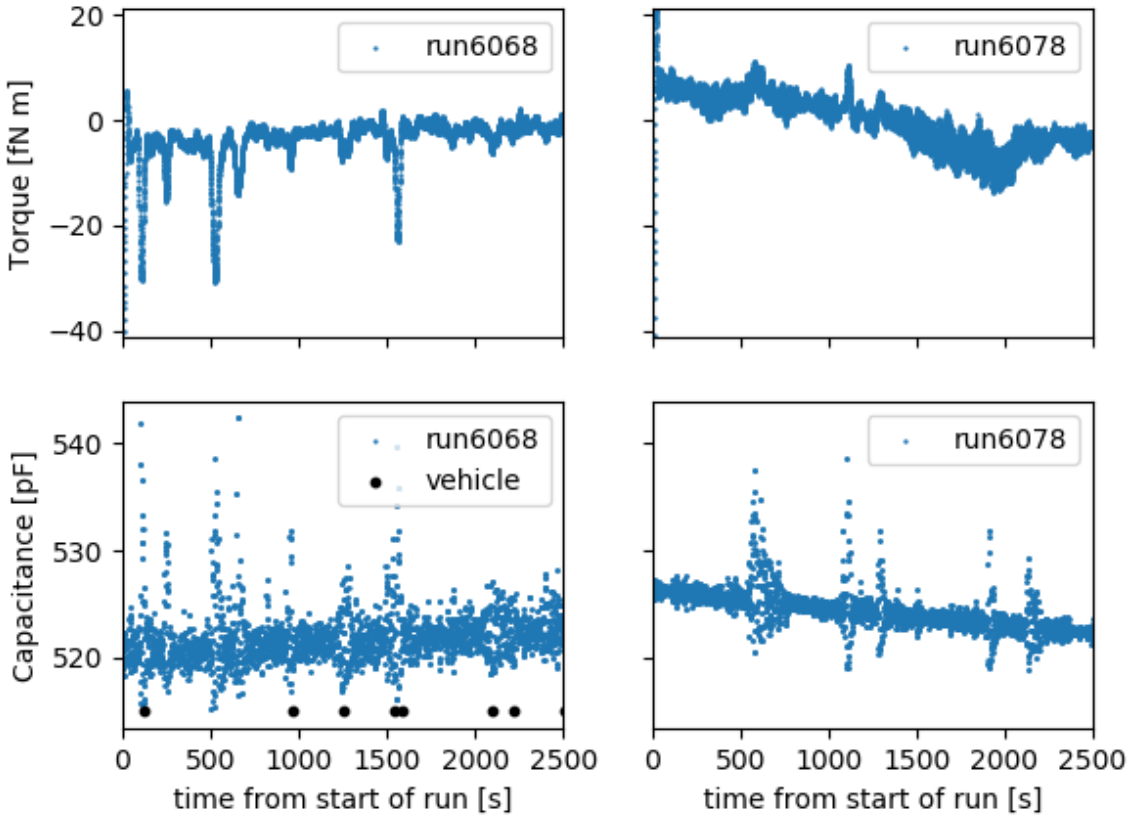

Figure 9.1: **Seismic disturbance effect on torque from pendulum-screen tilt misalignment** - The top figures show the torque time-series constructed from the twist angle data of run6068 (left) and run6078 (right) with low-pass filter applied at .03Hz. The bottom figures show impulses in the corresponding pendulum-screen capacitance suggestive of ground motion. Trucks or buses driving on a nearby road were heard at the lab at times indicated in the lower left plot, often in correspondence with impulses in the capacitance and unidirectional impulses in torque. The direction and magnitude of the torque impulses changed with the alignment of the pendulum test-mass plane to the electrostatic screen plane.

9.3.2 Patch-field Potentials

It was assumed that a significant source of noise at close separations was due to the interaction of random patch potentials on the gold-coated surfaces of the pendulum test mass and the beryllium-copper screen. As the pendulum horizontally or vertically translates, it experiences many random torques from the various patch potentials, likely due to random crystal orientations of the gold-coatings [12], surface flaws, and dust and other contaminants[29]. This would contribute to the seismic coupling.

Estimates of the torque noise contributions due to Speake and Trenkel, and Behunin, et al. suggest a noise model dependent on the spatial correlations of the patch potentials. They derived the force between two planes separated by a vertical distance, D, for a translation in horizontal direction x.

$$\mathcal{F}_x(x) = \epsilon_0 \int \frac{d^2k}{(2\pi)^2}(-ik_x)\frac{ke^{ik_x x}}{\sinh kD} V_1[-\boldsymbol{k}]V_2[\boldsymbol{k}] \tag{9.1}$$

The lateral force power spectrum could then be determined by known two-dimensional spatial distributions of the patch potentials of the two surfaces, $V_1[\boldsymbol{k}]$ and $V_2[\boldsymbol{k}]$, and frequency dependent translation amplitudes. A torque power spectrum could be determined similarly.

The spatial distribution of patch potentials in our experiment could be determined through scanning Kelvin probe microscopy (SKPM) measurements with an atomic force microscope (AFM), but the typical scan area of an AFM is on the order of $1\mu\text{m}^2$ which would rule out scanning the entire surface of either the electrostatic screen or the pendulum test-mass which has an area of about 2000 mm^2. Our experiment also had a stationary electrostatic screen separating the pendulum test-mass from any motion of the attractor, so any torque noise would necessarily stem only from the small amount of motion in the pendulum test-mass or fluctuations of the patch potentials. For now, this statistical noise source appears both difficult to predict and to measure definitively.

9.3.3 Squeeze-Film Damping

Another potential Brownian noise source was gas damping of the torsion pendulum. In the high vacuum of this experiment, the mean free path of gas molecules was longer than the size of the pendulum, known as the molecular flow regime. The damping could be characterized by a viscous damping term, $\gamma_\infty = -\frac{dN}{d\phi}$, with torque noise given by the fluctuation-dissipation theorem, $S_N = 4k_BT\gamma_\infty$. Cavalleri et. al. gave a method to estimate damping coefficients in an infinite volume given parallel and perpendicular force noise models [14]. The noise models assumed molecules with a Maxwell-Boltzman distribution and desorption with an angular cosine distribution. These two assumptions give rise to the parallel and perpendicular force noise terms on a surface:

$$\begin{aligned} S_\parallel &= p\left(\frac{8m_0k_BT}{\pi}\right)^{1/2} &&= 4k_BT\left(\frac{p}{v_T}\right)\left(\frac{1}{2\pi}\right)^{1/2} \\ S_\perp &= p\left(\frac{32m_0k_BT}{\pi}\right)^{1/2}\left(1+\frac{\pi}{4}\right) &&= 4k_BT\left(\frac{p}{v_T}\right)\left(\frac{2}{\pi}\right)^{1/2}\left(1+\frac{\pi}{4}\right). \end{aligned}$$

where p is the pressure, T is the temperature, k_B is Boltzmann's constant, m_0 is the mass of the molecules in the gas, and v_T is the thermal velocity, $v_T = \sqrt{\frac{m_0}{k_BT}}$. For this experiment, the relevant geometry was an annulus. The calculations are as follows:

$$\begin{aligned} S_N^{Ann.} &= 2\int_Z \left[r^2S_\parallel\right]rdrd\theta + \int_{IR}\left[r_i^2S_\parallel\right]r_idzd\theta + \int_{OR}\left[r_o^2S_\parallel\right]r_odzd\theta \\ &= 2\int_{r_i}^{r_o}\int_0^{2\pi}\left[r^2S_\parallel\right]rdrd\theta + \int_{-t/2}^{t/2}\int_0^{2\pi}\left[r_i^2S_\parallel\right]r_idzd\theta + \int_{-t/2}^{t/2}\int_0^{2\pi}\left[r_o^2S_\parallel\right]r_odzd\theta \\ &= \left[\pi\left(r_o^4-r_i^4\right)+2\pi t\left(r_o^3+r_i^3\right)\right]S_\parallel \end{aligned}$$

There should also have been an effective increase in pressure as two macroscopic surfaces come close to each other in the presence of a gas. This can be visualized in that a gas molecule will bounce back and forth many times in the small separation gap rather than traveling through the narrow range of angles to exit the gap. We estimated this proximity-enhanced gas damping with the heuristic given in [22] as follows

$$\gamma_s = \gamma_\infty \frac{\left(\frac{s}{d}\right)^2}{\log\left(\left(\frac{s}{d}\right)^2 + 1\right)}$$

where d was the distance to the nearest macroscopic surface and s was the average radius of the test-mass.

We estimated the contribution to torque noise at different separations for the current geometry with filled wedges. Our estimate was made with the assumption that effective increase in pressure with separation is uniform across the annulus. In reality, the diffusion time of a particle emitted near the edge of the test-mass annulus should be smaller than one emitted at half the radius which should de-weight the torque noise at larger radii on the test-mass surface. The calculations suggested that some portion of excess torque noise at the smallest pendulum-screen separations could be associated to squeeze-film damping. This could be further studied by measuring decay time of the pendulum as a function of pressure, using a residual gas analyzer to determine the gas species present in the system, and performing a Monte-Carlo calculation to predict the true scaling dependence on separation.

9.3.4 Magnetic Noise

Another source of separation dependent noise arises from thermally driven currents in the conductive electrostatic screen. These currents could produce magnetic fields that would couple to any permanent magnetic moment in the pendulum M and create a torque noise with a dependence on separation to the screen. Varpula and Poutanen, [56], derived an expression for the thermal magnetic field noise parallel to an infinite conductive slab of thickness t, conductivity σ, permeability μ, and at a separation z, so that the torque noise about the fiber is

$$N_z = m \times B_\parallel = \frac{M}{\sqrt{2}} \frac{\mu}{2} \sqrt{\frac{\sigma k T t}{2\pi}} \frac{1}{z} \frac{1}{\sqrt{1 + \left(\frac{2f_c}{\pi f}\right)^2}},$$

where the cutoff frequency f_c is defined as

$$f_c = \frac{1}{4\mu\sigma z t}.$$

For the 10 μm thick beryllium-copper screen at a distance of 5 μm separation, the magnetic field noise would be approximately 0.5 nT. Measurements of the pendulum torque from a modulated horizontal magnetic field suggest the pendulum magnetic moment was approximately 1.02×10^6 fNm/T. This noise source was unlikely to cause any significant effect in the measurements at the current achievable separations and sensitivity.

Chapter 10

SYSTEMATIC EFFECTS

In addition to the various statistical noise sources, systematic torques could arise from gravitational, thermal, electrostatic, or magnetic interactions. We typically constrained the torques from a given systematic effect S, in one of two ways. In the first method, we exaggerated S by a factor f_e compared to its typical value in the science data. Then, with the attractor rotating, we measured the induced change in torque, ΔN^m with $m = 18, 54, 120\omega$. The systematic torque in the science data was then $N_S^m = \frac{1}{f_e}\Delta N^m$. This method was used to determine the systematic torques from static magnetic fields and electrostatic potentials. In the second method, we modulated S at a definite frequency and measured the sinusoidal amplitude and phase of S, (A_S^f, ϕ_S^f) and the resulting torque, (A_N, ϕ_N). We defined a coupling constant as the ratio of the amplitude of the torque to the amplitude of the modulated systematic, $C_S = \frac{A_N}{A_S^f}$ and a phase delay from the difference in phases, $\Delta\phi = \phi_N - \phi_S$. We then fitted the science data for the sinusoidal amplitude and phases of the systematic during normal operation in the signal frequencies. We derived the systematic torque in each component and signal harmonic from the measured coupling constant and then rotated each component by the phase delay, $N_S^m = C_S A_S^m e^{i\phi_S^m} e^{i\Delta\phi}$. This method was used to find couplings to temperature and dynamic magnetic fields. We calculated uncertainties $\sigma_{N,S}$ using standard error propagation methods.

We subtracted the systematic torques from our science data and included the error in quadrature if the signal was resolved at 2σ, that is $(|N_S| - 2\sigma_{N,S}) > 0$. If the systematic torque was not well resolved, we bounded the systematic torque error contribution by an effective systematic torque uncertainty $\widehat{\sigma}_S = |N_S| + |\sigma_{N,S}|$ and added the error in quadrature.

10.1 Magnetic Torques

A magnetic systematic torque could arise in several possible ways. Our biggest concern in the test-mass fabrication process was avoiding introducing some permanent magnetization through contamination in the EDM or gluing processes. Concerns about this systematic were somewhat mitigated through the dedicated AMR probe measurements, see Chapter 6. We also worried about an induced magnetization from a static magnetic field. A static magnetic field would lead to a magnetization in the shape of the test-mass pattern due to the difference in magnetic volume susceptibility of Platinum to Stycast 1266, $\chi_{Pt} = 2.667 \times 10^{-4}$ [20] and $\chi_{1266} = -8.859 \times 10^{-6}$ [7]. One test-mass magnetized in a static magnetic field could couple to a permanent magnetization in the other test-mass (which would be a coupling linear in the magnetic field) or to the induced magnetization in the other test-mass (which would be quadratic in the magnetic field). Finally, if the pendulum had a residual permanent magnetic dipole moment perpendicular to the fiber axis, it could couple to an oscillating horizontal magnetic field. We performed measurements to constrain all three of these possibilities.

10.1.1 Static Magnetic Fields

We searched for a systematic torque dependent on the application of a static magnetic field by applying a magnetic field from a pair of 190-turn, 91cm diameter coils in a Helmholtz configuration separately along all three axes of the apparatus and with a total pendulum-attractor separation of 72μm. For reference, the $z-$axis of the instrument was defined to be local vertical, the $y-$axis was oriented horizontally along the axis of the autocollimator, and the $x-$axis perpendicular to both. Science data were taken with a two sets of mu-metal magnetic shields: one external to the apparatus and another inside the apparatus. For each orientation of an applied field (B_X, B_Y, B_Z), we performed tests both with all shields in place and with one portion of the external shields removed and at various field amplitudes. We observed a quadratic dependence of the 120ω torques on the applied magnetic field in all cases. This quadratic effect in the 120ω torques was consistent with an induced

magnetization in the wedge pattern such that both the sign of the curvature and relative amplitudes matched expectations. The only significant systematic torque arose from the 120ω B_Z-dependent signal. We tested the separation dependence of the B_Z torque which also matched predictions from `FBESSELN`. Further details of each set of measurements are given below.

120ω torque dependence on B_Z

In the vertical field case, we observed a systematic torque with quadratic dependence on the applied field with positive curvature and a minimum at $B_Z = (64 \pm 1)\mu$T, see figure 10.1. The positive curvature agreed with the intuitive picture of the wedges magnetized as dipoles aligned with the vertical field (platinum is paramagnetic) creating an additional attractive torque. Measurements without the external magnetic shield allowed us to better determine the position of the quadratic minimum. A permanent pendulum magnetic dipole moment could not experience a torque about the fiber from a vertically oriented field, and therefore we expected no linear coupling. We confirmed this after removing the pendulum by measuring the ambient vertical magnetic field with an AMR probe in the pendulum position to be $(61 \pm 2)\mu$T with statistical error only, largely coming from the Earth's magnetic field. This confirmed that the torque minimum occurred where B_Z bucked the ambient magnetic field and that there was no evidence for a linear magnetic coupling. The systematic torque contribution from the external static vertical magnetic field to the 120ω signal at $s = 72\mu$m was 0.0165 ± 0.0054 fNm.

120ω torque dependence on B_X, B_Y

The quadratic dependence of the 120ω torques on horizontally oriented applied magnetic fields, see figures 10.2 and 10.3, was also consistent with an induced magnetization in the wedge pattern. The negative curvature and roughly $20\times$ smaller effect again agreed with the intuitive picture of wedges magnetized as dipoles aligned with the horizontal field, where the torque is repulsive and $2\times$ smaller. In addition the inner shield attenuated horizontal fields

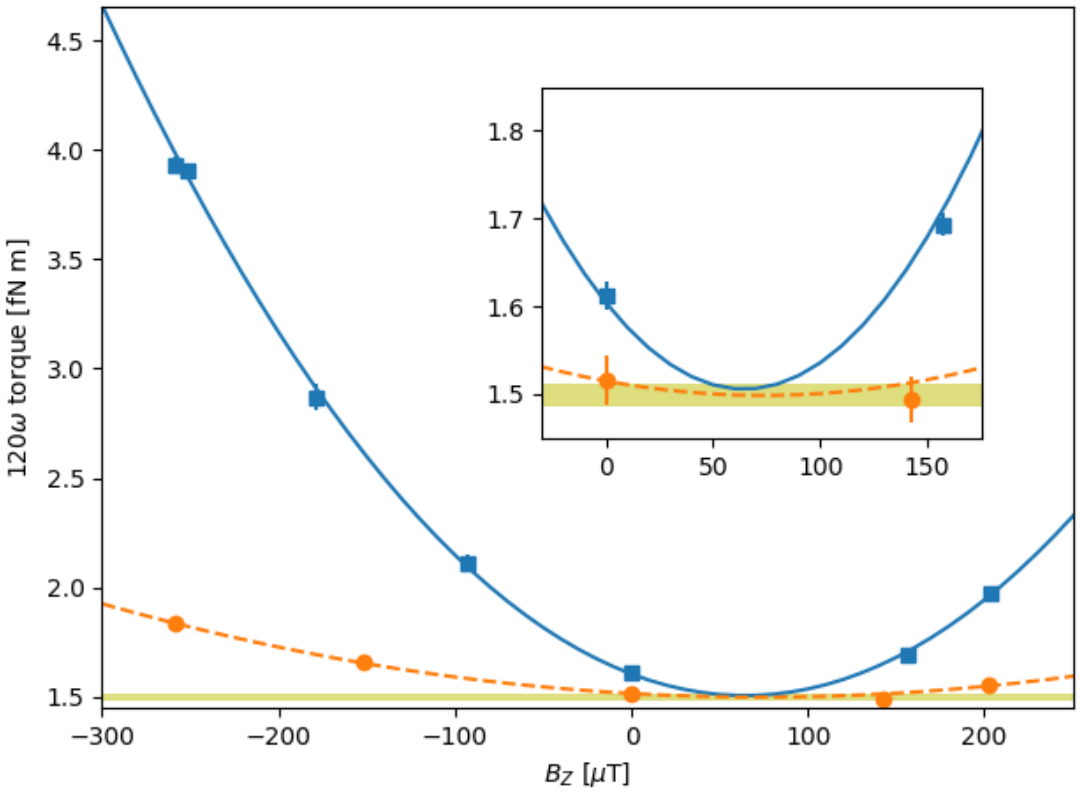

Figure 10.1: 120ω **torque dependence on** B_Z - Measurements of the 120ω torque taken at $s = 72\mu$m without the external magnetic shield (blue points) and with all shields in place (orange points) show a quadratic dependence on B_Z with positive curvature. The curves show a quadratic fit to the data. The yellow band shows the average torque measurement taken in the science data at the same separation. The inset shows the location of the torque minimum where the applied field cancels the Earth's field, $B_Z = (64 \pm 1)\mu$T.

more effectively than vertical. In both field orientations, measurements without the external magnetic shield allowed us to better determine the position of the quadratic maximum. The B_X, B_Y values at these maxima were sensitve to both induced magnetization from external horizontal fields and from linear magnetic couplings. Unlike the vertical field orientation, a horizontal magnetic field coupled to a permanent horizontal magnetic moment could cause

a torque on the pendulum about the fiber axis. After removing the pendulum, we also measured the x- and y-oriented magnetic fields in the pendulum position, $(8 \pm 2)\mu$T and $(8 \pm 2)\mu$T respectively. We concluded that the pendulum dipole coupled to an applied magnetic field in the x-direction. The systematic torque contributions from the external static horizontal x,y-magnetic fields to the 120ω signal at 72μm were (0.0026 ± 0.0040) fNm and $(0.0008 \pm .0071)$ fNm, respectively. These systematic torques were unresolved and again negligible compared to the torque measurement errors at that close separation.

18ω, 54ω torque dependence on B

The torque coupling to applied magnetic field was unresolved in the 18ω and 54ω torque measurements for all field orientations. This was also consistent with an induced magnetization when compared to Fourier-Bessel calculations. We bounded a systematic torque contribution at these signal frequencies based on the Fourier-Bessel calculations of a magnetization which matched the 120ω systematic torques with less than 1 aNm each at $s = 72\mu$m.

Separation dependence & Systematic Effect

The only relevant systematic torque came from the vertically-oriented induced magnetization in the platinum wedges from the external field through the two layers of magnetic shielding. This B_Z torque had a dependence on the test-mass separation that was readily calculable with the Fourier-Bessel decomposition. We measured $s-$dependence of the B_Z torque as the difference in the torque with a strong field ($B_Z = -250\mu$T and external shield removed) and a nulled field ($B_Z = +66\mu$T with all shields in place). The measurement agreed with the `FBESSELN` predictions of a set of wedges with a uniform vertical magnetization with one overall normalization factor, see figure 10.4. This further confirmed the induced magnetization as the origin of the systematic torque.

We calculated the $s-$dependence of each of the harmonics at a fixed magnetization using `FBESSELN` and then scaled the result to match the 120ω systematic measurement (the best resolved effect) taken at 72μm, .0165 fNm. In this calculation we assumed the magnetization

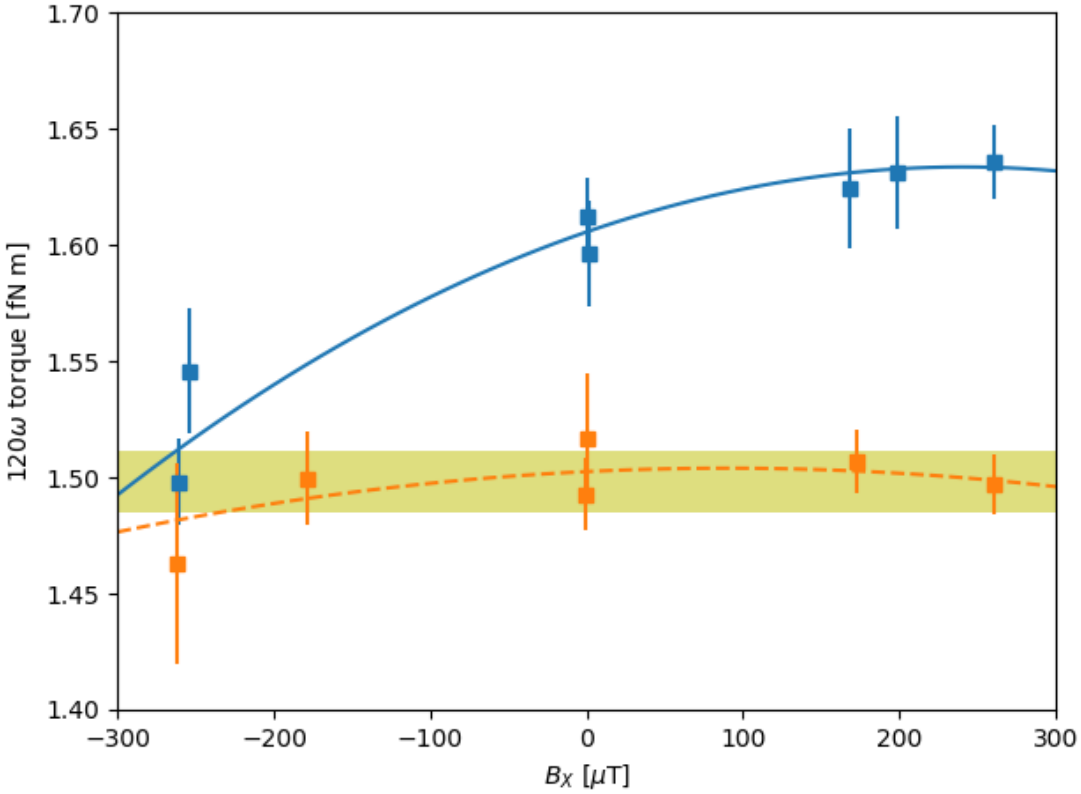

Figure 10.2: 120ω **torque dependence on** B_X - Meaurements of the 120ω torque taken at $s = 72\mu$m without the external magnetic shield (blue points) and with all shields in place (orange points) show a quadratic dependence on B_X with negative curvature. The curves show a quadratic fit to the data. The offset vertically between the two curves comes from the systematic coupling to the vertical component of the Earth's field. The yellow band shows the average torque measurement taken in the science data at the same separation. There is a significant linear coupling to the pendulum magnetic dipole.

was uniform across the test-masses, the test-masses were linearly magnetized due to their difference in susceptibilities, and that the separation dependence was consistent solely with the quadratic coupling of the induced magnetization in the wedges, all evidenced by the single scale factor for the separation dependent measurements and the consistency of the

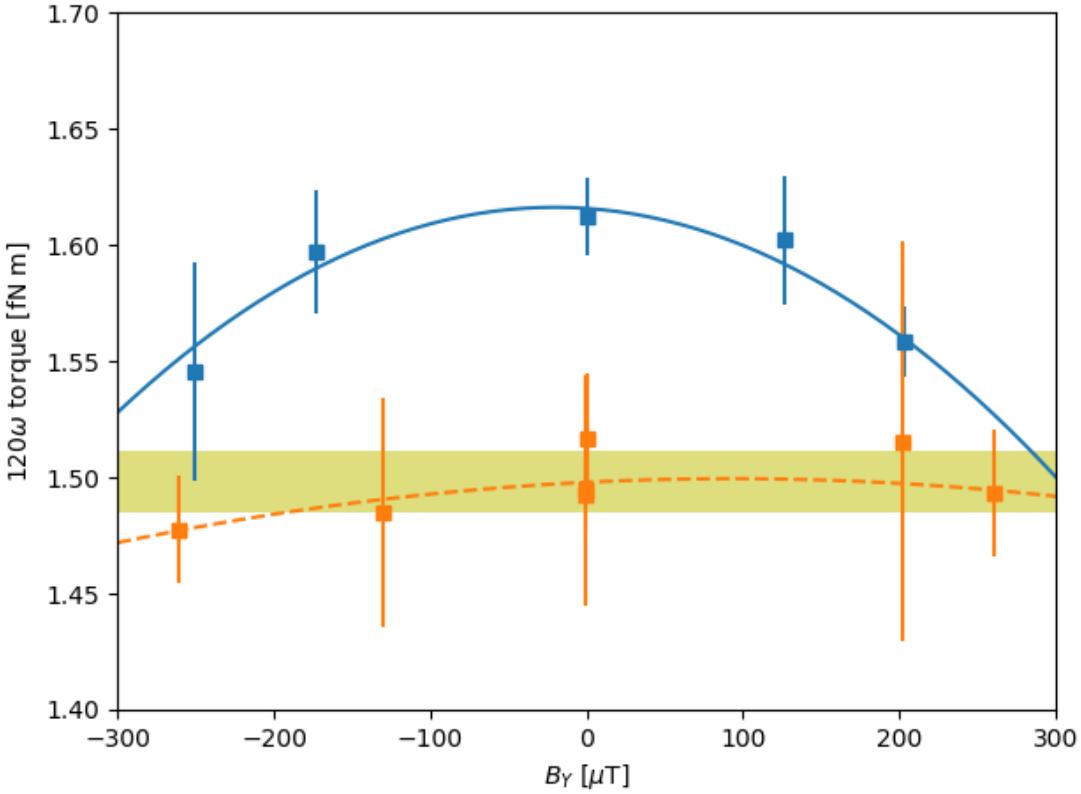

Figure 10.3: 120ω **torque dependence on** B_Y - Meaurements of the 120ω torque taken at $s = 72\mu$m without the external magnetic shield (blue points) and with all shields in place (orange points) show a quadratic dependence on B_Y with negative curvature. The curves show a quadratic fit to the data. The offset vertically between the two curves comes from the systematic coupling to the vertical component of the Earth's field. The yellow band shows the average torque measurement taken in the science data at the same separation.

field offsets with the location of the quadratic minimum of the torque measurements. We estimated the other harmonic corrections using the same scale factor. We subtracted the systematic vertical magnetic field torque, $N_B^m(s)$ computed from `FBESSELN` from each of the measured torque harmonics. It was notable that the separation dependence of the 120ω, B_Z torque was nearly identical to the that arising from gravity so that the correction was almost

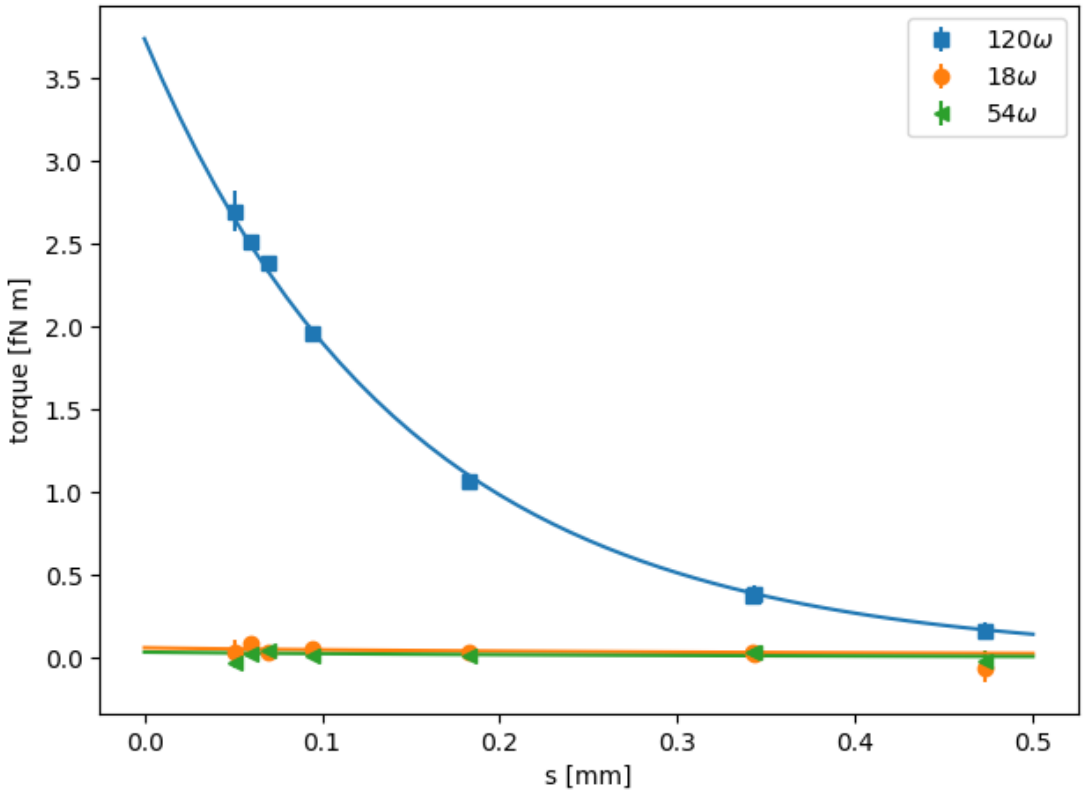

Figure 10.4: **Systematic B_Z torques as a function of test-mass separation** - Each point is the difference in torques measured with a strong vertical field ($B_Z = -250\mu$T and external shield removed) and a nulled field ($B_Z = +66\mu$T with all shields in place). The curves are Fourier-Bessel calculations of the spin-spin torque from the induced magnetization of the test-masses, all scaled by a single factor to match the data.

equivalent to scaling the 120ω torque data by a factor of 0.989 ± 0.004.

10.1.2 Dynamic Magnetic Fields: Pendulum Dipole Coupling

A permanent pendulum magnetic dipole oriented perpendicular to the fiber axis could produce a systematic torque if it coupled to a magnetic field oriented perpendicular to both the fiber and dipole oscillating at one of the signal frequencies. To measure the pendulum dipole coupling, we applied an oscillating magnetic field by driving a sinusoidally varying current through a pair of 190-turn, 91cm diameter coils in a Helmholtz configuration. We measured the magnetic coupling with the field oriented along the x and y axes of the apparatus. In both orientations we made measurements without the external magnetic shield (run7246 and run7329) and found the pendulum dipole coupling to be $(1.02 \pm 0.11) \times 10^6$ fNm/T.

After collecting the science data, we removed the pendulum and placed the AMR probe in the location of the pendulum test-mass to measure the x-direction magnetic field noise over the course of several hours (run7401). We found the sinusoidal oscillation of the field in our signal frequencies to be 0.001 ± 0.002 mGauss. This oscillating field would lead to a systematic torque of at most $\widehat{\sigma} = 0.0017$ fNm, where we have included a factor of $5.6\times$ from the shielding of the inner mu-metal shield. This systematic torque is negligible in comparison to the science data torque measurement errors.

10.2 Electrostatic Torques

10.2.1 Foil Displacement

Suppose there were a bias voltage between the pendulum and screen or attractor and screen. If the pendulum or attractor platinum wedges and glue-filled gaps were at slightly different separations or if they had different potentials, for example due to a contact potential difference, then the wedges would pull with different forces vertically on the foil causing raised and lowered ridges. This deformation of the screen could couple the attractor and pendulum electrostatically. This electrical force must fight against the tension in the foil to create a

Bessel function drumhead mode of order (18,1), (54,1), or (120,1) where the 1 indicates the lowest mode with the given spatial frequency.

The frequency of a given drumhead mode is

$$f_{m,n} = \frac{1}{2\pi}\sqrt{\frac{T\alpha_{m,n}^2}{\rho h a^2}} = \frac{1}{2\pi}\sqrt{\frac{K_{m,n}}{M}}$$

where T is the tension, $\alpha_{m,n}$ is the n^{th} zero of the m^{th}-order Bessel function, ρ is the density of the screen, and ρ, h, and a are the density, thickness, and radius of the screen, [40]. We related this to a spring constant for an average displacement in each mode where $K_{m,n}$ is the spring constant and $M = \pi\rho h a^2$ is the mass of the screen. A measurement of the spring constant for the lowest (0,1) mode would allow us to compute the spring constant for any other mode,

$$K_{m,n} = K_{0,1}\left(\frac{\alpha_{m,n}}{\alpha_{0,1}}\right)^2$$

$$\alpha_{0,1} = 2.4048, \quad \alpha_{18,1} = 23.2568, \quad \alpha_{54,1} = 61.2875, \quad \alpha_{120,1} = 129.3628$$

We determined $K_{0,1}$ by measuring the attractor-screen capacitance as a function of applied DC bias voltage. The minimum of the capacitance determined the contact potential bias voltage, $V_{attr} = (-301 \pm 17)$ mV. The capacitance measurements were converted to separations using an attractor z-scan and we computed the electrostatic force with the derivative of the capacitance model with respect to separation and the known applied voltages, $F = \frac{1}{2}\frac{\partial C}{\partial z}(\Delta V)^2$. The spring constant was determined by fitting the screen displacement as a linear function of electrostatic force, $F = K_{0,1}\Delta z$, see figure 10.5.

The resulting $K_{0,1}$, (10075 ± 162) N m^{-1}, gave the spring constants of the 18-, 54- and 120-fold drumhead modes as $K_{18,1} = 9.4 \times 10^5$ N m^{-1}, $K_{54,1} = 6.5 \times 10^6$ N m^{-1}, and $K_{120,1} = 2.9 \times 10^7$ N m^{-1}.

We additionally tested for the dependence of a potential bias voltage on the attractor by applying a $\pm$3V bias between attractor and screen using two AA batteries through a

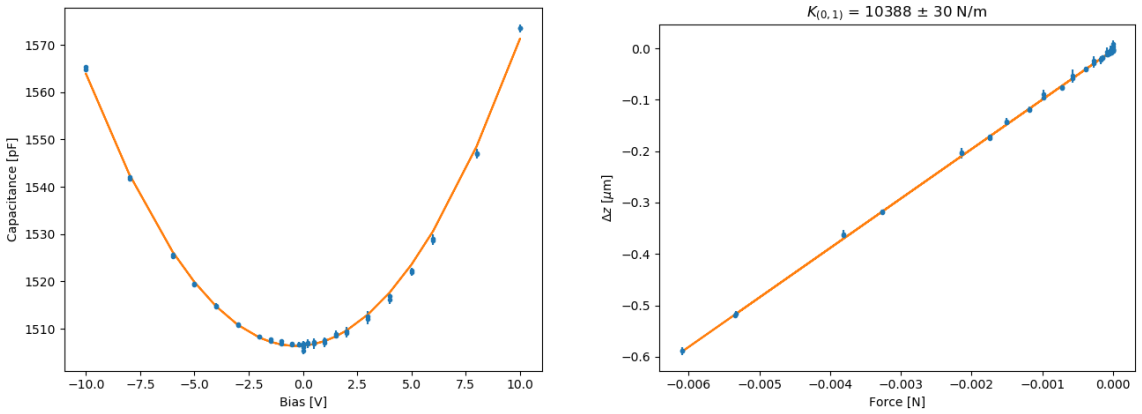

Figure 10.5: **Attractor Contact Potential and Screen Tension** - The attractor-screen contact potential was measured by applying a bias voltage through the Stanford LCR meter and measuring the change in capacitance. The contact potential appears at the minimum of the parabola, $V_{attr} = (-301 \pm 17)$ mV. The change in capacitance is converted to a displacement of the screen and used to estimate the screen spring constant and tension.

1MΩ resistor. The exaggeration factor was $f_{bias}^{\pm} = \left(\frac{3\mp.301}{-.301}\right)^2$, depending on the sign of the applied bias. The spurious torque was proportional to $(\Delta V)^2$ and so we averaged the effect of the ±3V configurations. The resulting torques were less than 1 aNm in every harmonic, see table 10.1.

10.2.2 Separation-dependent changes

Previous iterations of this experiment [31][19] showed that the pendulum's equilibrium angle and free-torsional oscillation frequency depended on its separation from the screen. This was ascribed to an electrostatic coupling between "patch" fields on the pendulum test-mass and the screen. We measured the pendulum equilibrium angle and period as a function of separation to the screen at the beginning and end of the data-set.

We modeled this behavior by assuming that the pendulum torsion spring constant had

harmonic	V_{attr}=+3V	V_{attr}=−3V	V_{attr}=0V	$N_{bias} \pm \sigma_{N,bias}$	$\widehat{\sigma}$
120	1.498±.014	1.499±.013	1.498±.013	.0000 ± .0004	.0004
18	1.072±.010	1.057±.009	1.056±.007	.0002 ± .0003	.0005
54	.119±.005	.119±.005	.125±.004	−.0001 ± .0001	.0003

Table 10.1: **Attractor Bias Potential Torque** - We applied a bias voltage of ±3V (run7359, run7361) between the attractor and screen, and observed the change in torque amplitude relative to runs at the same pendulum-screen separation (run6962, run7326, and run7363). The average of the runs with applied bias were used to compute the systematic. All units are in fNm.

two components, the usual contribution for the suspension fiber and an additional electrostatic spring with a separation-dependent spring constant. Assuming the pendulum is a harmonic oscillator with a spring constant from the fiber suspension, κ_f, centered at θ_f and an electrostatic spring with pendulum-screen separation, z_p, dependent spring constant, κ_e, centered at θ_e, so that its energy is

$$U(\theta, z_p) = \frac{1}{2}\kappa_f(\theta - \theta_f)^2 + \frac{1}{2}\kappa_e(z_p)(\theta - \theta_e)^2$$

The equilibrium angle is then given by the following:

$$\theta_{eq} = \frac{\kappa_e(z_p)\theta_e}{\kappa_f + \kappa_e(z_p)} + \frac{\kappa_f\theta_f}{\kappa_f + \kappa_e(z_p)} = \frac{\theta_e}{1 + \frac{\kappa_f}{\kappa_e(z_p)}} + \frac{\theta_f}{1 + \frac{\kappa_e(z_p)}{\kappa_f}}$$

The free torsional oscillation frequency is given by:

$$\omega_0(z_p) = \sqrt{\frac{\kappa_f + \kappa_e(z_p)}{I_z}} = \omega_{0,f}\sqrt{1 + \frac{\kappa_e(z_p)}{\kappa_f}}$$

where $\omega_{0,f} = \sqrt{\kappa_f/I_z}$ is the free torsional frequency of the pendulum due only to the fiber without electrostatic interations to the screen. There are a couple of likely origins for the electrostatic spring constant. If the electrostatic force were due to a potential between the

pendulum test-mass and the electrostatic screen, we could model the spring constant as the inverse-square of the separation. If the force were due to a collection of patch fields, we might have expected to see an inverse-fourth power of separation [28].

A systematic torque error could occur in two ways. A change in z_p between the data run and sweep run would result in an error of the measurement of ω_0 used to convert twist angle measurements to torque. Additionally, any modulation of z_p at a signal frequency, could induce a torque through the changing electrostatic spring constant.

$\theta_{eq}(z_p)$, $\omega_0(z_p)$ Measurements

We performed five measurements of equilibrium angle, θ_{eq}, and pendulum free-torsional oscillation frequency, ω_0, as a function of z_p similar to the z-scans performed to determine separations. We started the pendulum at a far separation, $z_p \approx 3$mm. We then logarithmically stepped the pendulum closer while recording pendulum twist-angle, pendulum-screen capacitance, and z dial-indicator value. The steps were made every 2.5 pendulum oscillations. This allowed us to fit the equilibrium angle without much dependence on the twist angle amplitude and it tended to not drive up the twist angle amplitude too much.

The data were fit for θ_{eq} and ω_0 simultaneously with a nonlinear fit at each dial-indicator position. We also found the average capacitance at each dial-indicator position, which allowed us to also treat these measurements as a z-scan. The change in pendulum position tilted the pendulum support, so we fit for a linear coupling in θ_{eq} to the two AGI values to remove this effect. All five measurements are shown in figure 10.6.

The equilibrium angle dependence on pendulum-screen separation was not characterized by a simple power-law, and so we interpolated each of the scans with third-order splines, $\widehat{\theta_{eq}}(z_p)$ and $\widehat{\omega_0}(z_p)$. Each data run was associated with the scan closest in time corresponding to the same apparatus configuration. The different configurations were a tilt of the apparatus after run6302 and the removal/reattachment of the ion pump after run6787. To assess an error on the scan interpolations, we observe the scatter between run6971, run6986, and run6995 which were all taken within eight days of each other and in the same configuration.

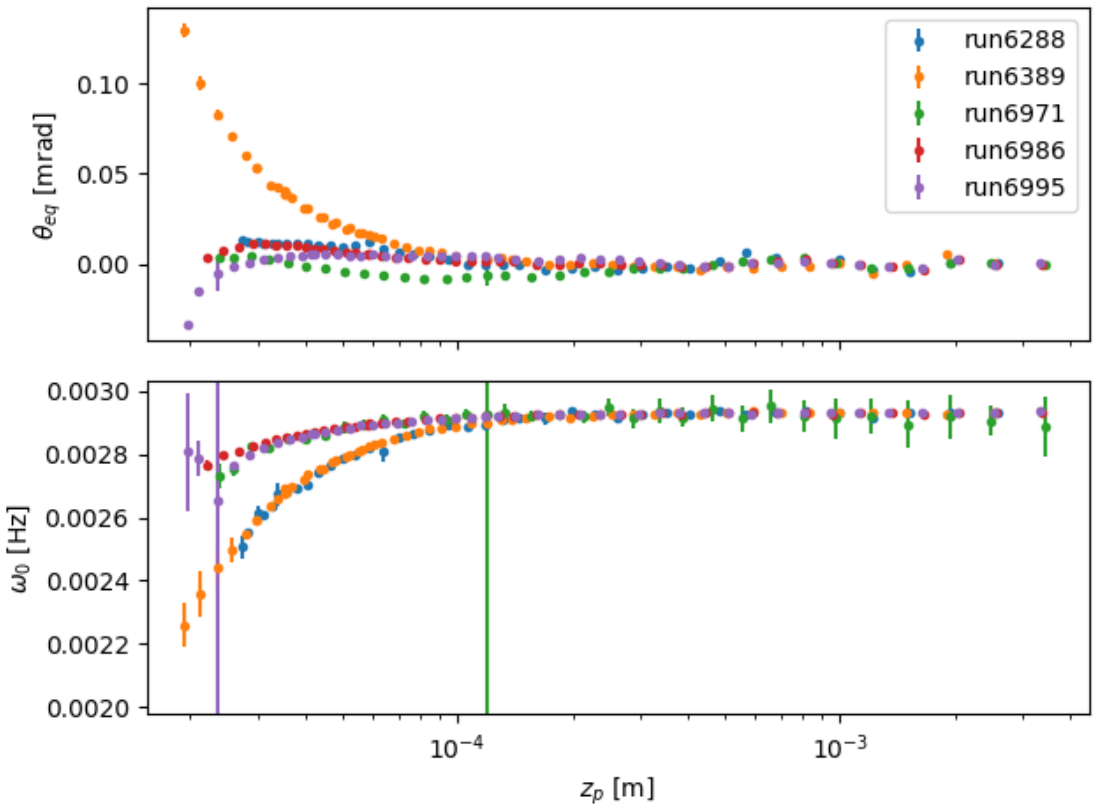

Figure 10.6: **Equilibrium angle and torsional oscillation frequency dependence on z_p** - We performed five measurements of equilibrium angle and pendulum free torsional-oscillation frequency as a function of pendulum-screen separation z_p throughout the dataset. Differences in the the scans can be attributed to changes of the apparatus. The apparatus tilt was changed between run6288 and run6389. The ion pump failed between run6389 and run6971 and was removed and then re-attached. The final three scans were all taken within eight days of each other (run6971, run6986, and run6995).

We used the scatter of points evaluated with these interpolations to assess the error.

We used sweep runs to calibrate out non-linearities of the autocollimator angle readout system as well as to measure the pendulum free-torsional frequency ω_0 at a given z_p for each data run. A fit to twist-angle of a given turntable harmonic $\theta^m(\omega)$ is converted to torque using this frequency measurement as follows (a more detailed description can be found in Chapter 7):

$$N^m(\omega) = I\omega_0^2 \left(1 - \left(\frac{\omega}{\omega_0}\right)^2 + \frac{i}{Q}\right) \theta^m(\omega).$$

If the pendulum-screen separation changes between the sweep run and data run, ω_0 will change slightly. We estimated this effect with our interpolation function, $\Delta\omega_0 = \frac{\partial\widehat{\omega_0}(z_p)}{\partial z_p}\Delta z_p$. This leads to a multiplicative systematic effect of

$$N^m(\omega) \approx \left(1 + \frac{2\Delta\omega}{\omega_0(z_p)}\right) N^m(\omega_0).$$

The largest difference in z_p between sweep and data runs was 18μm but at a large distance and the average difference in z_p was less than 1μm. The average systematic effect is about 0.01% and at most 0.1% and therefore much less than the calibration uncertainty.

z_p modulation

A systematic torque would appear from any modulation of the pendulum-screen separation through the electrostatic interaction to the screen in phase with the attractor rotation. We fit the pendulum-screen capacitance data over the whole dataset for a modulation in the capacitance δc^m at the signal frequencies of $m = 18\omega, 54\omega$, and 120ω as a function of turntable angle. These fits were converted to a separation modulation $\delta z^m = \frac{z_p}{\overline{C}}\delta c^m$, where $\overline{C}$ was the average pendulum-screen capacitance in the the data run. The z_p modulations of each harmonic averaged over the whole dataset are given in table 10.2.

We treated the change in equilibrium angle in our measurements as a static torque so that for a given separation modulation δz^m, a systematic torque was given as

harmonic	$\delta z_{\cos}$ [nm]	$\delta z_{\sin}$ [nm]
18ω	$.50 \pm .12$	$-.02 \pm .16$
54ω	$-.51 \pm .07$	$.10 \pm .09$
120ω	$.91 \pm .07$	$-1.61 \pm .09$

Table 10.2: **Average vertical modulation of pendulum-screen separation at signal frequencies** - We searched for any vertical modulation of pendulum-screen separation due to the attractor rotation at the signal harmonics. We averaged the results from each run.

$$N^m = I\omega_0^2 \frac{\partial \widehat{\theta_{eq}}}{\partial z_p} \delta z^m$$

The largest effect was about (0.018±0.001)fNm in the 120ω signal at a data run associated to the scan during run6389 and at a close separation, but the average effect was 0.002fNm. We subtracted these systematic torques from the appropriate phases and harmonics and included their error in quadrature.

10.3 Parameter error

10.3.1 z_0 error

We found a calibration discrepancy in the Stanford SR720 LCR meter used for our capacitance measurements while in the pF range and driven at 100kHz. We measured the capacitance of between one and ten (100 ± 1)pF capacitors in parallel at the leads typically connected to the attractor and screen (run7404). We fit the capacitance measurements to a line and found the slope to be 4% percent larger than expected which was independent of the offset capacitance in the leads. In the nF range, the LCR meter gave consistent values for two and three (470 ± 4.7)pF capacitors in parallel. This systematic effect was larger when driven at higher frequencies and suggestive of inductance in the circuit.

This calibration discrepancy largely did not affect the fits for z_0 in our z-scans as the

location of the pole is independent of the overall scale factor. Only one pendulum z-scan entered the nF range of the LCR meter and so there was no systematic associated with the pendulum z_0. We found the corrected attractor scans gave a systematic effect of less than 0.5μm, in agreement with intuition.

The z_0 errors associated with slow drifts between the 15 z-scans were corrected by fitting the pendulum z_0 values as linear functions of time, see section 5.7.6.

10.3.2 Radial centering and ϕ-top runout

The pendulum was suspended from a set of three translation stages and a rotation stage. A rotation of the upper stage can lead to a horizontal translation of the pendulum if the suspension point is horizontally misplaced from the rotation axis, which we call runout. We measured the runout of our fiber suspension to be $\approx (1 \pm .5)$mm. Due to thermal drifts of the fiber and apparatus (typically $\sim .2\mu$rad/hr), the equilibrium angle of the pendulum mirror changed with respect to the autocollimator and was rotated to realign the two. With a runout r_0 and a total equilibrium angle change of $\Delta\phi$, the radial positioning error is $\Delta r = r_0\sqrt{\sin^2(\Delta\phi) + (1-\cos(\Delta\phi))^2}$. We tracked the rotation stage position for each data run and found the total equilibrium angle change was $\Delta\phi = (0.24 \pm 0.02)$mrad. The radial positioning error was therefore $\Delta r = (0.2 \pm 0.1)\mu$m, much smaller than the uncertainty in the radially centered position.

10.4 Thermal Coupling to Twist Angle

We relied on a water-bath chiller to control the air temperature of the thermal enclosure surrounding the apparatus. Similarly, the temperature of the motor that turned the attractor was locked with a water-cooled Peltier element. The steady temperature environment maintained the alignment and stability of many apparatus components throughout the entire data taking campaign and during the course of each data run. However, a temperature modulation fixed in phase to the attractor rotation and at one of the signal frequencies could cause an apparent change in twist angle through deformation of the apparatus or the optical

path.

We measured the dependence of the twist angle on the thermal enclosure temperature by sinusoidally driving the chiller bath temperature at the 18ω frequency by $\pm$350mK without the attractor rotating (run7159). We expected any modulation at a higher frequency to be substantially attenuated by the large heat capacity of the apparatus and therefore to be much less than the coupling at the 18ω frequency. A temperature sensor attached to the autocollimator served as a proxy for the apparatus as a whole, and experienced a temperature change of $T_{app} \pm \sigma_{T,app} = 1.253 \pm .035$ mK in amplitude of sinusoidal variation at 18ω. This modulation caused an apparent sinusoidal twist of the pendulum at the same 18ω frequency, interpreted as a torque amplitude of $N_{18} \pm \sigma_{N,18} = 0.133 \pm 0.008$ fNm. We used the ratio of measured torque amplitude to apparatus temperature amplitude as the coupling coefficient of torque to apparatus temperature, $C_{T,app} = \frac{N_{18}}{T_{app}} = 0.106$ fNm/mK, and the phase delay was 1.22°.

We fitted each data run for the sinusoidal temperature variation in phase with the attractor rotation of the autocollimator temperature at 18ω and averaged each component over the entire dataset. We then calculated the contribution to each of the measured torque components using $C_{T,app}$. The average autocollimator temperature variations at 18ω were -0.96 ± 3.60 μK and 0.85 ± 3.99 μK in the cosine and sine components, respectively. We calculated the systematic torque in the same harmonic components using the coupling coefficient and rotating by the phase delay. The resulting systematic torques, given in table 10.3, were less than 1aNm, which was completely negligible in comparison to the science data torque measurement errors.

We similarly modulated the temperature of the attractor motor, driving the Peltier element sinusoidally at the 18ω frequency without the attractor rotating (run7202). We again expected any modulation at a higher frequency to be attenuated by the heat capacity of the turntable and therefore to be much less than the coupling at the 18ω frequency. This induced an 18ω sinusoidal variation in the temperature of the base plate supporting the turntable with an amplitude of $T_{motor} \pm \sigma_{T,motor} = 0.164 \pm 0.013$ mK and caused an apparent torque of

harmonic	$T \pm \sigma_T$ [μK]	$\widehat{\sigma}_{app}$ [aNm]
18c	-0.96±3.60	0.52
18s	0.85±3.99	0.47

Table 10.3: **Systematic torque bounds on modulated apparatus temperature at** 18ω - We bounded the systematic torques from modulation of the apparatus temperature at the 18^{th} harmonic of the attractor rotation. Higher harmonics were attenuated by the apparatus heat capacity. Here c and s denote the *cosine* and *sine* components relative the attractor rotation. Systematic torques at higher frequency from temperature variation were attenuated by the apparatus heat capacity.

$N_{18} \pm \sigma_{N,18} = 0.0096 \pm 0.0071$ fNm at 18ω. Again, we used the apparent coupling coefficient $C_{T,motor} = \frac{N_{18}}{T_{motor}} = 0.058$ fNm/mK, phase delay of 8.44°, and the modulated temperature in the base plate averaged over the whole dataset to derive the systematic torque. The base plate temperature variation at the 18ω over the entire dataset was $T_{18c} \pm \sigma_{T,18c} = -0.28 \pm 0.78$ μK and $T_{18s} \pm \sigma_{T,18s} = -0.16 \pm 0.81$ μK in the cosine and sine components, respectively. We calculated the systematic torque in the same harmonic components using the coupling coefficient and rotating by the phase delay. The bounds on systematic torques were close to 1aNm, which were negligible in comparison to the science data torque measurement errors.

10.5 Gravitational Torques

There were two potential gravitational sources of systematic error. The first were calibration errors, which were already accounted for in Chapter 8. The second were from other portions of the pendulum or attractor aside from the test-masses interacting at the 18ω and 120ω frequencies. Since the pendulum and attractor have some components with 6-fold symmetry we might expect to see coupling to the 18-fold or 120-fold patterns of the test-masses. The largest effect should occur at 18ω which could arise in three ways. First, the 6-fold screws

harmonic	$T \pm \sigma_T$ [μK]	$\widehat{\sigma}_{motor}$ [aNm]
18c	-0.28±0.78	0.66
18s	-0.16±0.81	1.15

Table 10.4: **Systematic torque bounds on modulated motor temperature at** 18ω - We bounded the systematic torques from modulation of the motor temperature at the 18^{th} harmonic of the attractor rotation. Higher harmonics were attenuated by the apparatus heat capacity. Here *c* and *s* denote the *cosine* and *sine* components relative the attractor rotation. Systematic torques at higher frequency from temperature variation were attenuated by the apparatus heat capacity.

on the tip-tilt stage of the attractor interact with the 6-fold holes that position the inner calibration spheres on the pendulum creating a 6ω torque and harmonic at 18ω. Second, the 6-fold screws interact directly with the 18-fold pattern of the pendulum test-mass. Finally, the 6-fold holes of the pendulum interact with the 18-fold pattern of the attractor test-mass. We estimated all of these couplings with `FBESSELN` and find the 18ω torques to be 4×10^{-19} fNm, 9×10^{-8} fNm, and 3×10^{-18} fNm respectively at the closest separations which are completely negligible.

Chapter 11

ANALYSIS

The fitting procedure was similar to those used in previous iterations of our ISL tests [19][36][31]. We minimized χ^2 cost functions for purely Newtonian torques or Newtonian + Yukawa torques over a range of length scales λ from 5μm to 9mm with freely varying α.

11.1 Torque Measurements

We collected science torque data from August 2018 through February 2019 for a total of 95 data runs. The face-to-face test-mass separation s ranged between 3mm and 52μm. The complete list of runs can be found in Appendix A. We found the single phase that placed all signal components in-phase with a Newtonian or Yukawa torque and subtracted systematic torques (see Chapter 10). The corrected in-phase data are plotted in figure 11.1.

11.1.1 Phase Alignment

Throughout the experiment, whenever the turntable was at the index-mark, the relative angular orientation of the test-mass patterns was always the same. However, this fixed angle was difficult to measure directly since it depended on the orientation of the attractor test-mass to the index mark and the pendulum test-mass to the mirror.

The constant angular orientation also left the phase of each measured torque signal constant. In our analysis (see Chapter 7), we fit each data run for $m\omega$ torques (m = 18, 54, 120) as a combination of cosine and sine amplitudes (C_m, S_m) as functions of turntable angle relative to the index mark ϕ. We converted from cosine and sine amplitudes to an amplitude and phase (A_m, ϕ_m) defined by

$$N_m(\phi) = C_m \cos(m\phi) + S_m \sin(m\phi) = A_m \sin(m(\phi - \phi_m)),$$

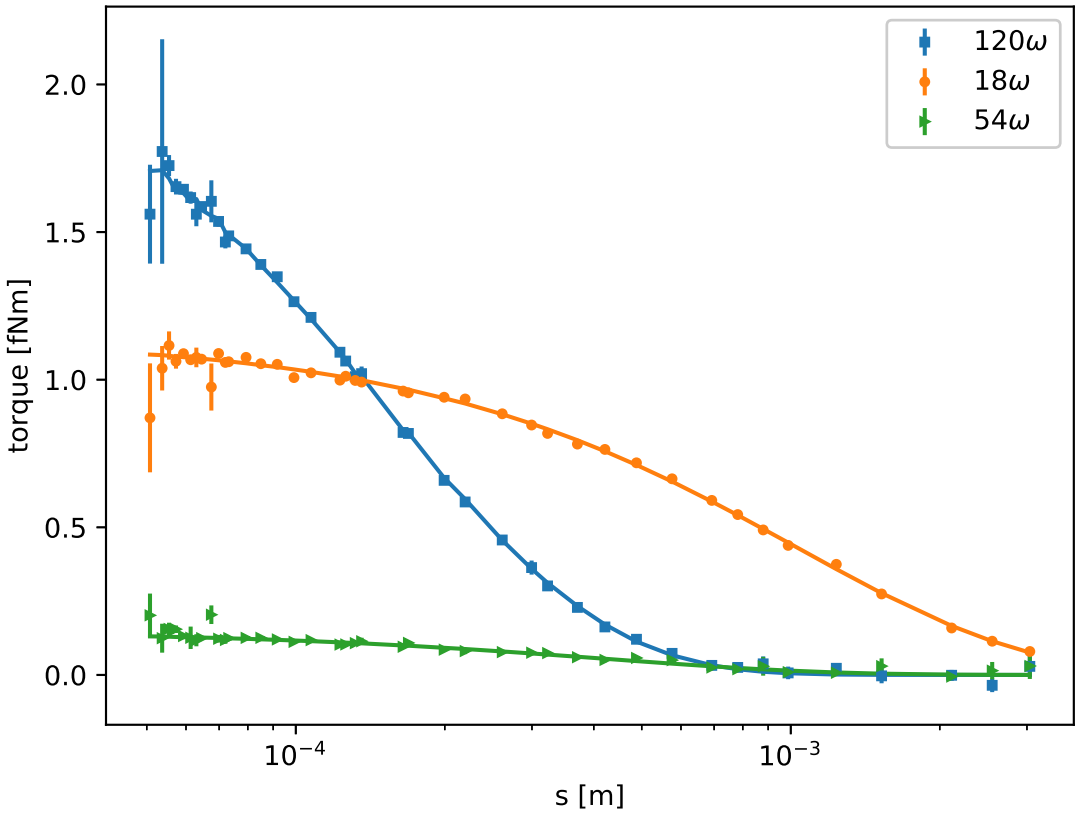

Figure 11.1: **Binned in-phase torque data** - The $120, 18$, and 54ω torque data has been binned into 2μm sized bins on the total face-to-face test-mass separation, s.

The phase ϕ_m was determined modulo $\frac{360^\circ}{m}$ and defined a turntable angle at which there was no $m\omega$ torque. We found the constant best-fit phase for each torque signal $\overline{\phi_m}$ using a weighted circular average over the fit phase for each run $\phi_{m,j}$,

$$\overline{\phi_m} = \frac{1}{m}\text{atan2}\left(\frac{1}{W}\sum_j W_j \sin m\phi_{m,j},\ \frac{1}{W}\sum_j W_j \cos m\phi_{m,j}\right),$$

where the weights were the inverse-square of the phase errors for each run, $W_j = 1/\sigma^2_{\phi_{m,j}}$ and $W = \sum_j W_j$ was the sum of the weights. This method was independent of the torque

amplitude at different s and handled runs where the phase was poorly determined within $\frac{360^\circ}{m}$.

Since the test-mass patterns were identical, there were no Newtonian or Yukawa torques in any harmonic at the turntable angle where the patterns directly overlay one another, $\phi = \phi_0$. The measurements of best-fit phase for each torque signal were then related to this single phase as

$$\overline{\phi_m} = \phi_0 \bmod \frac{360^\circ}{m}.$$

However, the 6-fold symmetry of the test-mass pattern limited any determination of ϕ_0 to within 60°. We determined ϕ_0 by iterating through the possible angles allowed by the best-fit phase for each harmonic to find a value consistent with each. That is, within a 60° segment there was a unique p and q such that

$$\phi_0 = \overline{\phi_{120}} + (3p)^\circ, \quad \text{for some } p \in [0, 1, 2, ..., 19]$$
$$\phi_0 = \overline{\phi_{18}} + (20q)^\circ, \quad \text{for some } q \in [0, 1, 2]$$

We averaged the consistent estimates of ϕ_0 weighted by the inverse-square errors. The best-fit phases for the 18, 54, and 120ω torques along with ϕ_0 are given in table 11.1. Since ϕ_0 was determined so well, we restricted our analysis to only the data components in-phase with the expected Newtonian or Yukawa signals.

	Phase [degrees]
ϕ_{120}	51.77131 ± 0.00079
ϕ_{18}	51.77225 ± 0.00380
ϕ_{54}	51.79217 ± 0.01040
ϕ_0	51.77146 ± 0.00077

Table 11.1: Preferred phase for each torque harmonic m and angular orientation of test-masses ϕ_0. Each phase has been rotated by an integer multiple of $\frac{360^\circ}{m}$ to place into the same approximate phase.

11.2 Torque Model and Parameters

The Newtonian and Yukawa torque models were based on the cylindrically-symmetric Fourier-Bessel calculations with corrections for angular and radial misalignments, geometry and metrology errors, and a calibration uncertainty. All of these parameters were determined through separate measurements, but many were allowed to float in the fit.

11.2.1 Fourier-Bessel Tables

Although we had an analytic formula for computing the torques of our geometry, re-evaluating the integral at each step of the fitting routine became computationally expensive. To save on computation time, we created a table of Fourier-Bessel torques over a range of separations spanning the range tested by experiment and for a reduced set of parameters. Each analytic Newtonian or Yukawa calculation was a function of 11 parameters for each $m\omega$ torque: the separation (s), the attractor and pendulum test-mass wedge thicknesses (t_a, t_p), the inner and outer radii ($r_{i,a}, r_{o,a}, r_{i,p}, r_{o,p}$), the subtended angle of the wedges (β_a, β_p), and the platinum and glue densities (ρ_{Pt}, ρ_g).

The subtended angle and inner and outer radii were all measured with the Smartscope and had an uncertainty due to the ability to locate the edge of the patterns. Gravity only cares about the average location of the masses in the wedges, but our optical edge tracing method could not see any craters in the edge surface roughness, only protruding burrs. We simplified the model to consist of the single "overcut" parameter, ϵ, that accounted for the roughness of every platinum surfaces cut by the EDM. This was defined such that a positive ϵ increased the area of the wedges equally in all directions, see figure 11.2. The inner and outer radii and subtended angles were adjusted as follows

$$
\begin{aligned}
r_i &\to r_i - \epsilon \\
r_o &\to r_o + \epsilon \\
\beta &\to \beta + 2\tan^{-1}\left(\frac{2\epsilon}{r_i + r_o}\right)
\end{aligned}
$$

The thicknesses were determined as described in section 4.1. We left each test-mass pattern thickness as a separate parameter. Adjustments of the overcut and thickness parameters also changed the estimated volume of the removed wedges.

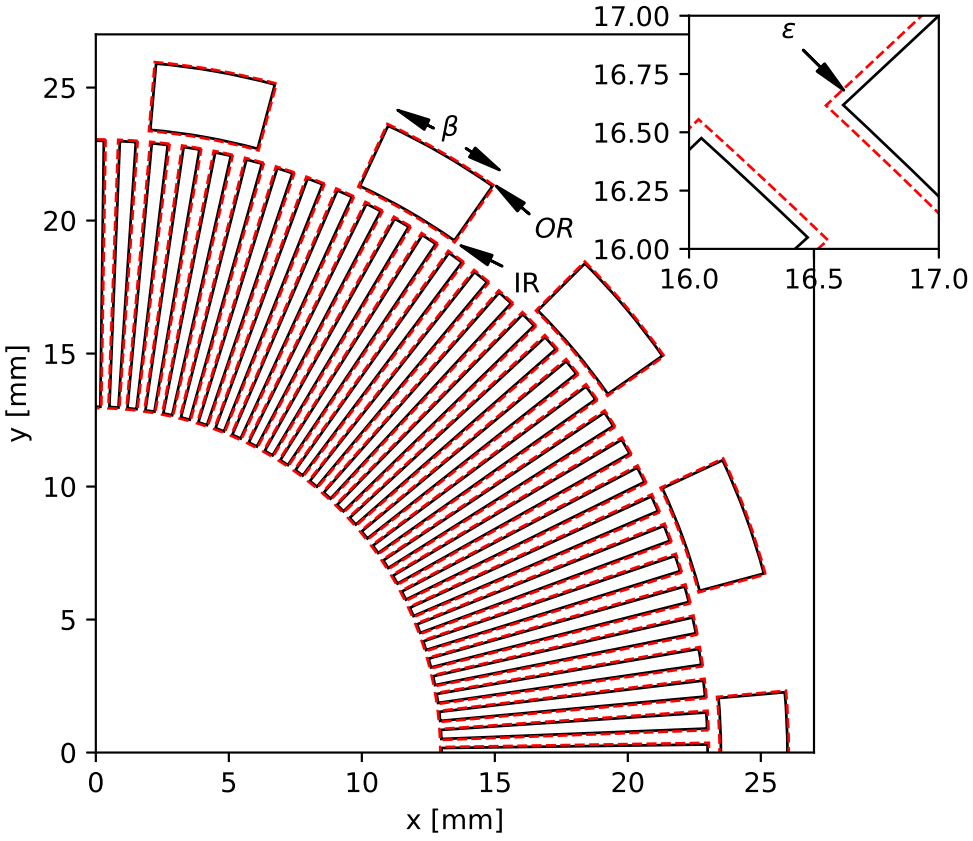

Figure 11.2: **Geometric parameters of the wedge patterns** - The subtended angle, β, and the inner and outer radii were computed at nominal values and adjusted with the overcut parameter, ϵ.

The torque calculations depended linearly on the density contrast for the evenly filled wedges. We had an explicit measurement of the glue density (ρ_g) which we left as a free parameter in our model. However, we could only infer the platinum density from measure-

ments of the mass loss ($m_{a,m}, m_{p,m}$) and volume of the platinum wedges. We effectively fixed the mass loss for each pattern in our torque tables and scaled the resulting torques as we adjusted the mass parameters in our fit.

We calculated tables of $m\omega$ Fourier-Bessel torques over a set of separations spanning the range tested by experiment with a reduced set of four floating parameters for each $m-$fold pattern ($t_{a,m}, t_{p,m}, \rho_g, \epsilon$). The 18-fold pattern thicknesses ($t_{a,18}, t_{p,18}$) were shared between the 18 and 54ω torque calculations, and the glue density and overcut were shared in all torque calculations. We computed the torques at high and low values of each parameter to account for uncertainty in the measured values for a total of 2^4 calculations for each separation.

In the fitting procedure, we used a third-order spline interpolation to asses the torque at a given separation for each combination of fit parameters ($t_{a,m}, t_{p,m}, \rho_g, \epsilon$). We then used a multilinear interpolation to find the torque associated to the best-fit values of each of the four parameters at that separation. We scaled the interpolated torque to match adjustments of the mass parameters ($m_{a,m}, m_{p,m}$).

11.2.2 Radial Misalignment Correction

We corrected for the effect of radial misalignments of both the attractor and pendulum test-mass from the turntable rotation axis (r_a and r_j, respectively) using an empirical function derived from Monte-Carlo calculations of torque radial dependence, see Chapter 2. The Monte-Carlo calculations were computed for each harmonic at various separations, radial offsets, and for various λ including Newtonian gravity. Measurements of the horizontal location of the 120ω torque maximum determined the position of the attractor rotation axis (x_0, y_0), and the pendulum position (x_j, y_j) was recorded for each data run. The radial misalignment of the attractor test-mass was found with the Smartscope. The two contributions did not add as one displacement since the direction of the attractor test-mass displacement changed with the turntable rotation which we correct for with a second order correction of the empirical function, see Appendix B.

11.2.3 Tilt Correction

We corrected for tilts of the attractor and pendulum test-masses relative to the rotation axis by including a second-order effect from the root-mean-square (RMS) separation. The attractor tilt Ψ_A changed with the turntable rotation (this is the same attractor tilt angle denoted as $\widetilde{\Psi}_A$ in Chapter 5). To account for the stationary tilt of the pendulum test-mass relative to the rotation axis, we combined the screen tilt with the deviation of the apparatus tilt from vertical for each run j ($\widetilde{\Psi}_S$ and $\widetilde{\Psi}_{V,j}$, respectively). The contribution of the pendulum test-mass tilt was unnecessary since the apparatus vertical was measured relative to the pendulum test-mass face. For simplicity we denote the stationary tilt as Ψ_P. The tilt corrections contributed separately, see Appendix B.

11.2.4 Torque Model

The final contribution to the full predicted torque model was a scale factor γ which accounted for the autocollimator calibration. This factor was determined by measurements with the external calibration turntable, see Chapter 8. The Newtonian ($\lambda = \infty$) and Yukawa torque models were given by

$$\widetilde{N}_m(\vec{\zeta}_j, \vec{\eta}, \lambda) = \overbrace{\gamma}^{\text{Cal. scale}} \overbrace{\left(\frac{m_p}{t_p A_p \rho_{nom}}\right)\left(\frac{m_a}{t_a A_a \rho_{nom}}\right)}^{\text{fit density correction}} \overbrace{R_m(r_j, r_a, s_j, \lambda)}^{\text{Radial misalignment}} \times$$
$$\Bigg[\underbrace{\overline{N}_m(s_j, t_p, t_a, \rho_g, \epsilon, \lambda)}_{\text{Fourier-Bessel Torque}} + \underbrace{\frac{1}{2}(\Delta s_m^2(\Psi_A) + \Delta s_m^2(\Psi_P))\frac{d^2\overline{N}_m(s_j, t_p, t_a, \rho_g, \epsilon, \lambda)}{ds_j^2}}_{\text{2nd Order RMS separation correction}}\Bigg]$$

The complete set of 17 model parameters were defined as:

- $m_{p,120}$, $m_{p,18}$, $m_{a,120}$, $m_{a,18}$: The missing mass from the pendulum and attractor 18- and 120-fold patterns
- $t_{p,120}$, $t_{p,18}$, $t_{a,120}$, $t_{a,18}$: The thickness of the pendulum and attractor 18- and 120-fold wedges
- x_0, y_0: The horizontal location of the attractor turntable rotation axis as measured with the dial indicators of the pendulum translation stages. This location was determined

by maximizing the 120ω torque at a constant separation. The pendulum dial indicator positions were recorded for each data run $[x_j, y_j, z_j]$ so the radial misalignment of the pendulum is $r_j = \sqrt{(x_j - x_0)^2 + (y_j - y_0)^2}$.

- s_0: Contribution to the total separation from the screen and epoxy film thickness, so the total separation for a given run is, $s_j = z_{p,j} + z_a + s_0$. The dial indicator position z_j and pendulum-screen capacitance C_j for each run determine the pendulum separation to the screen $z_{p,j}(z_j, C_j)$. The attractor-screen position z_a was determined via screen actuator position and attractor-screen capacitance. The addition of the s_0 parameter accounts for the thickness of the epoxy uniformly coating each test-mass along with the screen thickness determined by touch-probe measurements.
- ρ_g: Density of the Stycast 1266 epoxy with Loctite Catalyst 23LV hardener that fills the gaps in the platinum wedges. Our mistaken use of the wrong hardener required us to make a separate measurement of the epoxy density.
- Ψ_a: The tilt angle of the attractor test-mass with respect to the turntable rotation axis
- Ψ_p: The tilt angle of the pendulum test-mass with respect to the turntable rotation axis
- ϵ: The overcut parameter accounting for an uncertainty in the determination of the radial and angular dimensions of the test-mass patterns
- r_a: The radial misalignment (runout) of the attractor 120-fold pattern relative to the turntable axis of rotation
- γ: The overall scale factor determined from the gravititational torque calibration accounting for autocollimator calibration uncertainty

11.3 Newtonian Fit

We fit the torque model by minimizing the χ^2 function defined identically to previous iterations of our ISL test, [36] [19], given below

$$\chi^2 = \sum_j \sum_m \left[\frac{N_m(\vec{\zeta_j}) - \widetilde{N}_m(\vec{\zeta_j}, \vec{\eta}, \lambda)}{\sqrt{\delta N_m^2 + \delta z_{p,j}^2 \left(\frac{d\widetilde{N}_m}{ds_j}\right)^2}} \right]^2 + \sum_i \left[\frac{\eta_i^{exp} - \eta_i}{\delta \eta_i^{exp}} \right]^2 \tag{11.1}$$

where the first term is a sum over each data run with measurements of position $\vec{\zeta_j} = (x_j, y_j, z_{p,j})$ including the square-error contribution from each torque component $N_m(\vec{\zeta_j})$ ($m = 120\omega$, 18ω, 54ω) relative to the torque model prediction. We accounted for both the torque measurement error and the dependence of the model prediction on the measured pendulum position, which almost entirely came from the separation uncertainty. We also included a contribution of the square-error for each fit parameter η_i relative to the experimentally measured value η_i^{exp} scaled by the measurement error $\delta\eta_i^{exp}$. This forced the fit parameters to simultaneously match the torque data and parameter measurements.

We began by fitting the purely Newtonian model ($\widetilde{N}_m(\vec{\zeta_j}, \vec{\eta}, \infty)$) with the complete set of model parameters allowed to float and found that only a small subset of five parameters contributed significantly to χ^2, see table 11.3. We then performed a simpler fit with only x_0, y_0, s_0, ϵ and γ varying and the remaining parameters fixed by their measurements, see table 11.3.

Parameter	Measured	Fit	Units	χ^2
x_0	-0.130 ± 0.004	-0.129 ± 0.003	mm	0.10
y_0	-2.138 ± 0.003	-2.136 ± 0.003	mm	0.48
s_0	13.1 ± 1.4	14.1 ± 0.8	μm	0.48
$m_{A,120}$	1.19856 ± 0.00013	1.19856 ± 0.00013	mg	0.00
$m_{A,18}$	0.40955 ± 0.00010	0.40955 ± 0.00010	mg	0.00
$m_{P,120}$	0.65749 ± 0.00013	0.65749 ± 0.00013	mg	0.00
$m_{P,18}$	0.22402 ± 0.00008	0.22402 ± 0.00008	mg	0.00
$t_{A,120}$	98.58 ± 0.70	98.69 ± 0.67	μm	0.03
$t_{A,19}$	98.62 ± 0.64	98.61 ± 0.64	μm	0.00
$t_{P,120}$	54.33 ± 0.49	54.39 ± 0.48	μm	0.02
$t_{P,18}$	54.13 ± 0.56	54.12 ± 0.56	μm	0.00
ρ_g	1.162 ± 0.004	1.163 ± 0.004	g/cm^3	0.00
Ψ_A	58 ± 9	58 ± 9	μrad	0.00
Ψ_P	0 ± 45	0 ± 45	μrad	0.00
ϵ	0.2 ± 0.4	0.4 ± 0.4	μm	0.12
r_A	7.5 ± 1.8	7.5 ± 1.8	μm	0.00
γ	1.012 ± 0.005	1.010 ± 0.002	–	0.29

The fit to the simplified model had a $\chi^2 = 274.99$ with $\nu = 285$ degrees of freedom (DOF): 95 data runs with 3 torque in-phase torque amplitudes (285 DOF), 5 measured fit parameters (0 DOF), and no unconstrained fit parameters. The probability of observing a χ^2 greater than the fit was $P = .654$. The fits of purely Newtonian torques to the corrected in-phase data is plotted as the solid lines in figure 11.1 along with the data.

Parameter	Measured	Fit	Units	χ^2
x_0	-0.130 ± 0.004	-0.129 ± 0.003	mm	0.10
y_0	-2.138 ± 0.003	-2.136 ± 0.003	mm	0.48
s_0	13.1 ± 1.4	14.1 ± 0.7	μm	0.55
ϵ	0.2 ± 0.4	0.4 ± 0.4	μm	0.14
γ	1.012 ± 0.005	1.010 ± 0.002	–	0.28

11.4 Yukawa Fits

We then searched for the inclusion of a single Yukawa torque with λ between 5 μm and 9 mm by minimizing the same χ^2 function but adding to the Newtonian model a Yukawa torque at the given λ with an additional freely-varying scale parameter α, $\widetilde{N}_m(\vec{\zeta}_j, \vec{\eta}, \infty) + \alpha \widetilde{N}_m(\vec{\zeta}_j, \vec{\eta}, \lambda)$. None of the Yukawa potentials were preferred at 2σ ($\Delta\chi^2 = 6.17$) with the best fit $\Delta\chi^2 = 3.3$ at $\lambda = 7.1\,\mu$m. We placed positive and negative exclusion limits, $\pm\alpha_{95}$ based on the $\Delta\chi^2 = 6.17$ surface, see table 11.4. We placed a 2σ limit on the absolute value of α at each λ by finding the value $|\alpha_{95}|$ at which

$$\int_{-|\alpha_{95}|}^{|\alpha_{95}|} \mathcal{N}(\alpha^*, \sigma_\alpha) d\alpha = 0.95$$

where $\mathcal{N}(\alpha^*, \sigma_\alpha)$ is a normal distribution with mean and standard deviation given by the best fit value with uncertainty, $\alpha^* \pm \sigma_\alpha$, see figure 11.3. The full set of limits over the range of λ tested are given in table 11.4.

λ [mm]	$\alpha^* \pm \sigma_\alpha$	$+\alpha_{95}$	$-\alpha_{95}$	$\lvert\alpha_{95}\rvert$	χ^2
0.0050	$4.09\times10^6 \pm 2.58\times10^6$	1.18×10^7	-1.63×10^6	8.45×10^6	271.89
0.0056	$8.6\times10^5 \pm 5.29\times10^5$	2.4×10^6	-3.35×10^5	1.75×10^6	271.78
0.0063	$1.93\times10^5 \pm 1.17\times10^5$	5.31×10^5	-6.18×10^4	3.9×10^5	271.72
0.0071	$4.76\times10^4 \pm 2.86\times10^4$	1.29×10^5	-1.53×10^4	9.58×10^4	271.71
0.0079	$1.5\times10^4 \pm 8.96\times10^3$	3.99×10^4	-4.88×10^3	3.01×10^4	271.73
0.0089	$4.52\times10^3 \pm 2.71\times10^3$	1.19×10^4	-1.5×10^3	9.1×10^3	271.79

λ [mm]	$\alpha^* \pm \sigma_\alpha$	$+\alpha_{95}$	$-\alpha_{95}$	$\lvert\alpha_{95}\rvert$	χ^2
0.0100	$1.53\times10^3 \pm 923$	3.99×10^3	-520	3.09×10^3	271.86
0.0110	668 ± 406	1.73×10^3	-232	1.35×10^3	271.92
0.0130	176 ± 108	465	-63.5	359	272.04
0.0140	102 ± 63	268	-37.3	208	272.09
0.0160	40.3 ± 25.3	106	-15.2	83	272.19
0.0180	18.9 ± 12	49.4	-7.36	39.2	272.27
0.0200	10.1 ± 6.47	26.3	-4.02	21	272.34
0.0220	5.91 ± 3.83	15.4	-2.41	12.4	272.41
0.0250	3.03 ± 2	7.9	-1.27	6.4	272.50
0.0280	1.75 ± 1.17	4.51	-0.886	3.73	272.59
0.0320	0.963 ± 0.661	2.56	-0.507	2.08	272.71
0.0350	0.663 ± 0.464	1.77	-0.36	1.45	272.81
0.0400	0.394 ± 0.286	1.06	-0.226	0.877	272.97
0.0450	0.257 ± 0.194	0.699	-0.157	0.585	273.13
0.0500	0.179 ± 0.142	0.494	-0.117	0.419	273.30
0.0560	0.124 ± 0.104	0.35	-0.0884	0.3	273.49
0.0630	0.0862 ± 0.078	0.251	-0.0685	0.218	273.71
0.0710	0.0601 ± 0.06	0.183	-0.055	0.162	273.94
0.0790	0.0437 ± 0.0485	0.14	-0.0469	0.126	274.14
0.0890	0.0304 ± 0.0393	0.106	-0.0407	0.097	274.36
0.1000	0.021 ± 0.0326	0.0813	-0.0365	0.0766	274.56
0.1100	0.0151 ± 0.0285	0.0666	-0.034	0.0641	274.70
0.1300	0.0076 ± 0.0231	0.048	-0.0312	0.0487	274.88
0.1400	0.00511 ± 0.0213	0.042	-0.0304	0.0439	274.93
0.1600	0.00157 ± 0.0187	0.0336	-0.0293	0.0376	274.98
0.1800	-0.000748 ± 0.0169	0.0282	-0.0287	0.0339	274.99

λ [mm]	$\alpha^* \pm \sigma_\alpha$	$+\alpha_{95}$	$-\alpha_{95}$	$\lvert\alpha_{95}\rvert$	χ^2
0.2000	-0.00235 ± 0.0157	0.0245	-0.0284	0.0317	274.97
0.2200	-0.00351 ± 0.0147	0.0219	-0.0281	0.0303	274.94
0.2500	-0.00471 ± 0.0137	0.0192	-0.0279	0.029	274.88
0.2800	-0.00552 ± 0.013	0.0174	-0.0278	0.0282	274.81
0.3200	-0.00624 ± 0.0123	0.0157	-0.0276	0.0275	274.74
0.3500	-0.00661 ± 0.0119	0.0148	-0.0275	0.0271	274.69
0.4000	-0.00701 ± 0.0114	0.0137	-0.0273	0.0265	274.62
0.4500	-0.00723 ± 0.011	0.0129	-0.0269	0.026	274.57
0.5000	-0.00731 ± 0.0107	0.0123	-0.0265	0.0254	274.53
0.5600	-0.00728 ± 0.0103	0.0117	-0.0259	0.0247	274.49
0.6300	-0.00713 ± 0.00982	0.0111	-0.025	0.0238	274.47
0.7100	-0.00685 ± 0.00936	0.0105	-0.0239	0.0227	274.46
0.7900	-0.00653 ± 0.00893	0.01	-0.0228	0.0217	274.46
0.8900	-0.00612 ± 0.00845	0.00953	-0.0215	0.0205	274.47
1.0000	-0.00569 ± 0.00796	0.00903	-0.0201	0.0192	274.49
1.1000	-0.00534 ± 0.00763	0.00872	-0.0192	0.0183	274.50
1.3000	-0.00478 ± 0.00706	0.00816	-0.0175	0.0168	274.53
1.4000	-0.00456 ± 0.00683	0.00795	-0.0169	0.0162	274.55
1.6000	-0.00421 ± 0.00648	0.0076	-0.0158	0.0152	274.57
1.8000	-0.00395 ± 0.00621	0.00734	-0.015	0.0145	274.59
2.0000	-0.00375 ± 0.00599	0.00712	-0.0144	0.014	274.60
2.2000	-0.0036 ± 0.00585	0.00699	-0.014	0.0136	274.61
2.5000	-0.00344 ± 0.00567	0.00682	-0.0135	0.0131	274.63
2.8000	-0.00332 ± 0.00555	0.00669	-0.0132	0.0128	274.64
3.2000	-0.0032 ± 0.00543	0.00657	-0.0128	0.0125	274.64
3.5000	-0.00314 ± 0.00536	0.00651	-0.0126	0.0123	274.65

λ [mm]	$\alpha^* \pm \sigma_\alpha$	$+\alpha_{95}$	$-\alpha_{95}$	$\lvert\alpha_{95}\rvert$	χ^2
4.0000	-0.00307 ± 0.00526	0.0064	-0.0124	0.0121	274.65
4.5000	-0.00303 ± 0.00523	0.00637	-0.0123	0.012	274.66
5.0000	-0.00299 ± 0.00517	0.0063	-0.0121	0.0118	274.66
5.6000	-0.00295 ± 0.00515	0.0063	-0.012	0.0118	274.66
6.3000	-0.00293 ± 0.00512	0.00627	-0.012	0.0117	274.67
7.1000	-0.0029 ± 0.0051	0.00625	-0.0119	0.0116	274.67
7.9000	-0.00289 ± 0.00508	0.00623	-0.0119	0.0116	274.67
8.9000	-0.00288 ± 0.00507	0.00621	-0.0118	0.0116	274.67

11.5 Conclusions

We have excluded at 95% confidence gravitational strength Yukawa interactions with length scales $\lambda > 39\,\mu$m and set new limits between $\lambda = 8\,\mu$m and $90\,\mu$m. The constraint on $\alpha = 8/3$ implies the largest single extra dimension has a toroidal radius of $R < 30\,\mu$m. The result also constrains the dilaton (or heavy graviton [5]) and radion unification masses to be greater than 5.1 meV and 7.1 TeV, respectively.

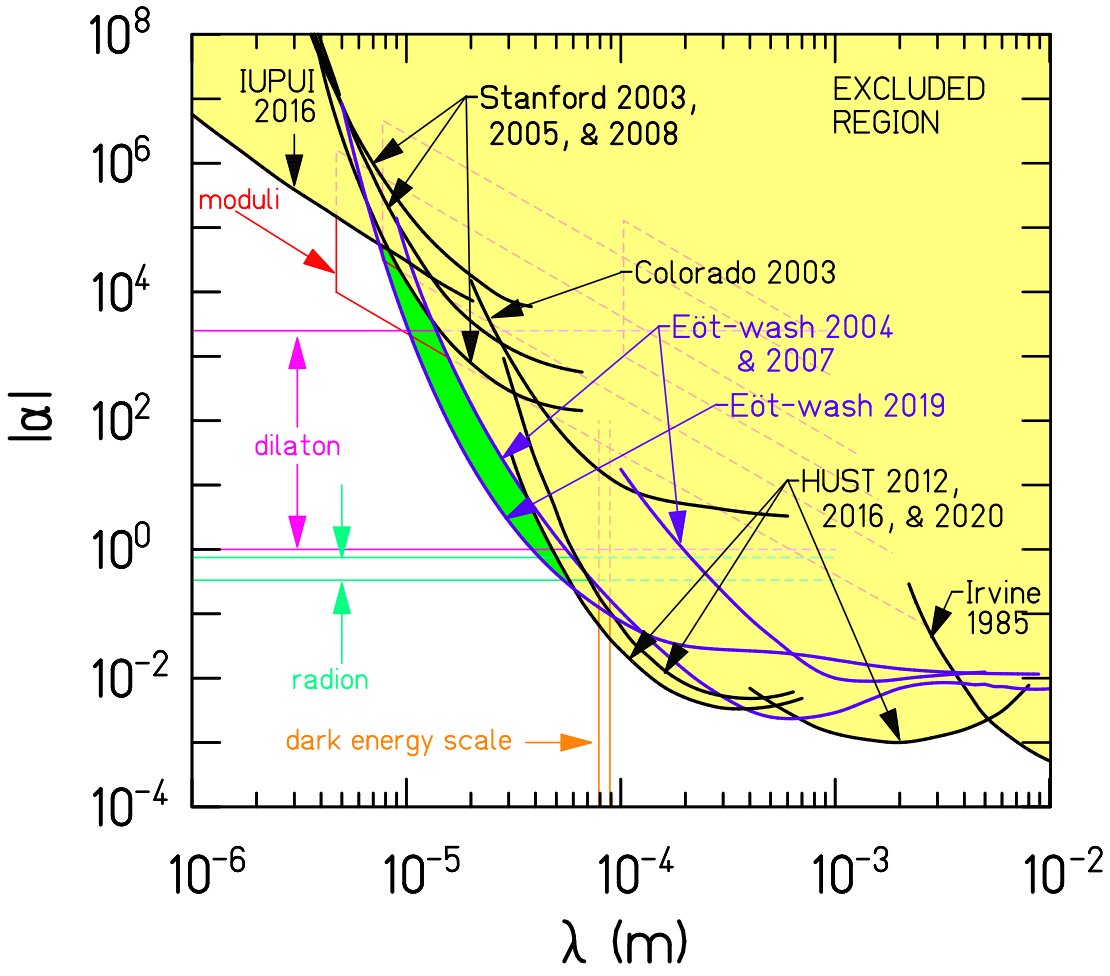

Figure 11.3: **95% confidence level constraints on Yukawa interactions** $(\lambda, |\alpha|)$ **from this experiment** - The green region is newly excluded by our experiment. Solid blue curves are previous limits from the Eöt-Wash group [36][31] while solid black lines correspond to limits from [16][50][60][17][44][25][30][49].

BIBLIOGRAPHY

[1] G. Aad, T. Abajyan, B. Abbott, J. Abdallah, S. Abdel Khalek, A. A. Abdelalim, O. Abdinov, R. Aben, B. Abi, M. Abolins, O. S. AbouZeid, H. Abramowicz, H. Abreu, B. S. Acharya, L. Adamczyk, D. L. Adams, T. N. Addy, J. Adelman, S. Adomeit, P. Adragna, T. Adye, S. Aefsky, J. A. Aguilar-Saavedra, M. Agustoni, M. Aharrouche, S. P. Ahlen, F. Ahles, A. Ahmad, M. Ahsan, G. Aielli, T. Akdogan, T. P. A. Åkesson, G. Akimoto, A. V. Akimov, M. S. Alam, M. A. Alam, J. Albert, S. Albrand, M. Aleksa, I. N. Aleksandrov, F. Alessandria, C. Alexa, G. Alexander, G. Alexandre, T. Alexopoulos, M. Alhroob, M. Aliev, G. Alimonti, J. Alison, B. M. M. Allbrooke, P. P. Allport, S. E. Allwood-Spiers, J. Almond, A. Aloisio, R. Alon, A. Alonso, F. Alonso, A. Altheimer, B. Alvarez Gonzalez, M. G. Alviggi, K. Amako, C. Amelung, V. V. Ammosov, S. P. Amor Dos Santos, A. Amorim, N. Amram, C. Anastopoulos, L. S. Ancu, N. Andari, T. Andeen, C. F. Anders, G. Anders, K. J. Anderson, A. Andreazza, V. Andrei, M-L. Andrieux, X. S. Anduaga, P. Anger, A. Angerami, F. Anghinolfi, A. Anisenkov, N. Anjos, A. Annovi, A. Antonaki, M. Antonelli, A. Antonov, J. Antos, F. Anulli, M. Aoki, S. Aoun, L. Aperio Bella, R. Apolle, G. Arabidze, I. Aracena, Y. Arai, A. T. H. Arce, S. Arfaoui, J-F. Arguin, E. Arik, M. Arik, A. J. Armbruster, O. Arnaez, V. Arnal, C. Arnault, A. Artamonov, G. Artoni, D. Arutinov, S. Asai, R. Asfandiyarov, S. Ask, B. Åsman, L. Asquith, K. Assamagan, A. Astbury, M. Atkinson, B. Aubert, E. Auge, K. Augsten, M. Aurousseau, G. Avolio, R. Avramidou, D. Axen, G. Azuelos, Y. Azuma, M. A. Baak, G. Baccaglioni, C. Bacci, A. M. Bach, H. Bachacou, K. Bachas, M. Backes, M. Backhaus, E. Badescu, P. Bagnaia, S. Bahinipati, Y. Bai, D. C. Bailey, T. Bain, J. T. Baines, O. K. Baker, M. D. Baker, S. Baker, E. Banas, P. Banerjee, Sw. Banerjee, D. Banfi, A. Bangert, V. Bansal, H. S. Bansil, L. Barak, S. P. Baranov, A. Barbaro Galtieri, T. Barber, E. L. Barberio, D. Barberis, M. Barbero, D. Y. Bardin, T. Barillari, M. Barisonzi, T. Barklow, N. Barlow, B. M. Barnett, R. M. Barnett, A. Baroncelli, G. Barone, A. J. Barr, F. Barreiro, J. Barreiro Guimarães da Costa, P. Barrillon, R. Bartoldus, A. E. Barton, V. Bartsch, A. Basye, R. L. Bates, L. Batkova, J. R. Batley, A. Battaglia, M. Battistin, F. Bauer, H. S. Bawa, S. Beale, T. Beau, P. H. Beauchemin, R. Beccherle, P. Bechtle, H. P. Beck, A. K. Becker, S. Becker, M. Beckingham, K. H. Becks, A. J. Beddall, A. Beddall, S. Bedikian, V. A. Bednyakov, C. P. Bee, L. J. Beemster, M. Begel, S. Behar Harpaz, P. K. Behera, M. Beimforde, C. Belanger-Champagne, P. J. Bell, W. H. Bell, G. Bella, L. Bellagamba, F. Bellina, M. Bellomo, A. Belloni, O. Beloborodova, K. Belotskiy, O. Beltramello, O. Benary, D. Benchekroun, K. Bendtz, N. Benekos, Y. Benhammou, E. Benhar Noccioli, J. A. Benitez Garcia, D. P. Benjamin, M. Benoit, J. R. Bensinger, K. Benslama, S. Bentvelsen, D. Berge, E. Bergeaas Ku-

utmann, N. Berger, F. Berghaus, E. Berglund, J. Beringer, P. Bernat, R. Bernhard, C. Bernius, T. Berry, C. Bertella, A. Bertin, F. Bertolucci, M. I. Besana, G. J. Besjes, N. Besson, S. Bethke, W. Bhimji, R. M. Bianchi, M. Bianco, O. Biebel, S. P. Bieniek, K. Bierwagen, J. Biesiada, M. Biglietti, H. Bilokon, M. Bindi, S. Binet, A. Bingul, C. Bini, C. Biscarat, B. Bittner, K. M. Black, R. E. Blair, J.-B. Blanchard, G. Blanchot, T. Blazek, I. Bloch, C. Blocker, J. Blocki, A. Blondel, W. Blum, U. Blumenschein, G. J. Bobbink, V. B. Bobrovnikov, S. S. Bocchetta, A. Bocci, C. R. Boddy, M. Boehler, J. Boek, N. Boelaert, J. A. Bogaerts, A. Bogdanchikov, A. Bogouch, C. Bohm, J. Bohm, V. Boisvert, T. Bold, V. Boldea, N. M. Bolnet, M. Bomben, M. Bona, M. Boonekamp, S. Bordoni, C. Borer, A. Borisov, G. Borissov, I. Borjanovic, M. Borri, S. Borroni, V. Bortolotto, K. Bos, D. Boscherini, M. Bosman, H. Boterenbrood, J. Bouchami, J. Boudreau, E. V. Bouhova-Thacker, D. Boumediene, C. Bourdarios, N. Bousson, A. Boveia, J. Boyd, I. R. Boyko, I. Bozovic-Jelisavcic, J. Bracinik, P. Branchini, G. W. Brandenburg, A. Brandt, G. Brandt, O. Brandt, U. Bratzler, B. Brau, J. E. Brau, H. M. Braun, S. F. Brazzale, B. Brelier, J. Bremer, K. Brendlinger, R. Brenner, S. Bressler, D. Britton, F. M. Brochu, I. Brock, R. Brock, F. Broggi, C. Bromberg, J. Bronner, G. Brooijmans, T. Brooks, W. K. Brooks, G. Brown, H. Brown, P. A. Bruckman de Renstrom, D. Bruncko, R. Bruneliere, S. Brunet, A. Bruni, G. Bruni, M. Bruschi, T. Buanes, Q. Buat, F. Bucci, J. Buchanan, P. Buchholz, R. M. Buckingham, A. G. Buckley, S. I. Buda, I. A. Budagov, B. Budick, V. Büscher, L. Bugge, O. Bulekov, A. C. Bundock, M. Bunse, T. Buran, H. Burckhart, S. Burdin, T. Burgess, S. Burke, E. Busato, P. Bussey, C. P. Buszello, B. Butler, J. M. Butler, C. M. Buttar, J. M. Butterworth, W. Buttinger, M. Byszewski, S. Cabrera Urbán, D. Caforio, O. Cakir, P. Calafiura, G. Calderini, P. Calfayan, R. Calkins, L. P. Caloba, R. Caloi, D. Calvet, S. Calvet, R. Camacho Toro, P. Camarri, D. Cameron, L. M. . Search for dark matter candidates and large extra dimensions in events with a photon and missing transverse momentum in *pp* collision data at $\sqrt{s}$=7 TeV with the atlas detector. *Phys. Rev. Lett.*, 110:011802, Jan 2013.

[2] EG Adelberger, JH Gundlach, BR Heckel, S Hoedl, and S Schlamminger. Torsion balance experiments: A low-energy frontier of particle physics. *Progress in Particle and Nuclear Physics*, 62(1):102–134, 2009.

[3] EG Adelberger, Blayne R Heckel, S Hoedl, CD Hoyle, DJ Kapner, and A Upadhye. Particle-physics implications of a recent test of the gravitational inverse-square law. *Physical review letters*, 98(13):131104, 2007.

[4] E.G. Adelberger, B.R. Heckel, and A.E. Nelson. Tests of the gravitational inverse-square law. *Annual Review of Nuclear and Particle Science*, 53(1):77–121, Dec 2003.

[5] Katsuki Aoki and Shinji Mukohyama. Massive gravitons as dark matter and gravitational waves. *Phys. Rev. D*, 94:024001, Jul 2016.

[6] Nima Arkani–Hamed, Savas Dimopoulos, and Gia Dvali. The hierarchy problem and new dimensions at a millimeter. *Physics Letters B*, 429(3-4):263–272, Jun 1998.

[7] L. J. Azevedo. Magnetic susceptibility of stycast 1266 epoxy. *Review of Scientific Instruments*, 54(12):1793–1793, 1983.

[8] Silas R. Beane. On the importance of testing gravity at distances less than 1cm. *General Relativity and Gravitation*, 29(8):945–951, Aug 1997.

[9] R. O. Behunin, D. A. R. Dalvit, R. S. Decca, and C. C. Speake. Limits on the accuracy of force sensing at short separations due to patch potentials. *Phys. Rev. D*, 89:051301, Mar 2014.

[10] L Blanchet, J Novak, E Augé, J Dumarchez, and Trân Thanh Vân J. Proceedings of the xlvith rencontres de moriond and gphys colloquium 2011: Gravitational waves and experimental gravity, 2011.

[11] Clare Burrage and Jeremy Sakstein. Tests of chameleon gravity. *Living Reviews in Relativity*, 21(1):1, Mar 2018.

[12] JB Camp, TW Darling, and Ronald E Brown. Macroscopic variations of surface potentials of conductors. *Journal of applied physics*, 69(10):7126–7129, 1991.

[13] A. Cavalleri, G. Ciani, R. Dolesi, A. Heptonstall, M. Hueller, D. Nicolodi, S. Rowan, D. Tombolato, S. Vitale, P. J. Wass, and W. J. Weber. Increased brownian force noise from molecular impacts in a constrained volume. *Phys. Rev. Lett.*, 103:140601, Sep 2009.

[14] A. Cavalleri, G. Ciani, R. Dolesi, M. Hueller, D. Nicolodi, D. Tombolato, S. Vitale, P.J. Wass, and W.J. Weber. Gas damping force noise on a macroscopic test body in an infinite gas reservoir. *Physics Letters A*, 374(34):3365 – 3369, 2010.

[15] Aston S.N. Collins C.J. Nelson M.J. Speake C.C. Chalkley, E.C. Testing the inverse square law of gravitation at short range with a superconducting torsion balance. In *Talk given at the XLVI Rencontres de Moriond. Gravitational Waves and Experimental Gravity, La Thuile, Aosta, 20-27 March 2011*, 2011.

[16] Y.-J. Chen, W. K. Tham, D. E. Krause, D. López, E. Fischbach, and R. S. Decca. Stronger limits on hypothetical yukawa interactions in the 30–8000 nm range. *Phys. Rev. Lett.*, 116:221102, Jun 2016.

[17] J. Chiaverini, S. J. Smullin, A. A. Geraci, D. M. Weld, and A. Kapitulnik. New experimental constraints on non-newtonian forces below 100 μm. *Phys. Rev. Lett.*, 90:151101, Apr 2003.

[18] Planck Collaboration, N. Aghanim, Y. Akrami, M. Ashdown, , J. Aumont, C. Baccigalupi, M. Ballardini, A. J. Banday, R. B. Barreiro, N. Bartolo, S. Basak, R. Battye, K. Benabed, J. P. Bernard, M. Bersanelli, P. Bielewicz, J. J. Bock, J. R. Bond, J. Borrill, F. R. Bouchet, F. Boulanger, M. Bucher, C. Burigana, R. C. Butler, E. Calabrese, J. F. Cardoso, J. Carron, A. Challinor, H. C. Chiang, J. Chluba, L. P. L. Colombo, C. Combet, D. Contreras, B. P. Crill, F. Cuttaia, P. de Bernardis, G. de Zotti, J. Delabrouille, J. M. Delouis, E. Di Valentino, J. M. Diego, O. Doré, M. Douspis, A. Ducout, X. Dupac, S. Dusini, G. Efstathiou, F. Elsner, T. A. Enßlin, H. K. Eriksen, Y. Fantaye, M. Farhang, J. Fergusson, R. Fernandez-Cobos, F. Finelli, F. Forastieri, M. Frailis, A. A. Fraisse, E. Franceschi, A. Frolov, S. Galeotta, S. Galli, K. Ganga, R. T. Génova-Santos, M. Gerbino, T. Ghosh, J. González-Nuevo, K. M. Górski, S. Gratton, A. Gruppuso, J. E. Gudmundsson, J. Hamann, W. Handley, F. K. Hansen, D. Herranz, S. R. Hildebrandt, E. Hivon, Z. Huang, A. H. Jaffe, W. C. Jones, A. Karakci, E. Keihänen, R. Keskitalo, K. Kiiveri, J. Kim, T. S. Kisner, L. Knox, N. Krachmalnicoff, M. Kunz, H. Kurki-Suonio, G. Lagache, J. M. Lamarre, A. Lasenby, M. Lattanzi, C. R. Lawrence, M. Le Jeune, P. Lemos, J. Lesgourgues, F. Levrier, A. Lewis, M. Liguori, P. B. Lilje, M. Lilley, V. Lindholm, M. López-Caniego, P. M. Lubin, Y. Z. Ma, J. F. Macías-Pérez, G. Maggio, D. Maino, N. Mandolesi, A. Mangilli, A. Marcos-Caballero, M. Maris, P. G. Martin, M. Martinelli, E. Martínez-González, S. Matarrese, N. Mauri, J. D. McEwen, P. R. Meinhold, A. Melchiorri, A. Mennella, M. Migliaccio, M. Millea, S. Mitra, M. A. Miville-Deschênes, D. Molinari, L. Montier, G. Morgante, A. Moss, P. Natoli, H. U. Nørgaard-Nielsen, L. Pagano, D. Paoletti, B. Partridge, G. Patanchon, H. V. Peiris, F. Perrotta, V. Pettorino, F. Piacentini, L. Polastri, G. Polenta, J. L. Puget, J. P. Rachen, M. Reinecke, M. Remazeilles, A. Renzi, G. Rocha, C. Rosset, G. Roudier, J. A. Rubiño-Martín, B. Ruiz-Granados, L. Salvati, M. Sandri, M. Savelainen, D. Scott, E. P. S. Shellard, C. Sirignano, G. Sirri, L. D. Spencer, R. Sunyaev, A. S. Suur-Uski, J. A. Tauber, D. Tavagnacco, M. Tenti, L. Toffolatti, M. Tomasi, T. Trombetti, L. Valenziano, J. Valiviita, B. Van Tent, L. Vibert, P. Vielva, F. Villa, N. Vittorio, B. D. Wandelt, I. K. Wehus, M. White, S. D. M. White, A. Zacchei, and A. Zonca. Planck 2018 results. vi. cosmological parameters, 2018.

[19] Ted Cook. *A test of the gravitational inverse-square law at short distance.* PhD thesis, 2013.

[20] CRC Handbook. *CRC Handbook of Chemistry and Physics, 85th Edition.* CRC Press, 85 edition, 2004.

[21] N.G. Deshpande, Stephen D.H. Hsu, and Jing Jiang. Long range forces and limits on unparticle interactions. *Physics Letters B*, 659(5):888–890, Feb 2008.

[22] R. Dolesi, M. Hueller, D. Nicolodi, D. Tombolato, S. Vitale, P. J. Wass, W. J. Weber, M. Evans, P. Fritschel, R. Weiss, J. H. Gundlach, C. A. Hagedorn, S. Schlamminger, G. Ciani, and A. Cavalleri. Brownian force noise from molecular collisions and the sensitivity of advanced gravitational wave observatories. *Phys. Rev. D*, 84:063007, Sep 2011.

[23] Christian D'Urso and E. G. Adelberger. Translation of multipoles for a $1/r$ potential. *Phys. Rev. D*, 55:7970–7972, Jun 1997.

[24] Howard Georgi. Unparticle physics. *Physical Review Letters*, 98(22), May 2007.

[25] Andrew A. Geraci, Sylvia J. Smullin, David M. Weld, John Chiaverini, and Aharon Kapitulnik. Improved constraints on non-newtonian forces at 10 microns. *Phys. Rev. D*, 78:022002, Jul 2008.

[26] Charles A Hagedorn. *A sub-millimeter parallel-plate test of gravity.* 2015.

[27] Steen Hannestad and Georg G. Raffelt. Supernova and neutron-star limits on large extra dimensions reexamined. *Phys. Rev. D*, 67:125008, Jun 2003.

[28] D. A. Hite, Y. Colombe, A. C. Wilson, K. R. Brown, U. Warring, R. Jördens, J. D. Jost, K. S. McKay, D. P. Pappas, D. Leibfried, and D. J. Wineland. 100-fold reduction of electric-field noise in an ion trap cleaned with in situ argon-ion-beam bombardment. *Phys. Rev. Lett.*, 109:103001, Sep 2012.

[29] DA Hite, Y Colombe, Andrew C Wilson, DTC Allcock, D Leibfried, DJ Wineland, and DP Pappas. Surface science for improved ion traps. *MRS bulletin*, 38(10):826–833, 2013.

[30] J. K. Hoskins, R. D. Newman, R. Spero, and J. Schultz. Experimental tests of the gravitational inverse-square law for mass separations from 2 to 105 cm. *Phys. Rev. D*, 32:3084–3095, Dec 1985.

[31] C. D. Hoyle, D. J. Kapner, B. R. Heckel, E. G. Adelberger, J. H. Gundlach, U. Schmidt, and H. E. Swanson. Submillimeter tests of the gravitational inverse-square law. *Phys. Rev. D*, 70:042004, Aug 2004.

[32] C. D. Hoyle, U. Schmidt, B. R. Heckel, E. G. Adelberger, J. H. Gundlach, D. J. Kapner, and H. E. Swanson. Submillimeter test of the gravitational inverse-square law: A search for "large" extra dimensions. *Phys. Rev. Lett.*, 86:1418–1421, Feb 2001.

[33] John David Jackson. *Classical electrodynamics*. Wiley, New York, NY, 3rd ed. edition, 1999.

[34] David B Kaplan and Mark B Wise. Couplings of a light dilaton and violations of the equivalence principle. *Journal of High Energy Physics*, 2000(08):037–037, Aug 2000.

[35] D. J. Kapner, T. S. Cook, E. G. Adelberger, J. H. Gundlach, B. R. Heckel, C. D. Hoyle, and H. E. Swanson. Tests of the gravitational inverse-square law below the dark-energy length scale. *Phys. Rev. Lett.*, 98:021101, Jan 2007.

[36] Daniel J Kapner. *A short-range test of Newton's gravitational inverse-square law*. Washington Univ., 2005.

[37] Frank V. Marcoline. Calculating torques on pendula due to yukawa, $\sigma \cdot r$ and $\sigma \cdot \sigma$ interactions. 2004.

[38] Ann E. Nelson and Jonathan Walsh. Chameleon vector bosons. *Phys. Rev. D*, 77:095006, May 2008.

[39] M Phelps. First contact application and removal procedure. *Internal LIGO Document*, 2010.

[40] M.A. Pinsky. *Partial Differential Equations and Boundary-value Problems with Applications*. International series in pure and applied mathematics. Waveland Press, 2003.

[41] Lisa Randall and Raman Sundrum. An alternative to compactification. *Phys. Rev. Lett.*, 83:4690–4693, Dec 1999.

[42] Lisa Randall and Raman Sundrum. Large mass hierarchy from a small extra dimension. *Phys. Rev. Lett.*, 83:3370–3373, Oct 1999.

[43] S. Schlamminger, C. A. Hagedorn, and J. H. Gundlach. Indirect evidence for lévy walks in squeeze film damping. *Phys. Rev. D*, 81:123008, Jun 2010.

[44] S. J. Smullin, A. A. Geraci, D. M. Weld, J. Chiaverini, S. Holmes, and A. Kapitulnik. Constraints on yukawa-type deviations from newtonian gravity at 20 microns. *Phys. Rev. D*, 72:122001, Dec 2005.

[45] C. C. Speake and C. Trenkel. Forces between conducting surfaces due to spatial variations of surface potential. *Phys. Rev. Lett.*, 90:160403, Apr 2003.

[46] Kerkira JS Stockton. Active vibration isolation systems. 2017.

[47] M.A.G. Suijlen, J.J. Koning, M.A.J. van Gils, and H.C.W. Beijerinck. Squeeze film damping in the free molecular flow regime with full thermal accommodation. *Sensors and Actuators A: Physical*, 156(1):171 – 179, 2009. EUROSENSORS XXII, 2008.

[48] Raman Sundrum. Fat gravitons, the cosmological constant and submillimeter tests. *Physical Review D*, 69(4), Feb 2004.

[49] Wen-Hai Tan, An-Bin Du, Wen-Can Dong, Shan-Qing Yang, Cheng-Gang Shao, Sheng-Guo Guan, Qing-Lan Wang, Bi-Fu Zhan, Peng-Shun Luo, Liang-Cheng Tu, and Jun Luo. Improvement for testing the gravitational inverse-square law at the submillimeter range. *Phys. Rev. Lett.*, 124:051301, Feb 2020.

[50] Wen-Hai Tan, Shan-Qing Yang, Cheng-Gang Shao, Jia Li, An-Bin Du, Bi-Fu Zhan, Qing-Lan Wang, Peng-Shun Luo, Liang-Cheng Tu, and Jun Luo. New test of the gravitational inverse-square law at the submillimeter range with dual modulation and compensation. *Phys. Rev. Lett.*, 116:131101, Mar 2016.

[51] W. A. Terrano, E. G. Adelberger, J. G. Lee, and B. R. Heckel. Short-range, spin-dependent interactions of electrons: A probe for exotic pseudo-goldstone bosons. *Phys. Rev. Lett.*, 115:201801, Nov 2015.

[52] William A Terrano. *Torsion pendulum searches for macroscopic spin-interactions as a window on new physics*. 2015.

[53] Amol Upadhye. Dark energy fifth forces in torsion pendulum experiments. *Physical Review D*, 86(10), Nov 2012.

[54] Amol Upadhye. Symmetron dark energy in laboratory experiments. *Phys. Rev. Lett.*, 110:031301, Jan 2013.

[55] Amol Upadhye, Wayne Hu, and Justin Khoury. Quantum stability of chameleon field theories. *Phys. Rev. Lett.*, 109:041301, Jul 2012.

[56] Timo Varpula and Torsti Poutanen. Magnetic field fluctuations arising from thermal motion of electric charge in conductors. *Journal of applied physics*, 55(11):4015–4021, 1984.

[57] Yethadka Venkateswara and Krishna Raj. *Cryogenic test of gravitational inverse square law below 100-micrometer length scales*. PhD thesis, 2010.

[58] Steven Weinberg. The cosmological constant problem. *Rev. Mod. Phys.*, 61:1–23, Jan 1989.

[59] David Minot Weld. Design, construction, and operation of an apparatus for detecting short-length-scale deviations from newtonian gravity. 2007.

[60] Shan-Qing Yang, Bi-Fu Zhan, Qing-Lan Wang, Cheng-Gang Shao, Liang-Cheng Tu, Wen-Hai Tan, and Jun Luo. Test of the gravitational inverse square law at millimeter ranges. *Phys. Rev. Lett.*, 108:081101, Feb 2012.

Appendix A

A.1 Data

The following is the list of data runs used in the final torque fit to pure Newtonian and Netwonian + Yukawa models. Run names given by "kunXXXX" had at least one missing record corrected by linear interpolation between adjacent points; this had negligible effect on the torque fits. A set of runs between run6448 and run6653 were excluded due to a slight touching of the attractor and screen indicated by a short in the attractor-screen capacitance signal. We have rotated the torque values into a single in-phase component, scaled them by the measured torque scale calibration, and have subtracted systematic torques. The files containing the *sine* and *cosine* amplitudes and errors without the rotation or systematic corrections can be found with the *.sum* extension in `\\TYCHO-BRAHE\SRDATA\BATDATA\`.

run	s [μm]	N_{120} [fNm]	N_{18} [fNm]	N_{54} [fNm]
run6276	164.7 ± 0.7	0.808 ± 0.0107	0.9441 ± 0.0079	0.1072 ± 0.0055
run6279	75.2 ± 0.7	1.4199 ± 0.0188	1.0772 ± 0.0109	0.1171 ± 0.0085
kun6282	60.2 ± 0.7	1.5532 ± 0.0642	1.0429 ± 0.0199	0.1265 ± 0.0175
run6286	60.4 ± 0.7	1.5560 ± 0.0472	1.0441 ± 0.0366	0.1173 ± 0.0253
run6302	49.6 ± 0.7	1.7514 ± 0.3756	1.0262 ± 0.0744	0.1230 ± 0.0484
run6347	58.8 ± 0.7	1.5411 ± 0.0403	1.0625 ± 0.0328	0.1158 ± 0.0202
run6373	52.1 ± 0.7	1.7113 ± 0.0395	1.1013 ± 0.0722	0.1376 ± 0.0380
run6377	366.4 ± 0.8	0.2317 ± 0.0099	0.7785 ± 0.0098	0.0503 ± 0.0076
run6378	366.5 ± 0.8	0.2162 ± 0.0129	0.7672 ± 0.0092	0.0679 ± 0.0074
run6381	983.7 ± 1.2	0.0068 ± 0.0211	0.4335 ± 0.0119	0.0093 ± 0.0075
run6384	60.5 ± 0.7	1.5182 ± 0.0571	1.0577 ± 0.0257	0.1031 ± 0.0213
run6387	54.4 ± 0.8	1.6398 ± 0.0263	1.1285 ± 0.0184	0.1324 ± 0.0124

run	s [μm]	N_{120} [fNm]	N_{18} [fNm]	N_{54} [fNm]
run6395	215.7 ± 0.7	0.5787 ± 0.0149	0.9234 ± 0.0085	0.0799 ± 0.0103
run6398	417.1 ± 0.9	0.1606 ± 0.0167	0.7546 ± 0.0102	0.0504 ± 0.0080
run6401	571.5 ± 1.0	0.0722 ± 0.0179	0.6563 ± 0.0087	0.0495 ± 0.0053
run6404	55.6 ± 0.7	1.6482 ± 0.0318	1.0497 ± 0.0197	0.1448 ± 0.0146
run6410	68.3 ± 0.7	1.4937 ± 0.0234	1.0770 ± 0.0244	0.1103 ± 0.0175
run6415	64.8 ± 0.7	1.5267 ± 0.0193	1.0726 ± 0.0239	0.1267 ± 0.0163
run6424	131.7 ± 0.7	1.0081 ± 0.0238	0.9799 ± 0.0148	0.1127 ± 0.0118
run6429	1231.8 ± 1.2	0.0222 ± 0.0146	0.3701 ± 0.0113	0.0072 ± 0.0078
run6435	55.1 ± 0.7	1.6572 ± 0.0507	1.0712 ± 0.0423	0.1317 ± 0.0227
run6438	50.7 ± 0.7	1.6995 ± 0.1410	1.0855 ± 0.1313	0.1510 ± 0.0453
run6443	54.2 ± 0.7	1.8585 ± 0.3398	0.9612 ± 0.1386	0.0658 ± 0.1765
run6448	68.0 ± 0.7	1.4493 ± 0.0676	1.1072 ± 0.0520	0.0781 ± 0.0262
run6653	65.9 ± 0.7	1.4680 ± 0.0644	1.1073 ± 0.0488	0.1111 ± 0.0212
run6659	81.4 ± 0.7	1.3822 ± 0.0160	1.0422 ± 0.0129	0.1195 ± 0.0068
run6662	63.4 ± 0.7	1.5076 ± 0.1289	0.6521 ± 0.3337	0.1899 ± 0.1476
run6664	63.4 ± 0.7	1.6170 ± 0.0839	0.9817 ± 0.0810	0.2021 ± 0.0318
run6673	80.3 ± 0.7	1.3517 ± 0.0249	1.0372 ± 0.0282	0.1314 ± 0.0084
run6679	58.0 ± 0.7	1.0456 ± 0.7213	1.1348 ± 0.2625	0.8082 ± 1.4227
run6682	2109.1 ± 1.2	-0.0011 ± 0.0179	0.1571 ± 0.0145	-0.0054 ± 0.0134
kun6685	57.4 ± 0.7	1.6987 ± 0.3914	1.1043 ± 0.1183	-0.0457 ± 0.7364
run6689	2548.0 ± 1.2	-0.0347 ± 0.0228	0.1128 ± 0.0064	0.0143 ± 0.0291
run6692	118.7 ± 0.7	1.0796 ± 0.0112	0.9864 ± 0.0071	0.1017 ± 0.0046
run6704	318.5 ± 0.8	0.2978 ± 0.0162	0.8081 ± 0.0088	0.0732 ± 0.0066
run6708	483.7 ± 0.9	0.1194 ± 0.0097	0.7098 ± 0.0082	0.0568 ± 0.0055
run6711	57.0 ± 0.7	1.7391 ± 0.1253	1.0487 ± 0.0428	-0.1969 ± 0.2556
run6713	56.9 ± 0.7	1.5757 ± 0.1361	1.0888 ± 0.0441	-0.0176 ± 0.2660

run	s [μm]	N_{120} [fNm]	N_{18} [fNm]	N_{54} [fNm]
kun6715	56.8 ± 0.7	1.4780 ± 0.1174	1.0726 ± 0.0423	0.2556 ± 0.2336
run6725	1521.5 ± 1.2	-0.0031 ± 0.0249	0.2710 ± 0.0066	0.0295 ± 0.0260
kun6729	122.0 ± 0.7	1.0502 ± 0.0147	0.9995 ± 0.0080	0.1020 ± 0.0077
run6732	104.0 ± 0.7	1.1883 ± 0.0182	1.0228 ± 0.0084	0.1276 ± 0.0050
run6735	66.0 ± 0.7	1.5099 ± 0.0715	1.0480 ± 0.0295	0.0841 ± 0.1436
kun6737	65.9 ± 0.7	1.4597 ± 0.0690	1.0946 ± 0.0285	0.1834 ± 0.1385
run6740	95.0 ± 0.7	1.2486 ± 0.0116	0.9949 ± 0.0092	0.1107 ± 0.0068
run6743	87.8 ± 0.7	1.3341 ± 0.0229	1.0057 ± 0.0171	0.1175 ± 0.0079
run6750	777.2 ± 1.1	0.0252 ± 0.0136	0.5366 ± 0.0051	0.0194 ± 0.0050
run6753	57.2 ± 0.7	1.5581 ± 0.5668	1.3034 ± 0.2158	0.2110 ± 1.1629
run6755	56.8 ± 0.7	1.6372 ± 0.4425	1.0123 ± 0.1539	0.2065 ± 0.8819
run6757	56.9 ± 0.7	0.4630 ± 0.7242	0.9849 ± 0.3068	2.5640 ± 1.4624
run6759	56.9 ± 0.7	1.9210 ± 0.8081	1.2076 ± 0.3710	-0.4850 ± 1.6146
run6762	688.3 ± 1.0	0.0320 ± 0.0112	0.5840 ± 0.0063	0.0249 ± 0.0053
run6765	257.1 ± 0.8	0.4515 ± 0.0094	0.8738 ± 0.0065	0.0764 ± 0.0049
run6768	295.4 ± 0.8	0.3592 ± 0.0235	0.8362 ± 0.0084	0.0744 ± 0.0068
run6771	102.4 ± 0.7	1.2008 ± 0.0140	1.0008 ± 0.0077	0.1050 ± 0.0051
kun6775	3036.3 ± 1.2	0.0287 ± 0.0359	0.0785 ± 0.0090	0.0299 ± 0.0434
run6778	87.4 ± 0.7	1.3307 ± 0.0204	1.0471 ± 0.0082	0.1194 ± 0.0055
run6781	75.2 ± 0.9	1.4302 ± 0.0174	1.0507 ± 0.0099	0.1280 ± 0.0064
run6784	67.6 ± 0.7	1.5115 ± 0.0344	1.0304 ± 0.0388	0.1303 ± 0.0151
run6787a	57.6 ± 0.7	2.2715 ± 0.3312	0.8031 ± 0.1156	-1.2174 ± 0.6814
run6787d	57.1 ± 0.7	1.2657 ± 0.2310	1.0658 ± 0.0991	0.7375 ± 0.4840
run6791	51.0 ± 0.7	1.5668 ± 0.4052	1.0119 ± 0.1263	0.2242 ± 0.8101
run6799	875.4 ± 1.1	0.0372 ± 0.0248	0.4852 ± 0.0064	0.0290 ± 0.0314
run6802	69.3 ± 0.7	1.4645 ± 0.1421	0.9998 ± 0.0529	-0.1326 ± 0.2846

run	s [μm]	N_{120} [fNm]	N_{18} [fNm]	N_{54} [fNm]
run6804	69.1 ± 0.7	1.4253 ± 0.0734	1.0064 ± 0.0257	0.0585 ± 0.1519
run6807	69.1 ± 0.7	1.4639 ± 0.0827	0.9903 ± 0.0296	0.0303 ± 0.1676
run6810	68.4 ± 0.7	1.4318 ± 0.0454	1.0169 ± 0.0158	0.0521 ± 0.0901
run6813	68.4 ± 0.8	1.4596 ± 0.0487	1.0322 ± 0.0160	0.0341 ± 0.0975
run6816	68.2 ± 0.7	1.4004 ± 0.0299	1.0441 ± 0.0113	0.1136 ± 0.0543
run6819	68.4 ± 0.7	1.4514 ± 0.0324	1.0554 ± 0.0106	0.0417 ± 0.0615
run6822	55.6 ± 0.7	1.6077 ± 0.0494	1.0526 ± 0.0161	0.0600 ± 0.0969
run6831	127.7 ± 0.7	0.9978 ± 0.0079	0.9854 ± 0.0091	0.1064 ± 0.0033
kun6834	57.6 ± 0.7	1.6681 ± 0.0542	1.0453 ± 0.0188	-0.0371 ± 0.1051
run6836	57.3 ± 0.7	1.5854 ± 0.0233	1.0554 ± 0.0082	0.1568 ± 0.0422
kun6840	52.3 ± 0.7	1.6953 ± 0.2311	0.9938 ± 0.0789	0.0204 ± 0.4701
run6844	160.6 ± 0.7	0.8113 ± 0.0097	0.9498 ± 0.0105	0.0943 ± 0.0063
run6914	47.4 ± 0.7	1.5608 ± 0.1670	0.8399 ± 0.1862	0.2146 ± 0.0740
kun6919	60.3 ± 0.7	1.5722 ± 0.0148	1.0643 ± 0.0136	0.1248 ± 0.0062
run6922	56.0 ± 0.7	1.6227 ± 0.0224	1.0693 ± 0.0138	0.1288 ± 0.0098
run6925	55.1 ± 0.7	1.6080 ± 0.0220	1.0881 ± 0.0200	0.1270 ± 0.0147
run6929	51.7 ± 0.7	1.5424 ± 0.2430	1.0287 ± 0.2856	0.1677 ± 0.1207
run6932	46.2 ± 0.7	0.3094 ± 1.9489	-0.5496 ± 1.4108	0.1669 ± 0.6626
run6934	46.2 ± 0.7	0.6858 ± 1.5099	2.5817 ± 1.1516	-0.4934 ± 0.5075
run6936	51.3 ± 0.7	1.6392 ± 0.1455	1.0644 ± 0.1905	0.1543 ± 0.0793
run6939	51.1 ± 0.7	1.7563 ± 0.1510	1.1928 ± 0.1017	0.1670 ± 0.0339
run6944	55.4 ± 0.7	1.6325 ± 0.0581	1.1230 ± 0.0320	0.1233 ± 0.0157
run6946	55.0 ± 0.7	1.5736 ± 0.0578	0.9570 ± 0.0499	0.1264 ± 0.0147
kun6948	53.9 ± 0.7	1.6328 ± 0.0264	1.0555 ± 0.0259	0.1531 ± 0.0125
run6954	194.4 ± 0.7	0.6406 ± 0.0154	0.9224 ± 0.0079	0.0815 ± 0.0070
run6962	69.0 ± 0.7	1.4837 ± 0.0278	1.0610 ± 0.0146	0.1123 ± 0.0063

run	s [μm]	N_{120} [fNm]	N_{18} [fNm]	N_{54} [fNm]
run6966	68.9 ± 0.7	1.4697 ± 0.0322	1.0857 ± 0.0250	0.1412 ± 0.0118
run6973	70.2 ± 0.7	1.4605 ± 0.0250	1.0661 ± 0.0246	0.1230 ± 0.0090
run6975	69.9 ± 0.7	1.4850 ± 0.0418	1.0849 ± 0.0218	0.1331 ± 0.0111
run6984	196.1 ± 0.7	0.6572 ± 0.0118	0.9328 ± 0.0058	0.0857 ± 0.0041
run6991	69.8 ± 0.7	1.4653 ± 0.0168	1.0453 ± 0.0156	0.1428 ± 0.0112

A.2 Gravitational Centering Data

The following is the list of data runs used for gravitationally centering the pendulum test-mass on the attractor rotation axis. The first set of centering data was taken before the science data collection and before the apparatus leveling. The second set of centering data was taken after the apparatus was leveled. The third set of centering data was actually assembled from runs only slightly translated from center and provided no centering information. Sets 3 and 4 were taken after the ion pump failed, was removed, and re-attached and reflect the change in tilt and centering following that process. Data collected after run6792 was referenced to the gravitational center of these sets.

set	run	$x-$mic	$y-$mic	N_{120} [fNm]
0	run6250	-0.277	-2.176	0.69492 ± 0.02193
0	run6253	-0.177	-2.177	0.74096 ± 0.01597
0	run6257	-0.077	-2.176	0.63947 ± 0.01434
0	run6260	-0.189	-2.177	0.74209 ± 0.00978
0	run6263	-0.197	-2.225	0.67998 ± 0.01402
0	run6266	-0.191	-1.935	0.53912 ± 0.01721
0	run6269	-0.192	-1.998	0.69982 ± 0.02569
0	run6272	-0.197	-2.284	0.56615 ± 0.0128
0	run6276	-0.193	-2.113	0.82645 ± 0.01076
1	run6307	-0.193	-2.113	1.18861 ± 0.03796

set	run	$x-$mic	$y-$mic	N_{120} [fNm]
1	run6310	-0.192	-2.028	1.05548 ± 0.03552
1	run6313	-0.195	-2.198	1.17543 ± 0.01165
1	run6316	-0.197	-2.284	0.93395 ± 0.02142
1	run6320	-0.194	-2.368	0.62313 ± 0.01908
1	run6323	-0.192	-1.944	0.7893 ± 0.03358
1	run6326	-0.146	-2.138	1.28121 ± 0.01626
1	run6329	-0.233	-2.138	1.12623 ± 0.02765
1	run6332	-0.065	-2.138	1.22079 ± 0.01704
1	run6335	-0.317	-2.137	0.83701 ± 0.01633
1	run6338	-0.129	-2.138	1.25393 ± 0.0327
1	run6344	0.063	-2.137	0.80615 ± 0.04116
2	run6802	-0.129	-2.138	1.50926 ± 0.15881
2	run6804	-0.129	-2.138	1.45947 ± 0.07473
2	run6807	-0.129	-2.138	1.49747 ± 0.08289
2	run6810	-0.134	-2.138	1.46458 ± 0.04418
2	run6813	-0.125	-2.138	1.49393 ± 0.04929
2	run6816	-0.129	-2.148	1.43306 ± 0.02972
2	run6819	-0.129	-2.128	1.48665 ± 0.03321
3	run7003	-0.225	-2.138	1.09975 ± 0.01513
3	run7006	-0.034	-2.137	1.18759 ± 0.01815
3	run7009	-0.129	-2.138	1.28705 ± 0.01515
3	run7012	-0.132	-2.232	1.10935 ± 0.01793
3	run7015	-0.127	-2.038	1.20205 ± 0.02133
3	run7018	-0.127	-1.94	0.92302 ± 0.01635
3	run7021	-0.13	-2.33	0.72712 ± 0.0155
3	run7024	0.065	-2.137	0.95993 ± 0.03218

set	run	$x-$mic	$y-$mic	N_{120} [fNm]
3	run7027	-0.326	-2.138	0.72616 ± 0.01871
4	run7113	-0.107	-2.114	1.31747 ± 0.00981
4	run7116	0.087	-2.113	0.87038 ± 0.01993
4	run7119	-0.007	-2.113	1.19826 ± 0.01909
4	run7122	-0.304	-2.114	0.8139 ± 0.01233
4	run7125	-0.213	-2.114	1.15646 ± 0.01854
4	run7130	-0.106	-1.916	0.80141 ± 0.016
4	run7133	-0.109	-2.306	0.90238 ± 0.01982
4	run7136	-0.109	-2.213	1.21288 ± 0.01421
4	run7139	-0.105	-2.014	1.18226 ± 0.01704

A.3 Calibration Data

Lateral centering of the calibration turntable was performed with an additional set of calibration spheres on the external turntable and measuring the 4ω torque amplitude. Further details can be found in Chapter 8.

run	x^c-mic [mm]	y^c-mic [mm]	$N_4 \cos$ [fNm]	$N_4 \sin$ [fNm]
run6862	-313.22	-310.99	-0.2061 ± 0.0118	-0.0829 ± 0.0115
run6864	-313.21	-309.0	-0.2617 ± 0.0097	-0.1116 ± 0.0105
run6866	-313.22	-312.97	-0.1281 ± 0.0231	0.0023 ± 0.0206
run6868	-313.22	-314.96	-0.0801 ± 0.0089	0.0108 ± 0.0103
run6870	-313.22	-316.96	-0.0017 ± 0.0105	0.0373 ± 0.0099
run6872	-313.22	-318.96	0.0037 ± 0.0150	0.0608 ± 0.0147
run6874	-313.21	-320.96	0.0835 ± 0.0117	0.0904 ± 0.0116
run6876	-313.21	-317.11	0.0120 ± 0.0141	0.0179 ± 0.0117
run6879	-311.22	-317.1	0.0024 ± 0.0121	-0.0287 ± 0.0120
run6881	-315.19	-317.1	-0.0784 ± 0.0097	0.0730 ± 0.0087

run	x^c-mic [mm]	y^c-mic [mm]	$N_4 \cos$ [fNm]	$N_4 \sin$ [fNm]
run6883	-309.22	-317.1	0.0383 ± 0.0097	-0.0835 ± 0.0100
run6885	-312.08	-317.1	-0.0380 ± 0.0158	0.0093 ± 0.0231

The vertical centering of the calibration turntable was performed by vertically translating the external turntable and maximizing the 3ω torque signal. Further details can be found in Chapter 8.

run	z^c-mic [mm]	N_3 [fNm]
run6887	-294.97	2.0933 ± 0.0081
run6893	-296.97	2.1043 ± 0.0125
run6891	-292.97	2.1036 ± 0.0084
run6895	-299.96	2.0928 ± 0.0064
run6897	-290.98	2.1010 ± 0.0066
run6899	-280.98	2.0976 ± 0.0086
run6901	-310.82	2.0269 ± 0.0077
run6903	-305.98	2.0523 ± 0.0086
run6905	-271.01	2.0288 ± 0.0151
run6907	-275.97	2.0488 ± 0.0065
run6909	-283.96	2.0880 ± 0.0058

We took a total of ten calibration runs at a fixed calibration turntable position prior to the lateral and vertical centering measurements given above. All calibration runs were taken with the calibration turntable position at $(x^c, y^c, z^c) = (-314.67, -310.99, -294.96)$mm.

run	$N_3 \cos$ [fNm]	$N_3 \sin$ [fNm]
run6596	2.0542 ± 0.0199	0.6091 ± 0.0192
run6610	2.0437 ± 0.0106	0.6061 ± 0.0103
run6630	2.0425 ± 0.0231	0.5812 ± 0.0236

run	$N_3 \cos$ [fNm]	$N_3 \sin$ [fNm]
run6656	2.0579 ± 0.0104	0.6204 ± 0.0077
run6670	2.0148 ± 0.0211	0.5671 ± 0.0311
run6701	2.0432 ± 0.0111	0.5985 ± 0.0124
run6719	2.0479 ± 0.0141	0.6024 ± 0.0133
run6746	2.0447 ± 0.0054	0.5938 ± 0.0051
run6795	2.0497 ± 0.0110	0.5801 ± 0.0136
run6826	2.0411 ± 0.0137	0.5775 ± 0.0189

Appendix B

B.1 Second order tilt corrections

We approximated the effect of a single tilt of either test-mass Ψ by a second-order correction to the predicted torque from the RMS change in separation

$$N(s,\Psi) \approx N(s,0) + \frac{1}{2}\Delta s^2(\Psi)\frac{\partial^2 N}{\partial s^2}.$$

To find the RMS change in separation of the wedge pattern from a tilt we average the change in separation over the area of the pattern (the same as done in [19])

$$\begin{aligned} s(\Psi) &= s + r\sin\Psi\sin\phi \\ \rightarrow \Delta s^2(\Psi) &= \frac{1}{\pi(R_o^2 - R_i^2)}\int_{R_i}^{R_o}\int_0^{2\pi}(s(\Psi)-s)^2\, r\, dr\, d\phi \\ &= \frac{1}{\pi(R_o^2 - R_i^2)}\int_{R_i}^{R_o}\int_0^{2\pi} r^2\sin^2\Psi\sin^2\phi\, r\, dr\, d\phi \\ &= \frac{1}{4}(R_o^2 + R_i^2)\sin^2\Psi \end{aligned}$$

Now we consider the case where both the pendulum and attractor are tilted. We assume that the pendulum has a fixed tilt Ψ_P (assumed to be along y), and the attractor has a tilt Ψ_A that changes orientation as the turntable rotates

$$\begin{aligned} s_p &= z_p + y\sin\Psi_P = z_p + r\sin\phi\sin\Psi_P \\ s_a &= z_a + x\sin\Psi_A\sin\omega t + y\sin\Psi_A\cos\omega t \\ &= z_a + r\cos\phi\sin\Psi_A\sin\omega t + r\sin\phi\sin\Psi_A\cos\omega t \\ \rightarrow s(\Psi_A,\Psi_P) &= s_p - s_a = s + r\cos\phi(\sin\Psi_A\sin\omega t) + r\sin\phi(\sin\Psi_P + \sin\Psi_A\cos\omega t) \end{aligned}$$

We now average the change in separation over the area of the pattern and a full rotation to find the time-averaged tilt contribution

$$\begin{aligned}
\Delta s^2(\Psi_A, \Psi_P) &= \frac{\omega}{2\pi}\frac{1}{\pi(R_o^2 - R_i^2)}\int_0^{\frac{2\pi}{\omega}}\int_0^{2\pi}\int_{R_i}^{R_o}(s(\Psi_A, \Psi_P) - s)^2\, r\, dr\, d\phi\, dt \\
&= \frac{\omega}{8\pi^2}(R_o^2 + R_i^2)\iint[\cos^2\phi(\sin\Psi_P + \sin\Psi_A\sin\omega t)^2 + \sin^2\phi\sin^2\Psi_A\cos^2\omega t \\
&\qquad + 2\cos\phi\sin\phi(\sin\Psi_P + \sin\Psi_A\sin\omega t)\sin\Psi_A\cos\omega t]\, d\phi\, dt \\
&= \frac{\omega}{8\pi}(R_o^2 + R_i^2)\int_0^{\frac{2\pi}{\omega}}(\sin\Psi_P + \sin\Psi_A\sin\omega t)^2 + \sin^2\Psi_A\cos^2\omega t\, dt \\
&= \frac{\omega}{8\pi}(R_o^2 + R_i^2)\int_0^{\frac{2\pi}{\omega}}\sin^2\Psi_P + \sin^2\Psi_A + 2\sin\Psi_P\sin\Psi_A\sin\omega t\, dt \\
&= \frac{1}{4}(R_o^2 + R_i^2)(\sin^2\Psi_A + \sin^2\Psi_P) \\
&= \Delta s^2(\Psi_A) + \Delta s^2(\Psi_P)
\end{aligned}$$

This shows that the two RMS separation changes from a rotating and stationary tilt add in quadrature.

B.2 Radial misalignment corrections

We made use of the same empirical function as in [19] to account fo radial misalignments of the pendulum and attractor test-masses, defined as follows

$$\begin{aligned}
R(r, s, \lambda) &= c_0 + (1 - c_0)\cos(f(s, \lambda)r) \\
f(s, \lambda) &= c_1 + c_2 e^{c_3 y(s,\lambda)} \\
y(s, \lambda) &= \begin{cases} s, & \text{Newton } (\lambda = \infty) \\ (1 - e^{c_6\lambda})s + c_4 e^{c_5\lambda}, & \text{Yukawa} \end{cases}
\end{aligned}$$

The coefficients $(c_0 - c_6)$ were derived from fits to Monte-Carlo calculations of radially misaligned torques, as detailed in Chapter 2. However, these calculations only accounted for a single fixed radial offset. We modified our predictions to account for both the fixed radial offset of a mis-centered pendulum test-mass $\vec{r}_p$ and a radial offset that changed orientation

with the attractor rotation, i.e. runout of the attractor test-mass $\vec{r}_A(\phi)$. Without loss of generality, we assume both offsets are oriented along the $x-$axis when the turntable angle is at the index mark, $\phi = 0$.

$$\begin{aligned} R(\vec{r}_p, \vec{r}_A, s, \lambda) &= c_0 + (1 - c_0)\cos(f(s,\lambda)|\vec{r}_p - \vec{r}_A|) \\ &= c_0 + (1 - c_0)\cos\left(f(s,\lambda)\sqrt{r_p^2 + r_A^2 - 2r_p r_A \cos\phi}\right) \\ &\approx c_0 + (1 - c_0)\cos\left(f(s,\lambda)r_> - f(s,\lambda)r_< \cos\phi\right) \end{aligned}$$

where we have expanded the square root to first order in the lesser radial offset. If we simply time average over a full attractor rotation we find

$$\begin{aligned} R(\vec{r}_p, \vec{r}_A, s, \lambda) &\approx \frac{1}{2\pi}\int_{-\pi}^{\pi} c_0 + (1 - c_0)\cos\left(fr_> - fr_< \cos\phi\right) d\phi \\ &= \frac{1}{2\pi}\int_{-\pi}^{\pi} c_0 + (1 - c_0)\cos\left(fr_>\right)\cos\left(fr_< \cos\phi\right) d\phi \\ &= c_0 + (1 - c_0)\cos(fr_>)J_0(fr_<). \end{aligned}$$

To a good approximation $(fr_<) \ll 1$, and we make a simpler and nearly identical prediction as follows

$$\begin{aligned} R(\vec{r}_p, \vec{r}_A, s, \lambda) &\approx \frac{1}{2\pi}\int_{-\pi}^{\pi} c_0 + (1 - c_0)\cos\left(fr_>\right)\cos\left(fr_< \cos\phi\right) d\phi \\ &\approx c_0 + (1 - c_0)\cos\left(fr_>\right)\left(1 - \frac{(r_< f)^2}{4}\right). \end{aligned}$$

We used this simpler form of a correction for two radial offsets (the same as in [19]) in our final fitting procedure.